MINIMUM ENERGY PATHS IN SPIN CHAIN SYSTEMS

Paul Iulian Gavriloaea

Master of Science (by Research)

University of York

Physics

December 2020

Abstract

Minimum energy paths (MEPs) link two given stable magnetic configurations and reveal the energy barrier between states. Analysing reaction pathways is especially relevant in the context of magnetic recording where one is concerned with the thermal stability of written data. The storage industry is currently migrating to Heat Assisted Magnetic Recording enabling the writing process of highly coercive grains. However, thermal stability remains a problem, especially when the bit patterns are subjected to high temperatures during the writing or rewriting of neighbouring tracks.

Concerning ourselves with the long-term and controlled stability of the recorded information, we developed an atomistic 1-dimensional model which allows us to analyse MEPs of reversal and extract the corresponding energy barriers. Our work is based on the Lagrange multiplier method of finding points of extremum for functions subject to equality constraints. Here, we integrate the Lagrange optimisation strategy in a direct minimisation tool based on the gradient descent algorithm.

We first apply our model to a generic single-phase spin chain, demonstrating its ability to track energy surfaces for coherent or domain-wall based reversal. Energy barriers are investigated varying the height of the grain, achieving good agreement with the Stoner-Wohlfarth model or the 180° Bloch wall description. Additionally, our results are shown to overlap with the dynamic calculations obtained using the Landau-Lifshitz-Gilbert equation. An analysis of field-dependent MEPs, revealed identical coercivities irrespective of the grain height, in the case of an applied field parallel with respect to the easy-axis. Finally, we qualitatively describe MEPs of reversal in exchange coupled hard/soft systems emphasising the role of the interfacial exchange in lowering the switching field. Presently, the model can successfully be applied in monolayer structures; in bi-layer systems, the Lagrange multiplier method is limited due to the form of the constraint field acting upon the spin chain.

Table of Contents

List of Tables

List of Figures

Bunicii mele, Victoria..

Acknowledgements

First of all, I would like to thank Prof. Roy Chantrell for the opportunity of studying under his supervision at the University of York as well as for his patience and continuous support. This has proven to be an extraordinary learning experience for which I am forever grateful. Secondly, I would like to thank Sergiu Ruta for the fruitful discussions and guidance. To both Sergiu and Mara, thank you for all your advice and help received long before the Master started. My further appreciation belongs to the whole Computational Magnetism group: Andrea, Ewan, Andrew, Tim, Sarah, Daniel, Junlin, Richard and Jane for the lively and friendly atmosphere I was made part of this entire period. Moreover, I would like to thank prof. Alexandru Stancu and the whole Electricity and Magnetism department at the "Alexandru Ioan Cuza" University of Iasi for the chance to study and grow by their side all throughout my undergraduate years. I would also like to extend my thanks to the Advanced Storage Research Consortium (ASRC) for funding my research degree. Last but not least, I would like to thank my family and friends for their continuous love and support. To you Ashleigh and Vlad, I say thank you for the laughs and the endless care you've shown towards me.

Declaration

I declare that except where specific reference is made to contributions or collaborators, this thesis is a presentation of original work and I am the sole author. This work has not previously been presented for an award at this, or any other, University. All sources are acknowledged as References.

Introduction

Magnetic recording remains the primary method of storing data in the current technological era. While solid-state devices contribute to the overall performance of data management, large enterprises and cloud computing facilities rely in greater part on magnetic-based media such as tapes and especially hard-disk-drives (HDDs), due to their lower costs of production and increased stability. It is expected that by 2025, a supply of 22 Zettabytes will become available as additional storage capacity, of which approximately 60% is to be shared by HDDs - according to the International Data Center [1].

In 1956, IBM introduced the 305 RAMAC computer, with an external memory unit which would prove to define the working principle of the modern hard-drives: rotating, magnetic platters serving as the recording medium on which the information is stored and a read/write head used to access and manipulate the data. A machine weighing over a tonne, IBM's invention sustained a maximum capacity of 5 Megabytes distributed in 50 disks with an areal density of 2 kbits/in^2 [2]. In comparison, our modern devices weigh a few hundreds of grams and are able to store several Terabytes of data. One important milestone has been recently achieved in 2012, when Seagate announced the first HDD proof-of-concept to exhibit an areal density (AD) of 1 Tbits/in^2 [3]; put next to the available technology in the 1950s', this corresponds to an overwhelming increase in AD of approximately 9 orders of magnitude.

The continuous AD growth is conditioned by the balance between several limiting factors, traditionally represented within the "magnetic trilemma" - see Figure 1.1.a). The accuracy of the read process is broadly governed by the width of the transition regions between bits; if the grain sizes are decreased, the bit separation is well defined and the readback magnetic signal is improved. While both the AD and the signal-to-noise ratio (SNR) benefit from a reduction of the grain dimensions, the thermal stability factor is at disadvantage. Considering the example of a single uni-axial grain in zero field given in Figure 1.1.b), there are two accessible stable states, separated by an energy barrier defined as $\Delta E = KV$, where K represents the first-order, magnetocrystalline anisotropy constant and V is the volume of the particle. It is

now clear that a decrease in the grain size will lead to a subsequent reduction of the energy barrier. If the surrounding thermal noise $k_B T$ is comparable to the ΔE margin, irreversible switching between one energy state and another occurs and the information is consequently lost. Due to this, materials with large anisotropies are required in order to counterbalance the volume reduction effect. With the aim of preserving the information for a period of 10 years, the magnetic recording standard imposes a minimum thermal stability factor $KV/k_B T$ of 40; however, as Richter et al. point out, this needs to be adjusted to a higher value of 60 in order to account for demagnetising effects [4]. Unfortunately, the use of highly anisotropic materials leads to a writability issue since the grain coercivity (H_c) needed to satisfy the thermal stability requirement can overcome the available write fields (H_w). A maximum H_w of approximately 1.5 T can be currently obtained by using FeCo binary alloys in the write head composition, insufficient if we consider the future of magnetic recording demands grains with coercivities of at least 3 T [5].

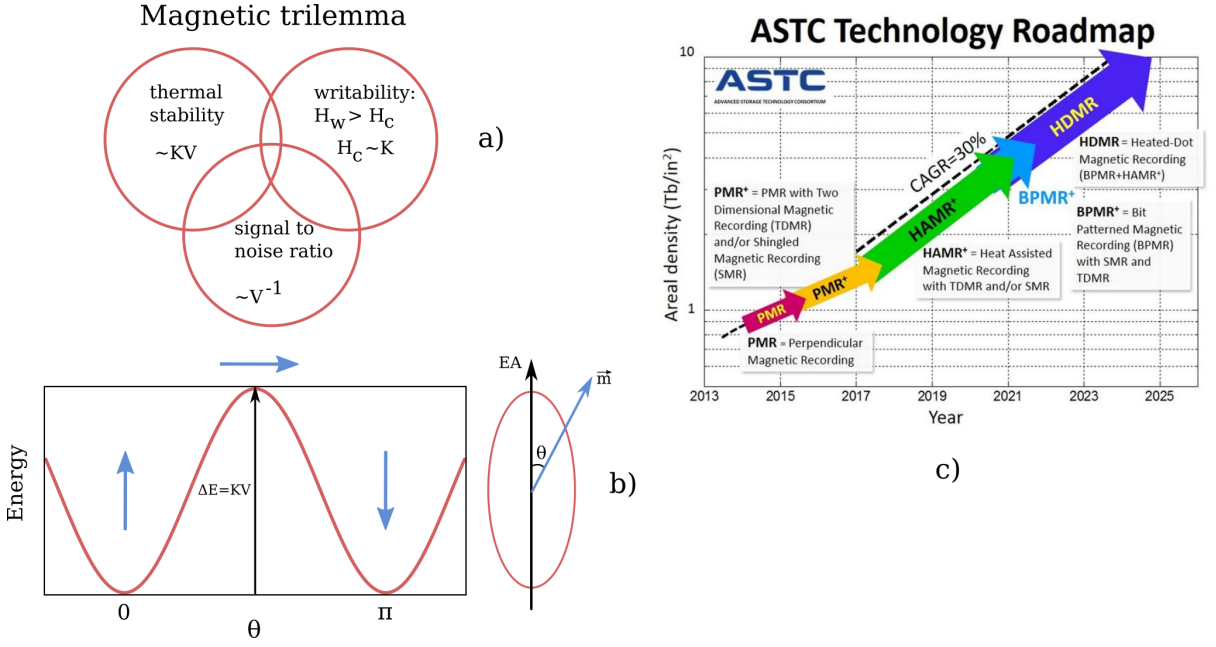

Figure 1.1: a) Schematic representation of the magnetic trilemma. b) Zero-field energy landscape for a single uni-axial particle; θ is the angle between the easy-axis (EA) and the magnetic moment $\boldsymbol{m}$. c) Predicted technology roadmap in the magnetic recording industry, proprietary to ASTC (Advanced Storage Technology Consortium) [6], recently known as ASRC (Advanced Storage Research Consortium).

According to the roadmap given in Figure 1.1.c), two main directions have been suggested in order to circumvent the limitations outlined by the magnetic trilemma. Heat Assisted Magnetic Recording (HAMR) is one of the promising solutions intended to increase areal

densities towards the 10 Tbits/in^2 margin. In order to solve the writability issue, HAMR involves laser-induced heating near the Curie temperature (T_c) of the recording layer, which gives rise to a decrease in H_c below the H_w threshold [7]. Beyond HAMR, it is expected that the current granular media will be replaced by discrete arrays of nano-dots, each representing individual bits in the so called Bit Patterned Magnetic Recording (BMPR) technology. With the dot structure being larger in size than a single grain in the conventional media, the stability criterion can be satisfied without affecting the writability aspect; another advantage would be the well-defined bit separation that can improve the SNR [8].

In the current perpendicular recording paradigm, several media designs have been suggested in order to address the conflicting elements in the trilemma. Sonobe et al. first considered the addition of a thin continuous layer over the standard granular phase, with the aim of increasing the overall thermal stability [9]. In this design known as Coupled Granular Continuous (CGC), any reversal process of the recording medium is accompanied by a domain wall nucleation in the thin layer; in this way, unwanted switching due to strong inter-grain interactions or self-demagnetising effects may be prevented. Later on, several works suggested possible workarounds for the writability issue, based on media designs consisting of hard/soft, exchange coupled systems. Victora and Shen used a two macrospin model to describe a mechanism for coercivity reduction in the so called Exchange Coupled Composite (ECC) structure [10]. The reversal process starts with the rotation of the soft phase which later provides an extra torque in the hard layer that aids its switching. In the same year, Suess et al. proposed the Exchange Spring (ES) media as a way to independently optimise the thermal stability and coercivity factors [11]. In the ES design, the switching of the hard layer is domain wall assisted as described by Dobin and Richter in [12, 13]. Hard/soft composites have also been suggested as an important component of the future HAMR technology due to their capacity of reducing thermally induced write errors [14].

The focus of this thesis revolves around the thermal stability aspect in magnetic recording. As we have seen earlier in the example of a single uni-axial particle, the key parameter governing the stability of the recorded information is the energy barrier separating two given magnetisation states. In perpendicular recording, this translates to the energy input required to reverse the magnetisation of the grains between the "up" and "down" configurations. General analytic descriptions of ΔE are difficult to define beyond the Stoner-Wohlfarth (SW) model. To characterise the thermal stability of complex media designs such as the ECC structure, numerical methods are required. Energy barrier calculations are intrinsically related to the minimum energy path (MEP) concept. Also known as a reaction path in transition state theory, a MEP links two minima across a given energy landscape, crossing

at least one first-order saddle point and defining the most likely route a system will take between the initial and final states. The main aim in our project is to develop a simple and reliable model able to track MEPs of reversal in spin chain systems, from which we can later infer the associated energy barriers. With the purpose of reducing the computational effort, we simulate one-dimensional (1D) magnetic structures which portray bulk single magnetic grains or hard/soft composites. The MEP search is a particular problem in the general field of mathematical optimisation. The most widely used numerical method in this endeavour is the Nudged Elastic Band (NEB): its first step requires the choice of an arbitrary "chain" of intermediate states or images, linking the initial and final configurations under study; an iterative approach is then used to optimise the starting pathway, by moving every image in the negative direction of the gradient and perpendicular to the current path. A fictitious spring force is being used additionally to prevent a loss of resolution near saddle points by keeping a fixed distance between each intermediate state. A powerful tool which has been successfully used previously in the field of magnetism [11, 15, 16], the NEB is an unnecessarily complex approach for the simple systems we are interested in. Every iteration step would require both energy and gradient evaluations for all the intermediate states in the chain, making parallelisation necessary.

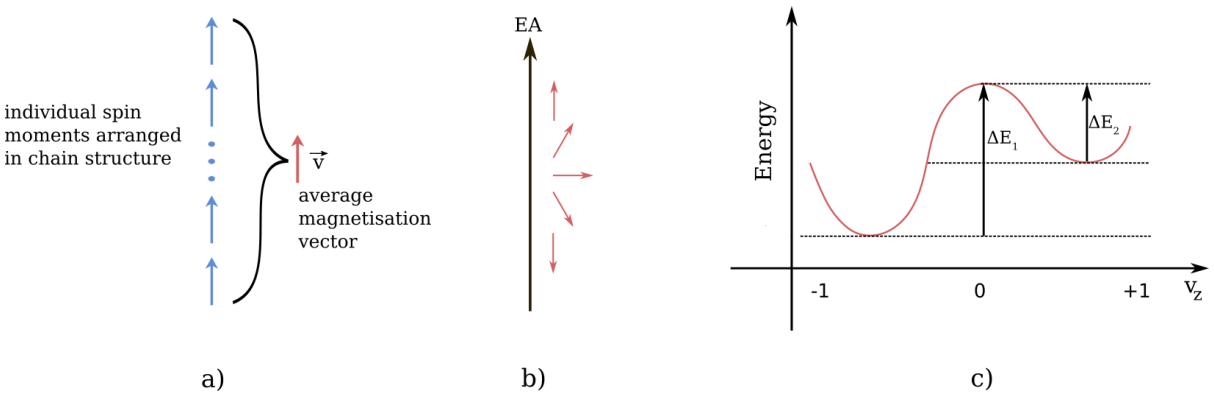

Figure 1.2: In our MEP search, we constrain the average magnetisation $\boldsymbol{v}$ of the spin chain system a) such that its projection on the EA (Oz) changes successively from the "up" to the "down" state b). The MEP is defined as the energy variation of the spin chain system during the reversal process with respect to v_z c): $E = f(v_z)$; ΔE_1 and ΔE_2 are schematic energy barriers between fictitious extrema.

In our project, the optimum paths of reversal are obtained through a Lagrange multiplier technique, incorporated in a simple direct minimisation approach which is based on the gradient descent algorithm - see Figure 1.2 for schematic steps. The key idea supported by the Lagrange multiplier method is the ability to constrain the average magnetisation vector $\boldsymbol{v}$

of the spin chain system, such that its projection on the Oz axis changes successively from $+1$ to -1, thus replicating the reversal process. The gradient descent algorithm allows us to reach the equilibrium state for every magnetic configuration along this route of reversal; finally, the MEP is given by the energy variation of the spin chain structure with respect to the z component of the average magnetisation vector: $E = f(v_z)$.

Succeeding this introductory part, the present thesis contains five additional chapters organised as follows: Chapter 2 sets the theoretical basis of our project; initially, we present essential physical quantities and classify materials according to their magnetic properties. We move on to discuss the main modelling tools in magnetism, emphasising the atomistic picture employed in our work. Next, we thoroughly analyse the extended Heisenberg Hamiltonian used to describe the spin chain systems under study. On the basis of the SW model and domain theory, we overview coherent and incoherent reversal mechanisms that later shall be used to interpret our results.

In Chapter 3, we discuss the implementation of our numerical method. The Lagrange multiplier technique is introduced in the context of optimisation theory and the gradient descent procedure is described in detail along with its relationship to the Landau-Lifshitz-Gilbert (LLG) equation. Algorithm optimisations and simulation parameters are also reviewed here.

Chapter 4 presents a series of initial tests and results obtained in the case of a generic, single-phase chain structure. MEPs are obtained for both coherent and domain wall based reversal processes and the results are compared with the description given by the LLG equation. Following this, we consider the Bloch nature of the domain walls observed in our 1D system. We then analyse the relationship between grain height and preferred reversal mechanism as well as consider the role of an external magnetic field in the switching process. Energy barriers are extracted from the reaction paths we obtain and are then compared with analytic limits described by the SW theory and the Bloch wall picture.

In the second to last chapter, we apply our numerical method in studying the reversal process of exchange coupled hard/soft systems. The results presented here have the work-in-progress label and they aim to demonstrate the present limitations of the model and the current status. Examples of MEPs are given and the role of the interfacial exchange coupling is discussed as a way to understand the thermal stability and ease of switching in a composite medium.

The final part of the thesis is dedicated to conclusions and possible future studies.

Theoretical background

Throughout this chapter, our main focus will be laying out the theoretical foundation on which the present work is based. We will firstly introduce the basic physical quantities and concepts used in the field of magnetism, as well as classify materials according to their magnetic properties. Following this, we will discuss various energy sources in a crystal, relevant to the Hamiltonian used in this thesis; we will also give a short description of the standard numerical methods implemented in the modelling of magnetic materials. Later on, we will introduce the theory behind coherent rotations and domain wall formation, essential to understand the reversal processes considered in our work. Briefly, we will also discuss the coercivity mechanisms at play in perfectly homogeneous crystals and composite media.

1 MAGNETISM AND MAGNETIC MATERIALS

Magnetism is a naturally occuring phenomenon, known to humanity for centuries and currently present in the majority of our day to day experiences. The elementary property of a magnetic material is the magnetisation:

$$\boldsymbol{M} = n\boldsymbol{m}, \tag{2.1}$$

where n represents the number of particles in a given unit volume and $\boldsymbol{m}$ is the local magnetic dipole moment. Therefore, the magnetisation gives us the density of magnetic dipole moments, in this way accounting at a macroscopic level for the total contribution of various microscopic degrees of freedom (atoms, ions, molecules and their interactions).

There are several methods to classify magnetic materials. The first one we mention – known today as the traditional method - was introduced by Faraday. He described materials with respect to their response to an external magnetic field, thus giving rise to three classes: diamagnetic, paramagnetic and ferromagnetic materials. A quantitative measure of these behaviours may be given using either the susceptibility χ or the permeability of the material

μ, depending on whether we choose to work with the magnetic field $\boldsymbol{H}$ or the induction $\boldsymbol{B}$:

$$\begin{aligned} \boldsymbol{H} &= \frac{1}{\chi}\boldsymbol{M}, \\ \boldsymbol{B} &= \mu \boldsymbol{H}, \end{aligned} \tag{2.2}$$

In Figure 2.1, we give a schematic representation of standard $\chi = f(T)$ curves in magnetism, where T is the temperature of the medium. Present as a natural reaction to any applied field - according to a Lenz-like law at the atomic level - diamagnetism is characterised by a negative, temperature independent susceptibility. Some of the most notable diamagnetic effects can be found in bismuth $\chi = -1.66 \cdot 10^{-4}$ and graphite $\chi = -4 \cdot 10^{-4}$[17]. By contrast, paramagnetic materials exhibit small and positive susceptibilities, typically in the range of $[10^{-3} \rightarrow 10^{-5}]$ [18]. In metals, the free electron model gives rise to a weak, temperature independent variant called Pauli paramagnetism. A stronger effect is present in insulators or rare-earth materials, where localised, non-interacting electrons shape the Curie paramagnetism: the susceptibility is inversely proportional to the working temperature. Above a certain T threshold, the susceptibility of a ferromagnet follows a similar temperature dependence governed by the Curie-Weiss law.

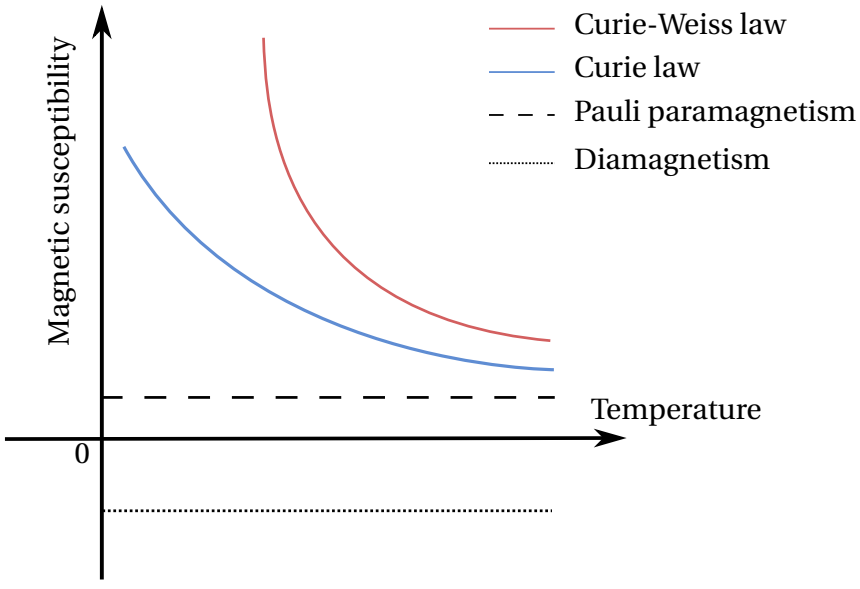

Figure 2.1: Simplified view of the standard susceptibility curves in magnetism.

Ferromagnetism itself is the result of spontaneous alignment between atomic magnetic dipoles within the material; in contrast with the previous two cases, the magnetism of the substance is present even in the absence of an external field. This behaviour can be phenomenologically explained within Weiss' molecular field theory. Moreover, the susceptibilities of ferromagnets take large positive values, usually in the range of $[50 \rightarrow 10000]$ [18]. The most representative ferromagnetic materials are Fe, Co, Ni.

A second method of classification takes into account the relative orientation between magnetic dipoles within a material - see Figure 2.2. In ferromagnets for example, the microscopic moments prefer to align parallel in order to minimise the total free energy of the system. Antiferromagnets show opposite orientation between neighouring magnetic dipoles; these systems may be viewed as two interconnected sublattices in which their respective magnetisations are of equal magnitude but oppositely oriented. As a result, the net magnetisation of the material is zero; common antiferromagnets are Cr, MnO or FeO. If the two aforementioned sublattices have net magnetisations which don't cancel out, the corresponding ordering of the dipoles is called ferrimagnetism.

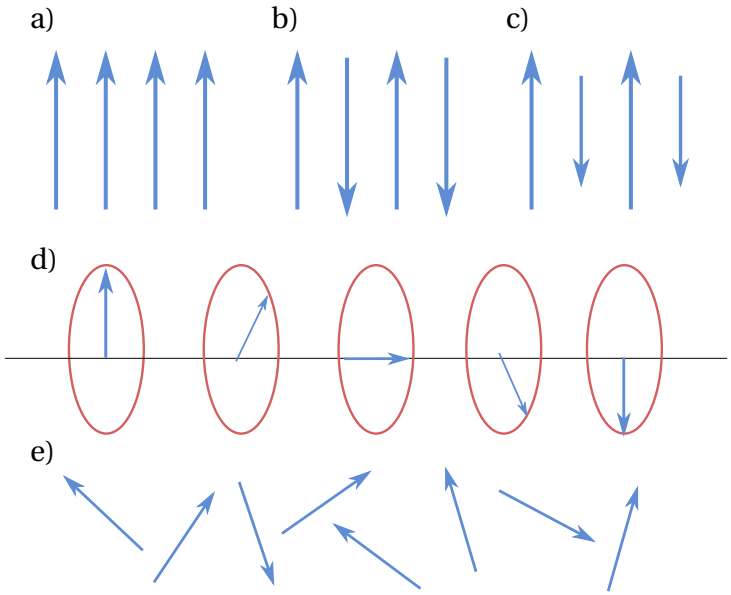

Figure 2.2: Types of magnetic configurations: a) ferromagnetic; b) antiferromagnetic; c) ferrimagnetic; d) helical; e) paramagnetic.

While ferromagnets and antiferromagnets are characterised by an ordering temperature above which they exhibit a phase transition towards paramagnetism – the Curie and the Néel temperature respectively- the magnetisation of a ferrimagnet follows a more complicated variation with temperature. Depending on the dominant lattice, the magnetisation can change sign; this transition occurs at a critical point called the compensation temperature,

where the two sublattices even out their contributions to the total magnetisation. Examples of ferrimagnets include magnetite or the low dissipative yttrium-iron-garnet. Another possible configuration is the helical order - atomic moments exhibit ferromagnetic coupling with nearest neighbours and antiferromagnetic coupling with nearest-next neighbours. The paramagnetic arrangement favours a random orientation of the moments such that the average magnetisation is zero in the absence of an external field.

Ferromagnets are regarded as the most important magnetic materials; the large susceptibility values and the ability to retain their magnetised state in the absence of a field, make them suitable for a broad spectrum of applications. Their properties can be outlined via magnetisation curves also known as hysteresis plots, in which the magnetisation of the system is investigated for a given field range. A magnetic material may find itself in two different states for the same value of an external field; this behaviour reflects how the magnetisation process is governed by the history of the system. The "hills and valleys" of the energy landscape are shaped according to the previous magnetised states, thus giving rise to different arrangements of the intrinsic magnetic dipoles for the same external stimulus, reflected in the two branches of the hysteresis plot. Ferromagnets may be separated in two classes according to their remanence and coercivity - see Figure 2.3.

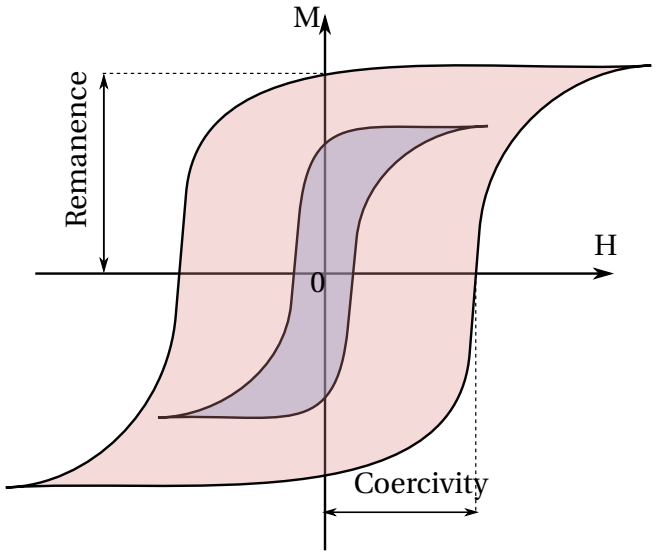

Figure 2.3: Example of hysteresis curves for both a soft (blue) and a hard material (red). Remanence and coercivity are highlighted only for the hard material.

The former outlines the ability of the material to retain its magnetisation when the external field is reduced to zero, while the latter property gives us a measure of the necessary perturbation – an external field in this case – required to fully demagnetise the system. Thus, hard magnetic materials are generally represented by high remanence and coercivity values, making them suitable as permanent magnets due to their large MH product. Examples of permanent magnets include various concentrations of NdFeB, AlNiCo or SmCo [19]. At the other end, soft magnetic materials display a narrower hysteresis loop due to in general lower remanence and coercivity. This led towards their usage in applications such as transformers or electromagnets, where a rapid response to an applied field is required, as well as a low power loss – the total losses being proportional to the area of the hysteresis loop. Typical soft magnets include permalloy (Ni-Fe) or permendur (Fe-Co). In the recording industry, hard materials are predominantly used because of their stability and capacity to retain the stored information for long periods of time. The recording media design may however require both hard and soft layers such as in the ECC technology, where the soft phase is used in order to reduce the required switching field while the structure preserves its high stability due to the coercivity of the hard layer.

2 NUMERICAL MAGNETISM

The three standard methods used to simulate magnetic materials or phenomena are: the *ab-initio*, the atomistic and the micromagnetic approach. The fundamental differences between these three methods are the length and time scales within which they can be successfully applied - see Figure 2.4. The following section will briefly describe each of the three approaches, an emphasis being shown in the description of the atomistic category.

2.1 *Ab-initio* methods

Ab-initio – "from the beginning" in Latin – methods form a class of established attempts to circumvent the impossibility of solving the Schrodinger equation for many body problems. In the case of the hydrogen atom, we can directly solve this equation thus obtaining the eigenvectors and eigenvalues which store the measurable information about the system. However, realistic descriptions require studies over large systems of particles which can no longer be tackled with the aim of obtaining exact analytic solutions. One common method of obtaining an approximate solution to the Schrodinger equation of N particles is the Density Functional Theory (DFT). Prior to its development, Hohenburg and Kohn developed

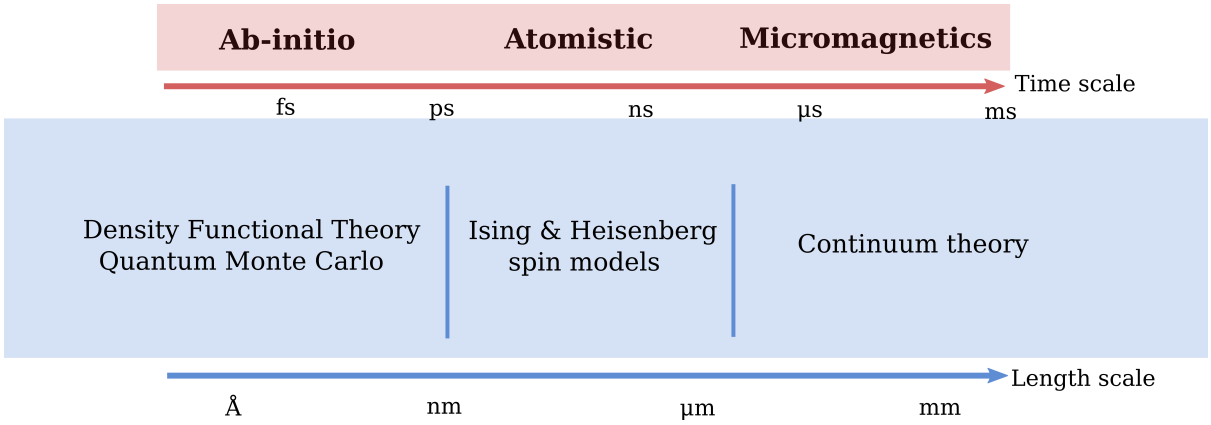

Figure 2.4: An approximate visualisation of the different length and time scales accessible for the three main modelling frameworks in magnetism: ab-initio, atomistic and the micromagnetic approach.

a theorem which states that the ground-state properties of a system can be determined via its density [20]. An N-dimensional problem can be thus reduced to only one single variable; in magnetism, DFT calculations may provide insights related to the local anisotropy, magnetic moments or strength of the exchange interactions [21].

Recent advancements have shown the usage of Quantum Monte Carlo methods in studying systems which contain d and f electrons, providing accurate results of their ground state properties [22]. First principle methods are not limited to static descriptions but they can be extended to time dependent phenomena. The TDDFT (time dependent density functional theory) method based on a time dependent particle density, may be used to model ultrafast spin dynamics [23].

An important model Hamiltonian at the electronic scale is the Hubbard description. Developed in the 1960s, it was initially used to study correlation phenomena in the partially filled d and f bands of transition metals or rare-earth materials [24]. Its picture outlines arrays of atomic sites over which electrons can move ignoring any contribution from the nuclei. Each atomic site consists of a single s orbital, which allows the presence of maximum two electrons per site – a spin up and a spin down electron. There are no interactions between the lattice points, however the model describes electron jumps from one site to its neighbours. The two electrons which may be present at a specific atomic site interact via Coulomb forces. Despite its apparent oversimplification, the Hubbard model is still used today and it represents a mathematically difficult problem for which an exact solution has been obtained only in the 1D case [25].

Notwithstanding their precise treatment and broad range of applications, *ab-initio* meth-

ods require substantial computational resources and are usually limited to small systems (tens of atoms).

2.2 Micromagnetism

The micromagnetic framework can be applied to problems in which the following hypothesis holds: above a certain length scale the atomic structure of a material can be neglected and the magnetisation can be treated as a continuous function $\boldsymbol{M} = \boldsymbol{M}(\boldsymbol{r})$, which depends on the position vector $\boldsymbol{r}$ attached to the coordinate system of the sample. This makes the method suitable for simulating structures with a resolution not lower than the size of a magnetic domain (tens of nanometers). The upper size threshold is in principle limited by the available computational resources.

The main goal of standard micromagnetic simulations is the attempt to find the spatial distribution of $\boldsymbol{M}(\boldsymbol{r})$ which minimises the total free energy of the system [26]. Only in a small number of cases, explicit analytic solutions of micromagnetic problems are obtained. In this category we can find the description of Bloch and Néel domain walls, critical diameter calculations which define the mono-domain limit for specific geometrical shapes or the determination of certain nucleation fields. Numerical micromagnetics gives the possibility of tackling a more generous amount of problems; using various discretisation techniques, the magnetic texture is divided into cells of different volumes which are then assigned an average magnetisation vector called a macrospin. The dimensions of the cells must be chosen such that the continuum approximation is satisfied and a reliable resolution is achieved.

Furthermore, dynamic investigations are also possible in the context of micromagnetic modelling. For temperatures well below the Curie point, a stochastic LLG equation can be used to model the magnetisation dynamics [27]; near the ordering temperature, the magnitude of the $\boldsymbol{M}(\boldsymbol{r})$ vector drastically drops and longitudinal relaxation processes are prevalent; in this situation one can use the Landau-Lifshitz-Bloch (LLB) equation to correctly describe dynamic processes at elevated temperatures [28]. The micromagnetic formalism is inherently limited by the continuum approximation; due to this, it cannot capture atomic level details such as surface or interface effects.

2.3 Atomistic models

The connecting link between *ab-initio* and micromagnetic calculations is represented by the atomistic class of magnetic models such as the Heisenberg or Ising descriptions. Within this framework, one is concerned with system sizes ranging from a few angstroms up to tens or

hundreds of nanometers.

The Ising model is one of the simplest methods used to describe a system of interacting spins. It was proposed by Wilhelm Lenz as a model for ferromagnetism and it was later explored by Ernst Ising - one of his students - during his doctoral studies, prior to the introduction of the spin as an additional electron property. The model assumes that atomic dipoles are able to rotate in a quantised manner, such that only two orientations are possible with respect to a fixed axis. Contrary to Weiss' phenomenological theory of ferromagnetism, Lenz argued that the spontaneous magnetisation can be interpreted based on these systems of dipoles, able to rotate with respect to their neighbours such that the total energy is minimised when parallel orientation arises. Moreover, the forces exerted by the elementary magnets are not of dipolar nature as in Weiss' theory; their strength fades rapidly with distance, hence only nearest neighbour interactions have been considered in the studies conducted by Ising. Following standard methods of calculations from statistical mechanics, Ising gives a complete description of the model in the 1D case; he arrives at an analytic expression for the average magnetisation of the system which shows that in zero applied field no spontaneous alignment is possible [29]. Thus, any ordered configuration in a chain-like system is only a metastable state and no phase transitions can occur. Based on his findings, Ising asserts that no phase transitions are possible in higher dimensions either, a conclusion which came to be contradicted years later.

The framework which explained ferromagnetism in a direct, non-phenomenological way was developed by Heisenberg using quantum mechanical tools. After the fourth quantum number was postulated and the Pauli exclusion principle introduced, Heisenberg showed how overlapping wave functions of electrons belonging to neighbouring atoms give rise to an unique "exchange" interaction, with no classical analogue [30]. Given that the orbital contribution to the total magnetic moment may be usually neglected, we can reduce the magnetism of condensed matter to a description of the spins. In a simplified manner, one can drop the quantum nature of atomic magnetic moments and allow them complete freedom of rotation over the surface of a sphere; attaching spin vectors of fixed length to atomic sites, it is possible to treat localised systems of electrons in a semi-classical approach. The unknown "forces" between magnetic dipoles suggested by Lenz and Ising, take now the form of the exchange interaction between neighbouring spins, giving rise to the classical Heisenberg model. The latter represents the basis upon which we develop the framework used throughout the thesis. This atomistic model can also be used in conjuction with the classic or stochastic variants of the LLG equation in order to capture dynamic phenomena: ultra-fast, temperature induced switching in magnetic recording [31], skyrmion or domain

wall motion [32, 33] and STT (spin-transfer-torque) or SOT (spin-orbit-torque) induced magnetisation processes [34, 35].

3 ATOMIC MAGNETIC MOMENTS

Before moving on to describe the various interactions arising in a magnetic sample, we need to establish the nature of the microscopic degrees of freedom which give rise to magnetic effects. To achieve this, we will describe via classical physics and later quantum theory the different contributions adding up to the total magnetic moment of an atom. Since experiments don't match with the theoretical magnetic moments in certain bulk materials (e.g. Fe, Co or Ni), we will have to introduce a series of concepts from band theory in order to account for the observed discrepancies.

3.1 From classical physics to quantum theory

The total magnetic moment which characterises an atom is mainly given by the two electron contributions: orbital and spin. The first one of these arises as a consequence of the electron revolution about the nucleus. Using the classical theory of electromagnetism, we can calculate this term making an analogy between the orbital motion and the picture of an Amperian loop current. The magnetic moment associated with this electrical circuit is directly proportional to the loop area A_{loop} and the current flowing through the coil, I:

$$\boldsymbol{m}_l = I\boldsymbol{A}_{loop} = -\frac{e}{2m_0}\boldsymbol{l}_o, \tag{2.3}$$

where e is the elementary charge, m_0 gives the mass of the electron and $\boldsymbol{l}_o$ is the orbital angular momentum. The vector $\boldsymbol{A}_{loop}$ points normal to the surface of the loop while its magnitude is equal to the total area enscribed by the circular orbit.

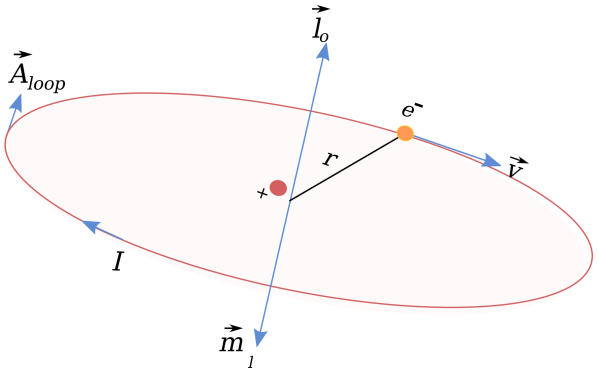

Figure 2.5: Schematic representation of the electron revolution about the nucleus and its equivalence to a current loop.

In our analogy, the current flow is generated by the periodic rotation of the electronic charge at a certain distance r from the nucleus - see Figure 2.5. The importance of the orbital magnetic moment is rather small in bulk systems; in the case of Fe for example, it is considered that only 5% of the total magnetic moment can be ascribed to the loop currents

[36]. Furthermore, this classical picture is incapable of capturing the origins of magnetism in electrical insulators. The electron spin gives the second contribution to the total magnetic moment; associating an angular momentum to the spin term, we can rewrite equation (2.3) in a general manner:

$$\boldsymbol{m} = -g\frac{e}{2m_0}\boldsymbol{l} = -\gamma\boldsymbol{l}, \tag{2.4}$$

where the g-factor takes the values 1 or 2 for the orbital and spin magnetic moment respectively; the γ constant is referred to as the gyromagnetic ratio. The spin can no longer be described in terms of any classical analogy. One should not consider it as a consequence of a hypothetical electron rotation around its axis; in this case, the observed angular momentum would require the electron to rotate faster than the speed of light.

The results of quantum theory tell us that the angular momentum can only take discrete values in units of the reduced Planck constant; due to this, the respective magnetic momenta are also quantised, the elementary unit being the Bohr magneton:

$$\mu_B = \frac{e\hbar}{2m_0} = 9.274 \times 10^{-24} J/T, \tag{2.5}$$

where $\hbar$ is the reduced Planck constant. In many electron atoms, a vector model may be used to determine the net angular momentum and magnetic moment by summing the spin and orbital contributions of the individual electrons. Taking into account the Pauli exclusion principle and Hund's rules, one can focus solely on the unfilled electron shells. As such, there are principally two ways of adding the contributions together based on vector summations. The first method, referred to as the $L-S$ coupling (or Russell-Saunders) can be used for lighter atoms in which the spin-orbit coupling is negligible in comparison to the spin-spin and orbit-orbit interactions; in this case, it is reasonable to add the total orbital contributions of each electron, separately from the spin momenta:

$$\boldsymbol{L} = \sum_i \boldsymbol{l}_o \tag{2.6}$$

$$\boldsymbol{S} = \sum_i \boldsymbol{l}_s \tag{2.7}$$

Eventually, the two resultant vectors may be combined to calculate the total angular momentum of the system: $\boldsymbol{J}_t = \boldsymbol{L} + \boldsymbol{S}$; the latter will in turn reveal the magnetic moment $\boldsymbol{m}_J = -g_J\frac{\mu_B}{\hbar}\boldsymbol{J}_t$. Since the strength of the spin-orbit interaction is proportional to the fourth power of the atomic number Z^4 [37], the Russell-Saunders coupling isn't useful when describing heavier atoms. In this case, one implements the jj coupling scheme in which the spin and

orbital momenta of each electron add up to local contributions $\boldsymbol{j} = \boldsymbol{l}_o + \boldsymbol{l}_s$, which are then summed over the whole system:

$$\boldsymbol{J}_t = \sum_i \boldsymbol{j} \tag{2.8}$$

The net magnetic moment is then obtained in a similar fashion as in the $L-S$ coupling.

3.2 Elements of band theory

Unfortunately, the vector model overestimates the observed magnetism in materials such as metals, where the discrete orbital picture cannot account for the delocalised nature of electrons. For example, if one makes use of the Pauli principle and the Hund rules to fill the available energy levels in the Fe atom, there would be a total of 4 *3d* unpaired electrons. The spin contribution of these electrons amounts to $4\mu_B$; even without considering the orbital component, using the vector model we obtain a much bigger value in comparison to the total measured magnetic moment: $2.21\mu_B$.

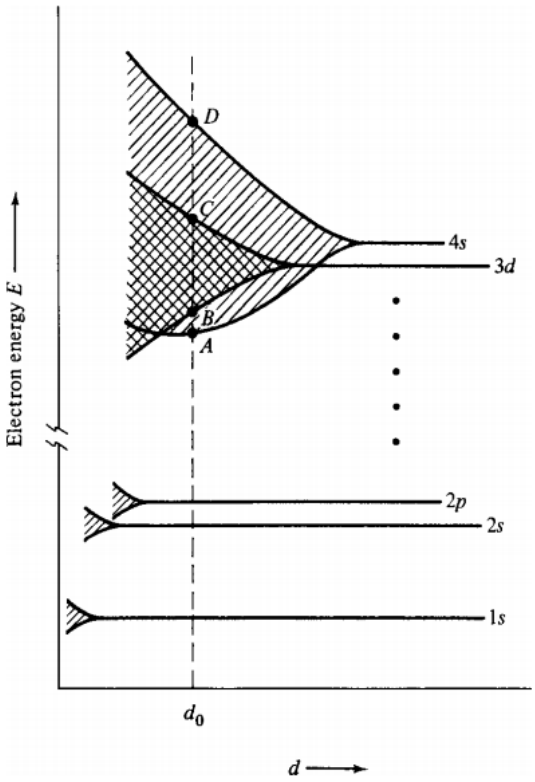

Figure 2.6: When atoms are brought together, a splitting of the energy levels occurs according to the interatomic distance d and the electron energies. The figure was extracted from [38].

Aditionally, the aforementioned model cannot account for the non-integer values one obtains experimentally for the projection of the magnetic moment on a reference axis. The same considerations may be applied for the other two natural ferromagnets, Co and Ni [39]. The explanation for these differences may be given using the band picture of solids. When atoms are brought together, a splitting of the discrete energy levels must occur such that the exclusion principle is satisfied. This splitting and the large number of atoms in solids lead to the appearance of energy bands which increase in width (W) as the interatomic distances d decrease: $W \propto d^{-5}$ [40]. The extent of the splitting as well as the band broadening also depend on the involved energy levels - see Figure 2.6.

As such, the *3d* levels of Fe atoms will lead to a wider energy band since the electrons there are the first to interact with the neighbouring atomic sites. The *1s* electrons though are closer to the nucleus and their corresponding band will have a narrower profile. According to Cullity [38], in 1 *mg* of Fe, each individual energy level of the free atom splits in approximately 10^{19} levels, shifting the focus from the discrete levels of energy portrayed in the vector model towards density of levels in the band.

The simplest description of ferromagnetism in metals, based on the band picture of solids, is the Stoner-Wohlfarth-Slater model. Within it, ferromagnetism is explained as an imbalance between the spin-up and spin-down subbands. The electron transfer from one subband to the other requires an increase in the kinetic energy of the system; however, it can be shown that such a transfer occurs in *3d* transition metals due to the strong exchange interactions between spins. This in turn favours the appearance of a mean-field felt by neighbouring spins, which compensates the kinetic energy penalty by lowering the total energy of the system when the two spin populations are unbalanced. Thus, the electron transfer leads to a net magnetic moment which according to Buschow and de Boer [40] can be written in a simple manner as:

$$m = 2pn_e\mu_B, \tag{2.9}$$

where n_e is the total number of electrons per atom and p represents the fraction of electrons that moved from one spin subband to the other. It is now clear how the magnetic moment can be written in non integer units of the Bohr magneton.

4 THE SPIN HAMILTONIAN

Our work is based on the atomistic model initially developed by Heisenberg. We treat magnetic moments in a semi-classical manner, assigning a vector $\boldsymbol{s}$ with complete rotational freedom to each atomic site. The magnitude of these vectors is considered to be fixed and equal to 1 which provides an advantage in numerical calculations. Hereafter, we will be referring to these vectorial quantities as spins, acknowledging the importance of the spin magnetic moment and neglecting the orbital component. The Spin Hamiltonian defining the total energy of an individual spin includes a Zeeman term, the exchange interaction with nearest-neighbours and an uni-axial anisotropy component. Throughout this section we will discuss each energy term in detail. The Spin Hamiltonian will be augmented in the next chapter with a constraint component owing to the Lagrange multiplier method used to map MEPs of reversal in the present thesis.

4.1 Zeeman energy

Technology wise, there are several limitations when generating magnetic fields at the scales the magnetic devices operate today, either due to the reduced sizes or for energy consumption reasons. An essential component of our project is the correct evaluation of MEPs and corresponding energy barriers as a function of the applied field strength. As such, it is important to introduce in the total Hamiltonian the contribution given by the interaction between spins and an external magnetic field:

$$\mathscr{H}_{ext} = -\sum_i \mu_s^i \boldsymbol{s}_i \cdot \boldsymbol{H}, \tag{2.10}$$

where i denotes the spin id, μ_s^i represents the local spin magnetic moment and $\boldsymbol{H}$ is the applied magnetic field.

Historically, the interaction between atoms and magnetic fields has first been observed by Pieter Zeeman in 1896 when studying the emission spectrum of Na. At the time, quantum theory was not available yet and our picture of the atomic world was very limited, the discovery of the electron taking place only a year later. The splitting of the spectral lines is currently fully understood on the basis of spin and orbital magnetic moment quantisation. Before the idea of "spin" was introduced, the effect observed in Na emissions was coined as "anomalous" in contrast with the results obtained in the case of hydrogen or calcium which yielded simpler atomic spectra and they were referred to as the "normal" Zeeman effect.

4.2 Exchange interaction

An external magnetic field will exert a torque on the atomic magnetic moments within a material, which will lead to their tendency to align on the direction of the field thus giving rise to a change in the total magnetisation. This picture helps us understand how paramagnets for example can be polarised via applied fields but it doesn't account for the spontaneous magnetisation observed in the case of ferromagnets. As stated in the previous chapter, the self sustaining magnetism of Fe, Co or Ni had been given an initial explanation by Pierre Weiss in 1907 [41], when he postulated the existence of a molecular field as the result of a positive feedback mechanism: $\boldsymbol{H}_m = n_w \boldsymbol{M}$, where n_w is the Weiss coefficient. This however is only a purely phenomenological description and it doesn't follow a step by step derivation from first principle methods; it is quantum theory eventually that will give an answer to the origins of the ferromagnetic spontaneous alignment and the nature of the molecular field.

In 1928, Heisenberg investigated Weiss' ideas using the newly developed wave mechanics

and introduced the exchange interaction [30]. One year before, Heitler and London were trying to give an explanation for the origins of the covalent bond in the hydrogen molecule [42]. Each of the hydrogen atoms contains one electron revolving around a single proton nucleus. From classical electromagnetism we know that bringing the two atoms together leads to three Coulomb interactions: electron-electron, electron-proton and proton-proton. Quantum theory reveals the existence of an additional interaction which takes place between the two electrons and it is governed by the relative orientation between their spins. When these are parallel aligned, the exchange interaction prevents the bonding of the atoms, whereas antiparallel alignment between the spins gives rise to attractive "forces" which tie the hydrogen atoms in a stable molecule. The repulsive and attractive mechanisms of the exchange interaction are direct consequences of the Pauli exclusion principle, which states that no two electrons can be found in the same quantum state, that is they cannot be characterised by identical quantum numbers. This postulate is clearly portrayed when one derives the total wave function of an electronic system; later, we will outline this in detail for the case of two interacting electrons. The "exchange" term names the possibility of a rapid electron transfer between atoms which are brought together; in the hydrogen molecule for example, electrons can switch places and orbit the adjacent protons rather than their local site [38].

The Hamiltonian of a multiparticle system must obey a symmetry property: under the interchange of spatial and spin coordinates, the observed probability densities do not change - the particles are said to be indistinguishable. This in turn requires the wave function describing a multiparticle system to be characterised by an odd or even symmetry. Due to this, particles are separated in two categories: bosons are described using even wave functions, they are characterised by integer spin values and they obey the Bose-Einstein statistics which allows them to occupy the same quantum state simultaneously. Electrons are included in the second category which demands particles to be described in terms of odd functions that do not allow them to crowd into the same quantum state at once, thus obeying the Fermi-Dirac statistics.

We shall further consider how the exchange interaction arises based on the quantum mechanical theory and the description given in [43]. The total wave function describing a system of two electrons can be written as $\psi(q_1, q_2)$, where q_1 and q_2 are the general coordinates (spatial and spin). As we stated earlier, the observed properties must not differ if the two electrons are interchanged, that is equivalent to the following condition:

$$|\psi(q_1, q_2)|^2 = |\psi(q_2, q_1)|^2 \tag{2.11}$$

Equation (2.11) implies that:

$$\psi(q_1, q_2) = \pm\psi(q_2, q_1), \tag{2.12}$$

where the plus sign denotes symmetric wave-functions and the negative sign corresponds to anti-symmetric wave-functions. Anti-symmetry prevents electrons from violating the Pauli exclusion principle. The spin and spatial components of the total wave function $\psi(q_1, q_2)$ can be explicitly separated:

$$\psi(q_1, q_2) = \rho(\boldsymbol{r}_1, \boldsymbol{r}_2)\xi(s_1, s_2) \tag{2.13}$$

If the spatial component is symmetric, the spin term has to be anti-symmetric and vice versa; in this way the total wave function remains anti-symmetric. The two situations correspond to the *singlet* and *triplet* state respectively. In the first case, electrons are paired, their spins align antiparallel and the resultant spin quantum number is 0. In the triplet state, the electrons are unpaired, having their spins oriented parallel with respect to one another while the total spin quantum number is 1. These two cases can be described using the following wave-functions:

$$\psi_S = \frac{1}{\sqrt{2}}[\rho_a(\boldsymbol{r}_1)\rho_b(\boldsymbol{r}_2) + \rho_a(\boldsymbol{r}_2)\rho_b(\boldsymbol{r}_1)]\xi_S, \tag{2.14}$$

$$\psi_T = \frac{1}{\sqrt{2}}[\rho_a(\boldsymbol{r}_1)\rho_b(\boldsymbol{r}_2) - \rho_a(\boldsymbol{r}_2)\rho_b(\boldsymbol{r}_1)]\xi_T, \tag{2.15}$$

where the S and T indices refer to the singlet and triplet states, while a and b denote two distinct orbital states. According to quantum theory, the wave function leads to the energy of a given quantum state. The energies characterising the singlet and triplet states can be calculated using the general formula:

$$E = \int \psi^* \mathscr{H} \psi \, d\boldsymbol{r}_1 \, d\boldsymbol{r}_2, \tag{2.16}$$

Taking into account equations (2.14), (2.15) and (2.16) we can calculate the energy difference between the two states:

$$E_S - E_T = 2\int \psi_a^*(\boldsymbol{r}_1)\psi_b^*(\boldsymbol{r}_2)\mathscr{H}\psi_a(\boldsymbol{r}_2)\psi_b(\boldsymbol{r}_1)\, d\boldsymbol{r}_1 \, d\boldsymbol{r}_2 = 2J, \tag{2.17}$$

where the spin components have been dropped through normalisation. The term noted J is called the exchange integral. In this two electron model, the total spin of the system can be written as: $\boldsymbol{S} = \boldsymbol{s}_1 + \boldsymbol{s}_2$, while $\boldsymbol{S}^2$ is given by $\boldsymbol{S}^2 = \boldsymbol{s}_1^2 + \boldsymbol{s}_2^2 + 2\boldsymbol{s}_1 \cdot \boldsymbol{s}_2$. The squared spin

terms can be written in terms of the spin quantum numbers as: $\boldsymbol{S}^2 = S(S+1)$ and $\boldsymbol{s}^2 = s(s+1)$ respectively. Knowing that S takes the 0 and 1 values as stated earlier, and that s is always $\frac{1}{2}$, the dot product $\boldsymbol{s}_1 \cdot \boldsymbol{s}_2$ can take the following values: $-\frac{3}{4}$ in the triplet state and $\frac{1}{4}$ in the singlet state. As shown in Blundell [43], the Hamiltonian in equation (2.17) can be parametrised using the dot product $\boldsymbol{s}_1 \cdot \boldsymbol{s}_2$:

$$\mathscr{H} = \frac{1}{4}(E_S + 3E_T) - (E_S - E_T)\boldsymbol{s}_1 \cdot \boldsymbol{s}_2 \tag{2.18}$$

We can further modify the Hamiltonian such that we absorb any constants in front of the variable terms. Making use of the newly introduced term J, equation (2.18) becomes

$$\mathscr{H} = -2J\boldsymbol{s}_1 \cdot \boldsymbol{s}_2 \tag{2.19}$$

This equation concentrates the basic information about ferromagnetism and antiferromagnetism as Heisenberg introduced it first [30]. If J is positive, spins will tend to align parallel with respect to each other while for a negative J, spins will align antiparallel. The exchange Hamiltonian in (2.19) describes the interaction between two spins only, but it can easily be generalised for a multi-particle system, as it is the case for any solid material:

$$\mathscr{H}_{exch} = -\sum_{\substack{i \neq j \\ i<j}} J_{ij}\boldsymbol{s}_i \cdot \boldsymbol{s}_j, \tag{2.20}$$

where the summation doesn't include spin pairs twice and hops over self interactions. While not restricted in reality, our numerical model takes into account only the nearest-neighbour contribution to the exchange energy. The constant J_{ij} describes the local isotropic interaction between two adjacent spins, i and j; in more complex materials where the canting between spins gives rise to special magnetic textures such as skyrmions, J needs to be expressed as a tensor, taking into account any anisotropic exchange effects. Calculating the exchange integral is not an easy task; that is why J is often extracted from first principles methods or approximated using easily accessible parameters such as the Curie temperature. The two electron model discussed earlier refers to the mechanism of direct exchange; if the degree of orbital overlapping is not well satisfied, other exchange routes need to be considered.

In certain materials such as oxides or fluorides, an indirect type of exchange arises, called superexchange: the interaction between two non-neighbouring atomic sites is mediated by an intermediate link. A good example is a crystal of MnO; in this case, O^{2-} mediates the interaction between two Mn^{2+} ions by donating up and down spins, leading to an antifer-

romagnetic arrangement of the manganese ions [44]. Another type of indirect exchange mechanism arises in metals: here, spins can polarise conduction electrons which in turn due to their delocalised nature transfer the polarisation to another atomic site. This mechanism is known as the Ruderman-Kittel-Kasuya-Yosida (RKKY) interaction or the itinerant exchange. We mentioned earlier the possibility of an anisotropic type of exchange. In materials which lack an inversion symmetry and exhibit a strong spin-orbit coupling, spins can interact through the Dzyaloshinskii-Moriya mechanism which favours their orthogonal alignment with respect to each other.

4.3 Magnetic anisotropy

In the previous section, we saw how the Heisenberg exchange term takes into account the relative orientation between spins without considering an external frame of reference - this favours an isotropic magnetism. Experimentally it is shown otherwise - magnetic properties differ as we vary the direction of our measurements. Anisotropy is at the origin of hysteresis and coercivity; later in this chapter we will discuss these connecting links. Several types of magnetic anisotropies are known, both intrinsic or artificial. The best known example and the most relevant type in our work is the intrinsic magnetocrystalline anisotropy: the energy of a given magnetic material is lowered when its magnetisation aligns along specific crystallographic directions or planes, called easy-axes and planes respectively. Similarly, there are hard planes and axes which increase the total energy of the crystal if the magnetisation points along them. Consequently, we will be able to magnetise a sample using a lower magnetic field if this is applied in the direction of the EA.

Within a crystal, there are three main types of interactions or couplings: we already discussed the spin-spin contribution or the exchange interaction. We also briefly mentioned how in certain materials, the orbital contribution to the total magnetic moment may be neglected. This is known as quenching and it arises as a result of the second coupling mechanism: the crystal symmetry favours specific orientations of the orbitals. Naturally, there is a third coupling linking the spin and orbital motions of the electron. An attempt to polarise the spin will modify the orientation of the electron orbit. Since the latter is coupled to the lattice, it will resist the change in angular momentum and it will also prevent the reorientation of the spin. The anisotropy energy is therefore related to the work required to overcome the spin-orbit coupling. The simplest form of magnetocrystalline anisotropy is referred to as uni-axial. Co is the only material in the ferromagnetic triad (Fe,Co,Ni) which is characterised by this type of anisotropy. Its hexagonal structure presents an EA along the

c direction of the crystal. Every other direction perpendicular to this axis is experimentally shown to be a hard direction.

Generally, the anisotropy energy is defined using a spatial function which takes into account the symmetry of the lattice. For uni-axial crystals, we can use the following mathematical relationship to express the anisotropy energy:

$$E_{uni} = K_1 \sin^2\theta + K_2 \sin^4\theta + .., \tag{2.21}$$

where θ represents the angle between the magnetisation vector and the EA while K_1 and K_2 are known as anisotropy constants. This series expansion can be defined both in terms of $\sin\theta$ and $\cos\theta$ powers and it is usually limited to the first two terms. If K_1 and K_2 are both positive, the anisotropy energy has a minimum for $\theta = 0°$ which corresponds to the magnetisation vector aligned on the EA , see Figure 2.7.

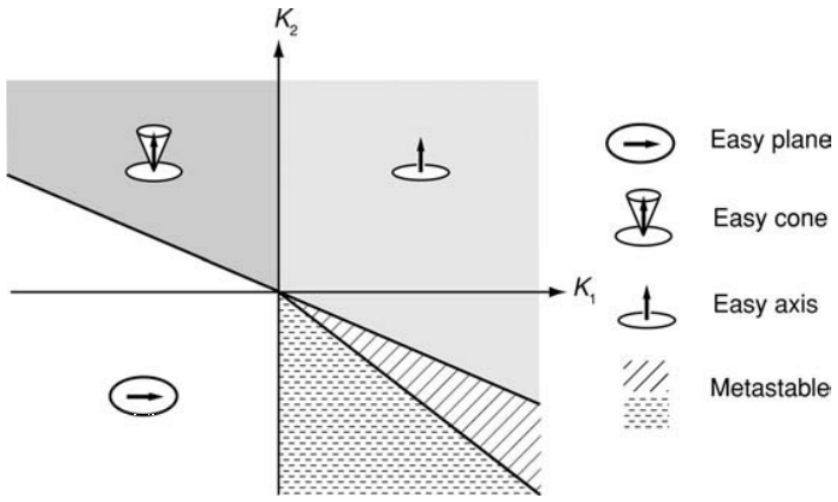

Figure 2.7: Uni-axial easy directions and planes for different values of the anisotropy constants K_1 and K_2. In the metastable region, the energy is minimised for $\theta = 0$ and $\theta = \frac{\pi}{2}$. Figure extracted from [45].

If however the two constants are negative, the energy minimum will be satisfied for $\theta = 90°$ and the magnetisation can lie anywhere in an easy plane. An interesting case arises when $K_1 < 0$ and $K_2 > -\frac{1}{2}K_1$; in this situation the anisotropy energy is minimum in an easy cone. In cubic crystals such as Fe or Ni, the anisotropy energy is defined using a more complicated expression. The body centered cubic (bcc) structure of Fe presents an EA in the $\langle 100 \rangle$ direction. For Ni, its face-centered (fcc) structure gives rise to an EA across the diagonal direction $\langle 111 \rangle$. In our atomistic model, we will be including an uni-axial anisotropy term in the total

Hamiltonian:

$$\mathcal{H}_{uni} = -\sum_i k_u^i (\boldsymbol{s}_i \cdot \boldsymbol{n})^2, \tag{2.22}$$

where k_u^i represents the local anisotropy constant associated with each atomic site and $\boldsymbol{n}$ gives the direction of the EA, traditionally chosen as Oz in an $Oxyz$ cartesian coordinate system. Another type of anisotropy is related to the shape of the magnetic material. A prolate ellipsoid will be easier to magnetize along its long axis; the explanation can be found calculating the demagnetizing fields across its principal axes. Simply put, as the distance between two magnetic poles increases the corresponding demagnetizing field will become smaller, which in turn will favour a quick magnetic response along that direction. Magnetic anisotropy can also be induced through applied stress or by annealing; both of these methods have the capacity to rearrange the atomic structure in such a way that anisotropy can result. As a final comment, we should mention that the magnetic anisotropy of a material drops as the temperature increases; its decay is usually faster compared to the loss of magnetisation. This aspect is particularly important in the recording media industry as it provides the stepping stone for the HAMR technology: while coercivity is greatly lowered at high temperatures, the preserved magnetisation can be polarised during the writing process.

5 DOMAIN THEORY AND MAGNETISATION PROCESSES

In this section, we will show how magnetic domains are formed and why they are favoured when magnetic materials grow in size. We will also discuss the transition regions known as domain walls based on the balance between the anisotropy and exchange energies. Furthermore, we shall introduce the Stoner-Wohlfarth theory able to explain the limit of coherent rotation in magnetic systems. Finally, we will give a short description of the main coercivity mechanisms which will help us understand reversal processes in perfectly homogeneous crystals and composite media.

5.1 Magnetic domains

When Weiss postulated the idea of the molecular field H_m, theory and experiments appeared to be contradictory; one can extract an approximate value for H_m knowing that a ferromagnet will lose its magnetisation at the Curie point [19]: $\mu_0 \mu_B H_W \sim k_B T_C$, where μ_0 is the vacuum permeability. Applying this relationship for Fe we obtain a molecular field of strength $H_m \sim 10^9 A/m$ which in more familiar units is roughly equivalent to 1200 T. Under these considerations, the obvious expectation would be to always observe fully saturated ferromagnets.

In practice however, not only we can have fully demagnetised samples, but the polarising magnetic fields used experimentally, are considerably much lower. In order to circumvent this, Weiss introduces the notion of magnetic domains: a ferromagnet is divided in regions - domains - magnetised to saturation such that the local degrees of freedom are highly collinear - see Figure 2.8.a). The direction of the magnetisation $\boldsymbol{M}_i$ within each domain, varies across the sample such that when one takes the integral over the volume $\boldsymbol{M} = \int_V \boldsymbol{M}_i$, a demagnetised state can result. The separation region between two domains is called a domain wall. Later, we will treat this notion in more detail as it will be extensively used throughout the thesis.

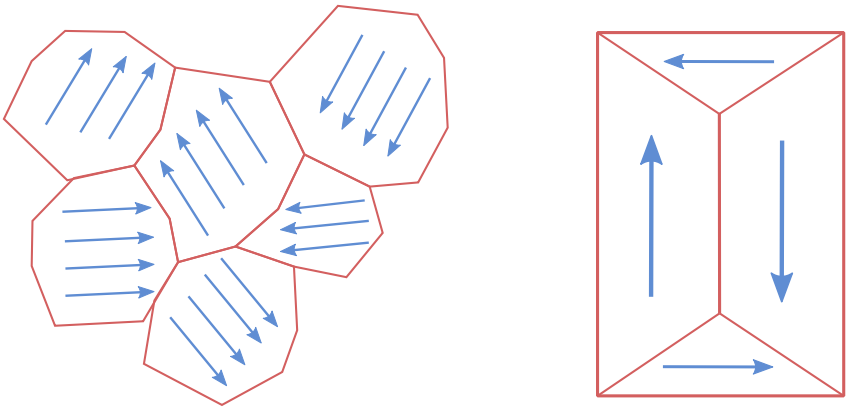

a) b)

Figure 2.8: Visual representations of: a) magnetic domains within which the collective degrees of freedom are magnetised close to saturation as postulated by Weiss; b) minimisation of the magnetostatic energy through the enclosure of the magnetic flux lines.

An indirect validation of the magnetic domains idea has been suggested for the first time in 1919 by Barkhasuen [46]. In his experiments, a coil was wound on a magnetic sample and the circuit connected to an amplifier and subsequently a speaker. Magnetising the sample using an external field, a crackling sound could be heard; initially, it was thought the noise was due to sudden rotations of the local magnetisation $\boldsymbol{M}_i$ vectors. It was later accepted that the Barkhausen effect arises due to impurities in the crystal which interfere with the motion of domains [47]. Measuring $M-H$ curves, it can be seen that the magnetisation process is not continuous no matter how smoothly the field is swept. Magnetic domains have since been observed in a variety of ways. One of the most common methods was introduced by Bitter [48]. He made use of fine magnetic particles spread across the surface of a ferromagnetic crystal. The stray field arranges the dust of particles in patterns which can later be observed in a microscope. An interesting Bitter-like approach makes use of magnetotactic bacteria as imaging agents [49]. Other techniques involve the Faraday and Kerr magneto-optical effects. More recently, magnetic domains have been visualised three dimensionally using a neutron

tomography method [50].

The existence of magnetic domains can be explained introducing the magnetostatic energy:

$$E_{ms} = -\frac{1}{2}\mu_0 \int_V \boldsymbol{M} \cdot \boldsymbol{H}_d \, dV, \tag{2.23}$$

where $\boldsymbol{H}_d$ represents the demagnetising field. This equation describes the interaction between the magnetisation of a crystal and the field created as a result of its magnetised state. In the absence of magnetic domains, the crystal would be characterised by a large demagnetising field $\boldsymbol{H}_d$, pointing opposite with respect to $\boldsymbol{M}$, thus maximising the energy term in (2.23). For this reason, domains are naturally favoured; their nucleation can lead to a cancellation of the strong $\boldsymbol{H}_d$ field as the flux lines close within the crystal - see Figure 2.8.b). This in turn minimises the total magnetostatic energy. There are however situations in which the energy gain is far less than the input needed to sustain the domain structure. For a spherical particle, the magnetostatic energy is directly proportional to its radius cubed $\sim R^3$, whereas the energy stored within the transition regions between domains is proportional to $\sim R^2$ [38]. As the former drops faster, for a critical radius the existence of domains is no longer favoured and the sample becomes a mono-domain particle. Generally, particles with a diameter smaller than 1000 Å will undergo this transition.

5.2 Domain walls

The single-domain limit is a rough approximation for typical domain wall widths. The size of these transition regions depends on the balance between the magnetocrystalline and the exchange energies. The former term favours narrow domain walls; this way, abrupt changes in the orientation of the spins will limit potential deviations of the magnetisation from the easy directions. On the other hand, the exchange contribution promotes wide separation regions between magnetic domains; this is easily explained going back to equation (2.19). This energy term is minimised if a spin is parallel to its neighbour; because of this, small rotations of the spins are favoured in the wall regions, which in turn increases their width.

Felix Bloch made the first theoretical investigation of domain walls in a classical paper from 1932 [51]. Following his model and the guidelines in [52], we will deduce an initial mathematical expression which gives us the energy of a domain wall. In Figure 2.9, one can see a chain of spins gradually changing their projection on a vertical axis (Oz) from $+1$ to -1, this being equivalent to a rotation from 0° to 180°. We can consider the outermost spins as part of two different infinite domains, while the rotation takes place in the finite width of a domain wall. For generality, we will assume N spins within the wall and an average angle of

$\theta = \frac{\pi}{N}$ between them. If two spins are parallel their energy is $-J$ according to equation (2.20).

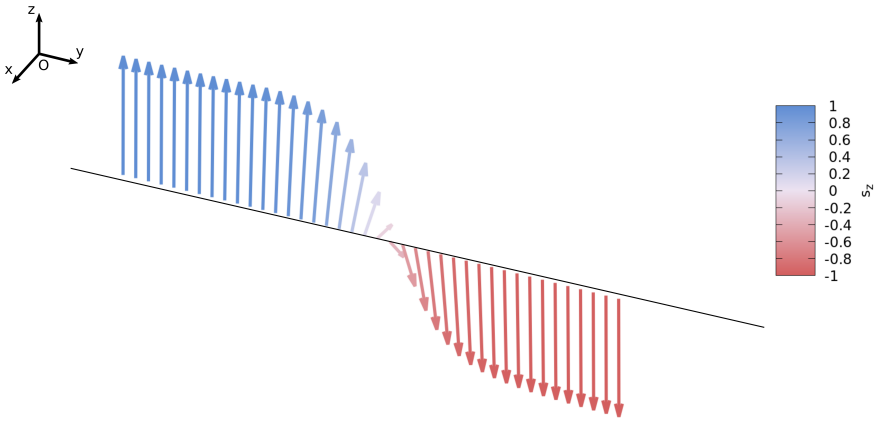

Figure 2.9: Visual representation of a Bloch domain wall. The spins in the system gradually change their projection on the Oz axis - see colorbar. A rotation takes place in the Oxz plane; there is no spin component on the Oy axis. This particular example is called an 180^o wall due to the antiparallel spins which it separates.

A small displacement with an angle θ requires an energy of $-J\cos\theta$. The energy difference between these two situations gives us the exchange contribution of two spins in the formation of a domain wall: $E_{int} = J(1-\cos\theta)$. Considering for simplicity an extra neighbour such that we have N interactions, the total exchange energy in the system is:

$$E_{ex} = NE_{int} = NJ(1-\cos\theta) \tag{2.24}$$

Making use of the first two terms in the Taylor expansion of the cosine function and knowing that $\theta = \frac{\pi}{N}$, equation (2.24) becomes:

$$E_{ex} = \frac{J\pi^2}{2N} \tag{2.25}$$

Each atomic site is characterised by an uni-axial anisotropy term which on its own leads to an energy penalty for each rotation of the spins. Assuming a reference energy of zero, the total anisotropy contribution in the system is:

$$E_{anis} = \sum k_u \cos^2\theta \tag{2.26}$$

Equation (2.26) can be replaced with a continuum expression for sufficiently large values of

spins:

$$E_{anis} = \frac{1}{d\theta} k_u \int_0^{\pi} \cos^2\theta d\theta = \frac{1}{d\theta} k_u \int_0^{\pi} \frac{(1+\cos 2\theta)}{2} d\theta = \frac{1}{d\theta} k_u \frac{\pi}{2} \tag{2.27}$$

Using our approximation for the angle θ, the total anisotropy energy is:

$$E_{anis} = \frac{k_u N}{2} \tag{2.28}$$

Adding together the contributions in (2.25) and (2.28) we obtain the total energy:

$$E_{total} = E_{ex} + E_{anis} = \frac{J\pi^2}{2N} + \frac{k_u N}{2} \tag{2.29}$$

In order to compute the domain wall energy, we first need to find the equilibrium thickness - equivalent in this description with the equilibrium number of spins in the wall; this can be done by minimising equation (2.29) with respect to N:

$$\frac{dE_{total}}{dN} = 0 \rightarrow N^* = \pi\sqrt{\frac{J}{k_u}} \tag{2.30}$$

As we can see, N^* is directly proportional to $J^{1/2}$ and inversly proportional to $k_u^{1/2}$, in accord with our earlier discussion - regarding the width of the wall as the competition between exchange and anisotropy. Having found the number of atomic sites which satisfies the minimum condition, we can now calculate the Bloch domain wall energy:

$$E^*_{DW} = \frac{J\pi^2}{2N} + \frac{k_u N}{2} = \pi\sqrt{Jk_u} \tag{2.31}$$

The wall energy is usually expressed as a surface density, but considering an unitary lattice spacing we can limit ourselves to the notation above. The domain wall energy we obtained is an approximation due to our initial hypothesis: $\theta = \frac{\pi}{N}$. A more accurate approach to our problem makes use of the variational calculus. In a continuum way, the total energy in (2.29) is given by the following expression, as suggested by Skomski [36]:

$$E = L^2 \int_{-\infty}^{\infty} \left(A\left(\frac{\partial\theta}{\partial y}\right)^2 + K\cos^2\theta \right) dy, \tag{2.32}$$

where L^2 is the area of the wall, while A and K are the micromagnetic equivalents of J and k_u. While k_u and J are both expressed in Joules, the exchange stiffness A is measured in J/m and K is given in energy density units J/m^3. The exact energy of the Bloch wall can be derived by minimising the integral in (2.32) with respect to $\theta(y)$ and solving the corresponding Euler-

Lagrange equation. The calculations yield the following energy density for the Bloch wall:

$$E/L^2 = 4\sqrt{AK} \tag{2.33}$$

In order to make use of equation (2.33),we need to adapt it to our atomistic picture:

$$E_{DW} = 4\sqrt{\frac{J}{2}k_u}, \tag{2.34}$$

where the exchange constant J is normalised by a factor of 2 in order to account for the contribution of a single spin rather than the whole interaction. See Table 1 in next chapter for detailed link between micromagnetic and atomistic parameters. We shall also point out a second relationship we will be using later in the results section; according to the description in Skomski [36], the magnetisation profile at equilibrium is given in the continuum approach by the following expression:

$$m_z(y) = -\tanh\left(y\sqrt{\frac{K}{A}}\right) \tag{2.35}$$

In our atomistic picture, equation (2.35) becomes:

$$s_z(y) = -\tanh\left(y\sqrt{\frac{2k_u}{J}}\right) \tag{2.36}$$

The y coordinate can be normalised to the lattice spacing of the atomic system, thus we will consider it an adimensional quantity.

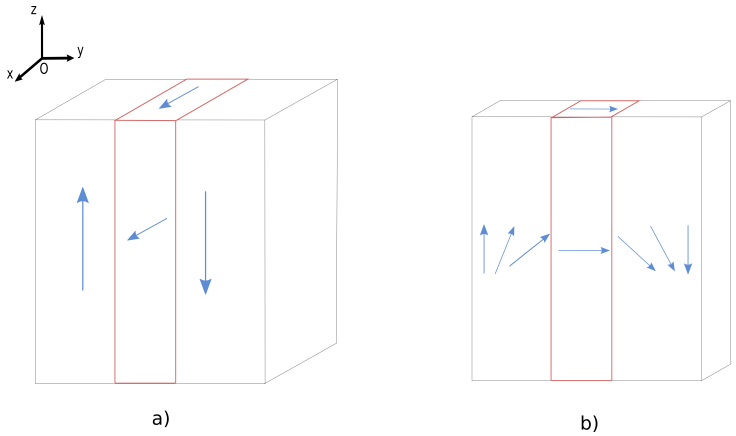

Figure 2.10: Domain walls: a) Bloch - the rotations of the spins occur in the Oxz plane; this favours the appearance of magnetic free poles at the surface of the sample. b) Néel- the spins rotate in the Oyz plane; this particular configuration gives rise to free magnetic poles on the surface of the wall.

As a final remark, we shall mention the existence of another type of domain wall. If the thickness of a magnetic sample becomes smaller than the width of the wall, the Bloch rotations will no longer be favoured. Louis Néel showed this arises due to the stray field created by the magnetic poles at the surface of the sample -see Figure 2.10.a) - which will lead to an overall increase in the magnetostatic energy. For this reason, domain walls in thin materials will exhibit a Néel type of rotation in order to reduce the stray field effects; this will lead to magnetic free poles on the surface of the wall - see Figure 2.10.b).

5.3 Stoner-Wohlfarth theory

The perpendicular recording process relies on the ability to switch the magnetisation from the "up" state to the "down" state using an external magnetic field. Within the macrospin approximation, one can use the Stoner-Wohlfarth (SW) theory in order to describe the magnetisation process, that is the relationship between $\boldsymbol{M}$ and $\boldsymbol{H}$. In a single-domain particle, all internal magnetic moments are said to undergo coherent rotations, meaning there is no phase lag between them and their directions are parallel. In the absence of a field, the magnetisation will lie in the direction of the EA; a small external perturbation will deviate the $\boldsymbol{M}$ vector from its equilibrium position giving rise to a reversible magnetisation increase in the direction of the field. The competition between the Zeeman and anisotropy contributions will give the deviation angle as well as define the limit between reversible and irreversible processes. For example, a particle initially magnetised in the $+z$ direction can switch in the opposite direction in the presence of a sufficiently large and negative field; after $\boldsymbol{H}$ is reduced to zero, the magnetisation will remain on $-z$, thus an irreversible process occured.

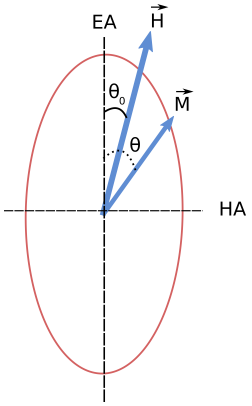

Figure 2.11: Schematic representation of the Stoner-Wolhfarth problem. EA and HA denote the easy and the hard axes respectively.

Stoner and Wolfarth applied the coherent approximation in the case of a prolate spheroid characterised by shape anisotropy along its major axis [53]. In order to preserve its traditional value, we will be unfolding the SW description in micromagnetic units, outlining its atomistic equivalent at the end. In Figure 2.11, one can see the visual representation of the problem. The energy of the SW particle is given by:

$$E_{SW} = -KV\cos^2\theta - \mu_0 H M_S V \cos(\theta - \theta_0), \tag{2.37}$$

where M_S is the saturation magnetisation, V is the volume of the particle, θ is the angle between $\boldsymbol{M}$ and the EA, while θ_0 gives the angle between $\boldsymbol{H}$ and the same reference axis. The extremum values in equation (2.37) are found taking the first-order derivative of the energy with respect to the angle θ:

$$\frac{\partial E_{SW}}{\partial \theta} = 0 \tag{2.38}$$

An extremum point will correspond to a stable state or an energy minimum if the following condition holds:

$$\frac{\partial^2 E_{SW}}{\partial \theta^2} \geq 0 \tag{2.39}$$

The energy landscape $E_{SW} = E_{SW}(\theta)$ may be characterised by either one or two energy minima depending on the competition between anisotropy and the external field. For a more suitable comparison, an anisotropy field can be defined: $H_K = \frac{2K}{\mu_0 M_S}$. Figure 2.12) shows which are the stable energy configurations of a SW particle for different H/H_K ratios, and assuming the external field is applied at an angle $\theta_0 = \pi$ with respect to the EA. If $H > H_K$, the

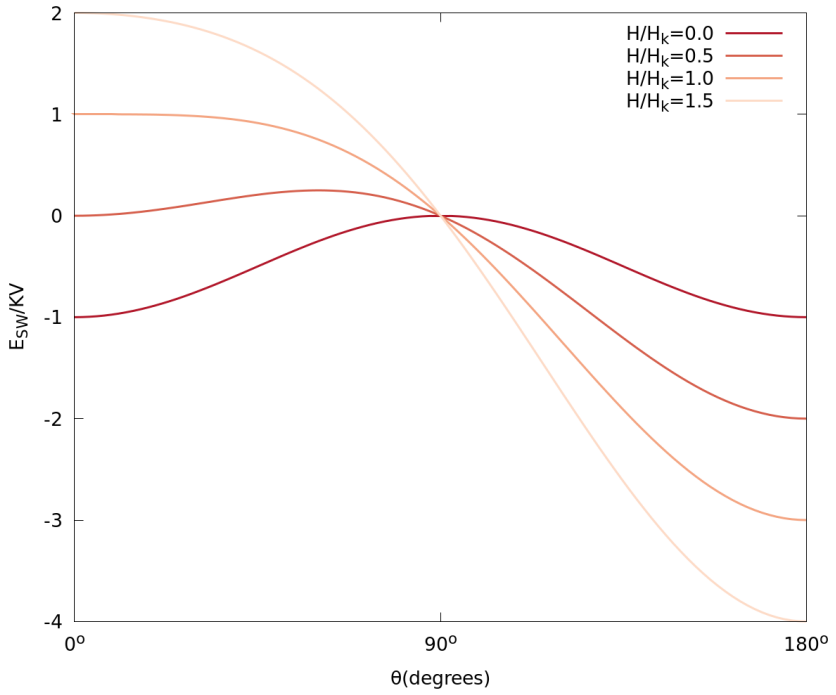

Figure 2.12: Energy landscapes for a Stoner Wohlfarth particle assuming different H/H_K ratios. The direction of the field corresponds to $\theta_0 = \pi$.

minimum energy corresponds to the magnetisation being aligned parallel to the direction of the field: $\theta = \theta_0$. For $H < H_K$, the energy map presents two possible minimum configurations at $\theta = 0°$ and $\theta = 180°$; any switching between these equilibrium positions requires an energy

input able to overcome the local barriers. The $H = H_K$ case corresponds to an irreversible change in the energy landscape for which one of the stable configurations vanishes. The difference between the maximum and minimum energy defines the global barrier:

$$\Delta E_{SW} = KV\left(1 - \frac{H}{H_K}\right)^2 \tag{2.40}$$

In a simple manner, equation (2.40) gives us a thermal stability measure in the magnetic recording process. For a given ratio between ΔE_{SW} and the $k_B T$ factor, spontaneous switching can occur with a probability governed by the Néel-Arrhenius law. Shrinking the volume of the particles will lead to a decrease in stability; in perpendicular recording media, storage densities of over 1Tb/in^2 can be achieved using highly anisotropic materials that compensate the downscaling effect. The power law given in (2.40) needs to be adjusted according to the problem at hand.

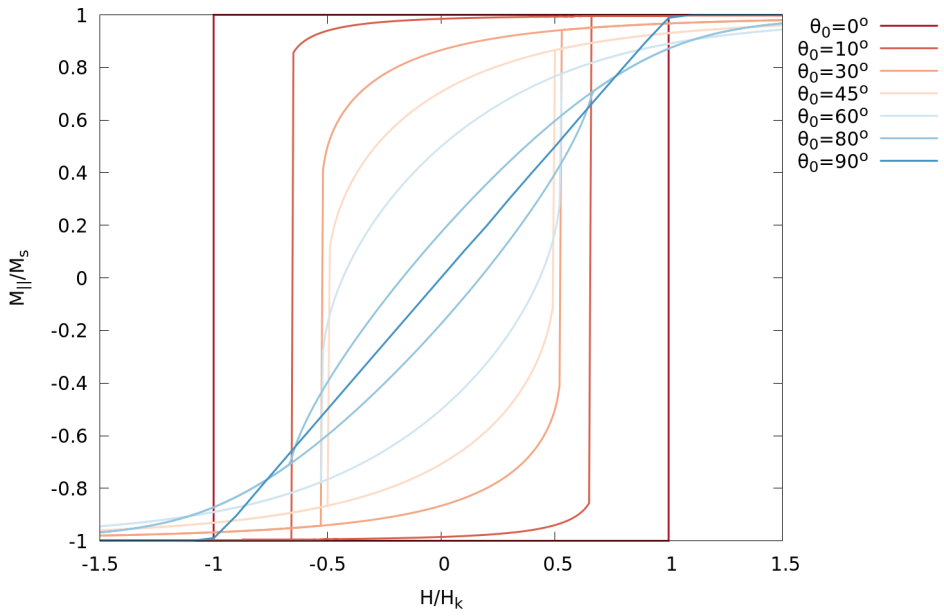

Figure 2.13: Hysteresis loops for a Stoner-Wohlfarth particle as a function of the θ_0 angle . $M_{||}$ represents the magnetisation projection on the direction of the field.

The Stoner-Wohlfarth model can also be used to understand the basic concepts of hysteresis. This behaviour is characteristic to ferromagnetic materials; the *hysteresis* term derived from Greek - meaning "to lag behind" - was coined by James Ewing in 1881. In the absence of any competing factor, the magnetisation would always align on the direction of the applied field. An anisotropy component alters the energy landscape and prevents the switching

process until a critical field value is reached. In Figure 2.13), one can see different hysteresis curves for a SW particle. As the angle between the EA and the applied field increases from 0° to 90°, the total area of the loop decreases. Consequently, the coercivity will be lowered continuously from H_K to 0. The field required to switch the magnetisation from +1 to −1 has a different variation; it decreases between $\theta_0 = 0°$ and $\theta_0 = 45°$ to a minimum of $H_K/2$, after which it goes back to H_K for $\theta_0 = 90°$. The irreversibility of the magnetisation process vanishes completely when the field is aligned on the hard-axis.

Making use of equations (2.22) and (2.10), we can write the energy of a SW particle in an atomistic fashion:

$$E_{SW} = -k_u \cos^2\theta - \mu_s H \cos(\theta - \theta_0) \tag{2.41}$$

The anisotropy field becomes $\frac{2k_u}{\mu_s}$ and the energy barrier is given by: $k_u(1 - \frac{H}{Hk})^2$. In the next chapter, we will be outlining the direct correlation between the atomistic and micromagnetic parameters.

5.4 Coercivity mechanisms

While remanence gives the material property to preserve information in the absence of an external field, coercivity represents a stability measure in the remanent state. The latter parameter needs to be sufficiently high in order to prevent any unwanted losses or changes in the recorded data. Early studies [54, 55] showed how the theoretical coercivities do not match the experimental values; this overestimation is also valid for the SW model discussed earlier. Despite its simplicity, the SW description is still widely used since it provides a basic coercivity explanation. The discrepancy between theory and practice constitutes Brown's paradox and its resolution is found taking into consideration inhomogeneities in a magnetic material: atomic vacancies, dislocations or grain boundaries [56].

Two principal mechanisms can be used to describe coercivity. The first one is known as nucleation; this term is associated with the field required to destabilize a magnetic system from its saturated state. As it can be seen from the hysteresis loops in Figure 2.13), at an early stage the magnetisation will not experience any changes. For a critical value known as the nucleation field, M becomes smaller than M_S. A visual analogy of this effect is the bending of a metallic beam [57]. Under a certain force applied to both ends of the beam, the material won't change its shape. At a critical value of the force, the beam will be slighly arched. A nucleation process can extend over the crystal volume - as it is the case with the SW model - or it can take place locally. In micromagnetics, different nucleation paths or modes arise solving an eigenvalue problem based on the linear Brown equations [19]. For perfectly homogeneous

crystals, the coherent reversal represents one of the solutions to this problem. Two other exact solutions can be found for single-domain particles: the curling and the buckling modes. Curling will be favoured in order to reduce the magnetostatic energy of the sample; this type of reversal leads to vortex-like spin configurations in a plane perpendicular to the EA - see Figure 2.14.

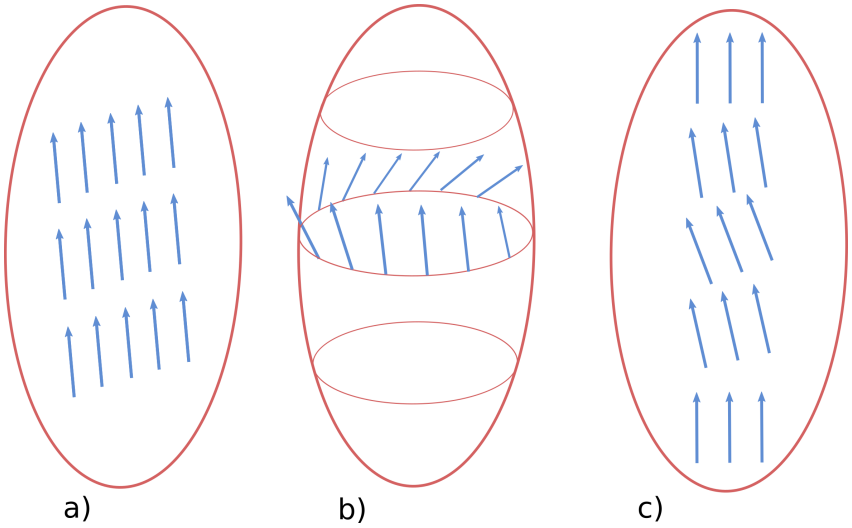

Figure 2.14: Visual representation of the reversal paths in single-domain particles: a) coherent; b) curling; c) buckling.

The buckling mode is the third nucleation type which can occur in prolate spheroids and it consists of a sinuisoidal variation of the magnetisation along the major axis of the sample [58]. The presence of defects in real crystals inserts an extra level of complexity in the study of their nucleation modes; the reversal types discussed earlier will no longer be preferred. Once dimensions increase over the coherent limit, multiple magnetic domains will form. If the sample is initially saturated, the material magnetisation will be uniform across the entire volume. For a given H_n field value, a local nucleation will lead to a reverse domain which will extend throughout the system via domain wall motion - see Figure 2.15. In certain cases, H_n is sufficiently strong to drive the domain wall across the material volume until the reversal process is complete - it is said that nucleation is the prevalent coercivity mechanism.

The coercive field H_c is traditionally a positive quantity while the nucleation field H_n is by convention negative. The relationship between these two parameters can be generally described using the following inequality: $H_c \geq -H_n$ - while in perfect crystals they are approximately equal. In some approaches, the coercivity is directly linked to the anisotropy field using a proportionality factor: $H_c = \sigma H_K$ [59]. If the right hand side term of the aforementioned inequality is positive, H_n is in the second quadrant of the hysteresis loop. As

the nucleation field becomes more negative, the stability of the remanent state increases in reverse fields, another important aspect in magnetic recording [60].

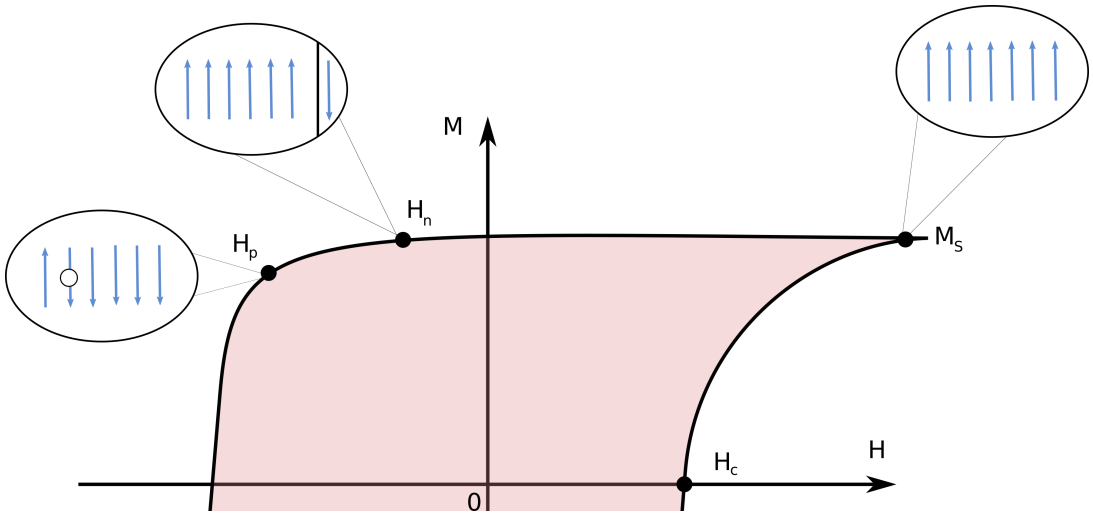

Figure 2.15: Hysteresis crop showing the reversal process in a multi-domain system: if the sample is initially saturated in the +z direction, a reduction in the field will lead to a domain wall nucleation at H_n which will then propagate through the system. If defects arise, a pinning field H_p will be required in order to "push" the wall over the energy barrier and continue the reversal process.

After a reverse domain is formed, its motion will not always be free of impediments; crystal imperfections will pin the wall preventing the reversal process - this effect is known as the second coercivity mechanism. There are two principal pinning methods depending on the size of the defects. When inhomogeneities are comparable with the domain-wall width, a strong pinning occurs. In the region of the defect, the exchange and anisotropy values will differ from the other parts of the crystal. The domain wall can be trapped in these regions if its energy is lowered by the pinning center; the opposite case creates an energy barrier needed to be crossed in order for the reversal process to continue. If the domain wall encounters multiple small defects, it is said the pinning is weak [45]. All real magnetic materials present impurities; as such, the pinning mechanism will always influence the reversal process. The crackling sound in the Barkhausen effect is given by a domain wall successfully moving past a defect. This transition takes place at a critical field value, tradionally named the pinnning field H_p. However, this term could be misleading and it is more suitable to consider it as a "de-pinning" parameter.

The reversal process in ES media combines both the nucleation and pinning effects. Initially, a domain wall is nucleated in the soft material. It then propagates through the system until it meets the soft-hard interface; when the applied field is sufficiently strong, the

wall will overcome the pinning effect and it will be pushed into the hard phase.

In practice it is not easy to differentiate between the two coercivity mechanisms. Ideally, the hysteresis loops for a given material should present two critical points from which H_p and H_n can be obtained. In some cases, defects can act both as nucleation and pinning centers leading to a self-pinning effect - this is reportedly the dominant coercive mechanism in some permanent or composite magnetic structures [61].

Numerical model

This chapter shall introduce the main aspects required to understand the numerical model implemented throughout our project. Firstly, we shall describe how the spin chain structures are generated as well as the way we obtain the input parameters. Furthermore, we will discuss a series of concepts from optimisation theory culminating with the Lagrange multiplier method. Since we are dealing with an energy minimisation problem, we will introduce the steepest descent algorithm after which we will make a qualitative comparison with the dynamic approach based on the Landau-Lifshitz-Gilbert equation. Finally, we will give a general review of the algorithm we use and describe a series of improvements we made in the numerical procedure in order to limit the errors.

1 SPIN SYSTEM: PARAMETERS AND GENERATION

The numerical model used throughout the thesis, generates a collection of N atomic sites, the total energy of the system being given by summing the Zeeman, exchange and anisotropy contributions given in equations (2.10),(2.20) and (2.22):

$$\mathscr{H}_{total} = -\sum_i \mu_s^i \boldsymbol{s}_i \cdot \boldsymbol{H} - \sum_{\substack{i\neq j \\ i<j}} J_{ij}\boldsymbol{s}_i \cdot \boldsymbol{s}_j - \sum_i k_u^i (\boldsymbol{s}_i \cdot \boldsymbol{n})^2 \tag{3.1}$$

The pre-factors μ_s^i, J_{ij} and k_u^i in equation (3.1) are referred to as atomistic parameters; as we previously suggested, these can be inferred from DFT calculations but the procedure is often tedious requiring considerable computational effort. The faster route is linking atomistic quantities to macroscopic parameters as it was previosuly shown in [62]. As such, the local microscopic magnetic moment μ_s is obtained from the saturation magnetisation M_s of the material:

$$\mu_s = \frac{M_s a^3}{n_{at}}, \tag{3.2}$$

where a is the lattice spacing and n_{at} gives the total number of atoms in the unit cell. In a similar manner, the anisotropy constant k_u is obtained from its macroscopic correspondent:

$$k_u = \frac{Ka^3}{n_{at}} \tag{3.3}$$

In our simulations, we will be considering a simple cubic (sc) structure which yields $n_{at} = 1$. The exchange constant J_{ij} can be obtained using the Curie temperature of the material:

$$J_{ij} = \frac{3k_B T_c}{\epsilon z}, \tag{3.4}$$

where k_B represents the Boltzmann constant, z is the number of nearest neighbours and ϵ is a correction factor which varies according to the crystal structure of the material [63]. In the table below, we summarise the conversion factors between the atomistic and micromagnetic parameters as well as display their respective units of measure.

Atomistic parameter	Micromagnetic parameter	Conversion factor
$\langle J_{ij} \rangle$ = Joules	$\langle A \rangle$ = Joules/meter	$1/2a^*$
$\langle \mu_s \rangle$ = Joules/Tesla	$\langle M_s \rangle$ = Ampere/meter	n_{at}/a^3
$\langle k_u \rangle$ = Joules	$\langle K \rangle$ = Joules/cubic meters	n_{at}/a^3

Table 1: Atomistic and micromagnetic physical quantities: units of measure and conversion factors. *This relationship is valid for a simple cubic system [36].

The majority of the results presented in the next chapters were obtained via a *C++* code developed in the first phase of the project. The code is modular offering the possibility for later modifications. The initialisation module sets up the starting positions of the spin vectors, assigns the list of interactions and calculates the ground state energy of the system. For all our simulations, the directions of the EA vector as well as the applied field will be chosen as *Oz*. Unless specified, the initial configuration of the spins will be homogeneously assigned to $\langle 0,0,1 \rangle$ as seen in Figure 3.1a). In our simple cubic structures the atomic sites are centered within the unit cell. In order to obtain a faster simulation procedure we choose to limit our study to 1D spin systems - see Figure 3.1b). Approximating magnetic grains to be perfect cuboids, we assume that during the reversal process spins will exhibit in the bulk material an identical rotation across any horizontal slice parallel to the Oxy plane. For this reason, we reduce the analysis to vertical chains such that we capture the entire reversal process in each slice while reducing the computational effort at the same time. Ultimately, any result could be extrapolated for the bulk material via a proportionality factor which takes into account

the total number of spin chains in the system. Throughout the rest of the thesis we may also refer to the 1D structures as *grains*.

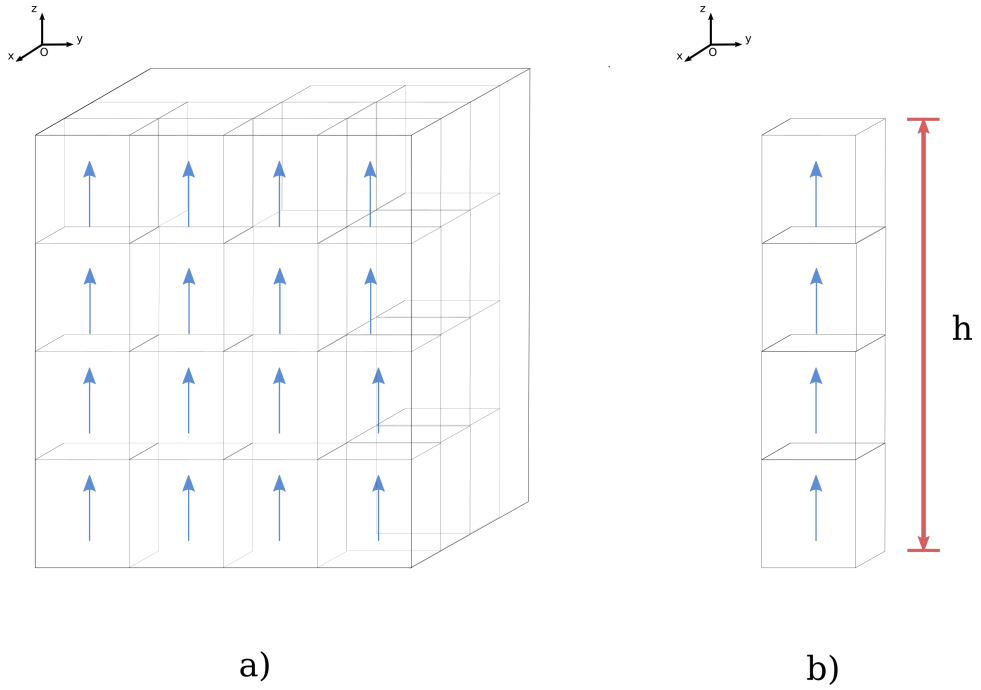

Figure 3.1: Visual representation of the initial spin configuration - equivalent to the ground state - in the bulk a) and the cropped system b) respectively. h is the height of the grain.

2 THE METHOD OF LAGRANGE MULTIPLIERS

In many numerical problems, the aim is to find the set of input parameters which "optimises" the output of a given system. In this work for example, we are seeking those paths of reversal which minimise along their way the energy of a given spin chain system. This approach has its theoretical basis in a stand-alone and evergrowing branch of mathematics, known as *optimisation theory*. In this section, we shall briefly discuss strategies used to solve constrained optimisation problems. We will introduce the method of Lagrange multipliers in its general mathematical form and we will later make use of visual representations aimed at facilitating its understanding.

2.1 General description

Let us consider a general function $f(\phi_1, \phi_2, .., \phi_N)$ defined on an N-dimensional space; formally, optimisation refers to the maximisation or minimisation of the function f with respect

to its variables $\boldsymbol{\phi} = \boldsymbol{\phi}(\phi_1, \phi_2, .., \phi_N)$, where $\boldsymbol{\phi}$ is a vectorial quantity defined on the same N space. Typically, the required solutions need to satisfy a series of *constraints*, which in turn translates to a restriction over the space we are allowed to search for the optimum ϕ_i variables. This reduced space is called the "feasible" region and it consists of all points which fulfill the constraints but do not necessarily satisfy f. In a mathematical way, the optimisation problem can be written as follows:

$$\min_{\boldsymbol{\phi}} f \text{ or } \max_{\boldsymbol{\phi}} f, \quad \text{such that } g_i(\boldsymbol{\phi}) = 0, \tag{3.5}$$

where $g_i(\boldsymbol{\phi}) = 0$ are known as equality constraints. We can also introduce a second type of restrictions making use of inequality constraints:

$$\min_{\boldsymbol{\phi}} f \text{ or } \max_{\boldsymbol{\phi}} f, \quad \text{such that } g_i(\boldsymbol{\phi}) \leq 0 \tag{3.6}$$

According to Bertsekas [64], there are three main approaches used to solve optimisation problems. The first method is rather obvious; supposing f is required to be minimised, we select an initial point $P = P(\boldsymbol{\phi}_0)$ inside the feasible region and we move towards the solution in successive directions $\boldsymbol{d}_k$ which need to satisfy two conditions: a) $\nabla f \cdot \boldsymbol{d}_k < 0$ stating that $\boldsymbol{d}_k$ needs to be a descent direction and b) the new points $P(\boldsymbol{\phi}_k + \alpha_l \boldsymbol{d}_k)$ must remain in the feasible region for an $\alpha_l > 0$. For clarification, k represents the iteration step. One of the disadvantages in these approaches is that we need to guess a satisfactory initial point. Another method suggests the use of a penalty function $h(\boldsymbol{\phi})$ which added to f increases in value if we move further away from the set of points which satisfy the constraints. If we are inside the feasible region, the penalty function becomes zero and the problem reduces to a search within this space. For a problem such as the one given in equation (3.5), $h(\boldsymbol{\phi})$ is most commonly defined in a quadratic form: $h(\boldsymbol{\phi}) = \frac{c}{2} g(\boldsymbol{\phi})^2$, where c is a penalty parameter [65].

A third approach and the one we are interested in throughout this project makes use of the *Lagrange multipliers* concept. Let's assume the function to be maximised or minimised is subjected to a single equality constraint. This optimisation strategy introduces an auxiliary function $\mathscr{L}$ called the *Lagrangian*, which holds both the objective function f, as well as the constraint g in a single expression:

$$\mathscr{L}(\boldsymbol{\phi}, \lambda) = f(\boldsymbol{\phi}) - \lambda g(\boldsymbol{\phi}), \tag{3.7}$$

where the parameter λ is known as a Lagrange multiplier. The basic idea in this method is to substitute the initial optimisation problem into a search for the stationary points of the $\mathscr{L}$

function within the feasible space, by using the given constraints in a similar manner to the penalty method. We therefore apply the ∇ operator to the Lagrangian function and equate the resultant components to 0 in order to find the stationary points:

$$\nabla_{\boldsymbol{\phi}} \mathscr{L} = \nabla f - \lambda \nabla g = 0, \tag{3.8}$$

$$\nabla_{\lambda} \mathscr{L} = g = 0, \tag{3.9}$$

The above set of equations allows us to search for the stationary points of the initial constrained problem. However, not every solution $\boldsymbol{\phi}^*$ may prove to be an optimum; searching for a global minimum we might end up in a local or saddle point. For this reason, in optimisation theory optimality conditions are separated in two categories: necessary and sufficient. The mathematical expressions in (3.8) and (3.9) are necessary conditions; to reveal the nature of the stationary point, one has to apply a second-derivative test based on the Hessian matrix.

2.2 Visualising the method

In order to facilitate the understanding of the Lagrange multiplier method, we shall initially make use of its geometric interpretation - see Figure 3.2.

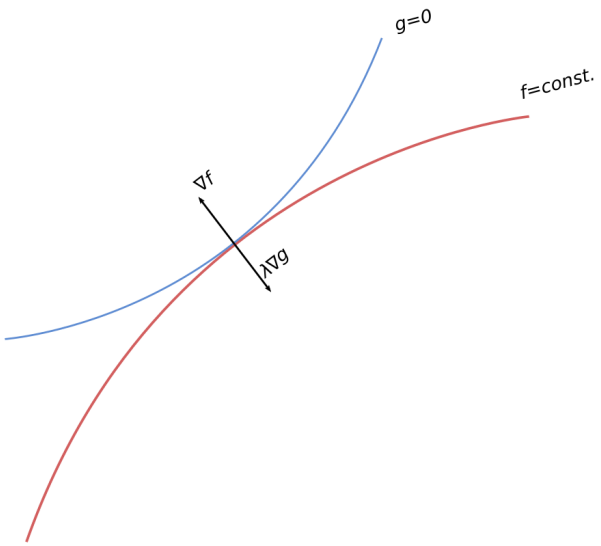

Figure 3.2: Geometrical interpretation of the condition satisfied by equation (3.10): the gradients of the two functions f and g lie on the same direction at the point where the level curves are tangent.

As we have seen earlier, the partial derivative of the Lagrangian function with respect to

the $\boldsymbol{\phi}$ set of variables reveals the following equality:

$$\nabla f = \lambda \nabla g, \tag{3.10}$$

The point satisfying the condition in equation (3.10) corresponds to the region where two level curves belonging to f and g become tangent. In other words, the solution is equivalent to the situation in which moving across the level surfaces of the function g with an infinitesimal step, the function f doesn't change. In the same point, the two gradient vectors must be collinear but not necessarily equal in length.

Additionally, we can see how the Lagrange multiplier method works in a simple example. Let's consider an optimisation problem in which we minimise the function $f(\phi_1, \phi_2) = \phi_1^2 + 2\phi_2$ subject to the following constraint $g(\phi_1, \phi_2) = \phi_1^2 + \phi_2^2 - 1$. According to the steps given in equations (3.7),(3.8) and (3.9) we arrive at the following set of solutions:

$$[\phi_1, \phi_2, \lambda]_1 = [0, 1, 1] \tag{3.11}$$

$$[\phi_1, \phi_2, \lambda]_2 = [0, -1, -1] \tag{3.12}$$

Out of the two possibilities we note that the point $A(\phi_1, \phi_2) = (0, -1)$ obtained for $\lambda = -1$ satisfies the minimum condition. Figure 3.3 illustrates the problem.

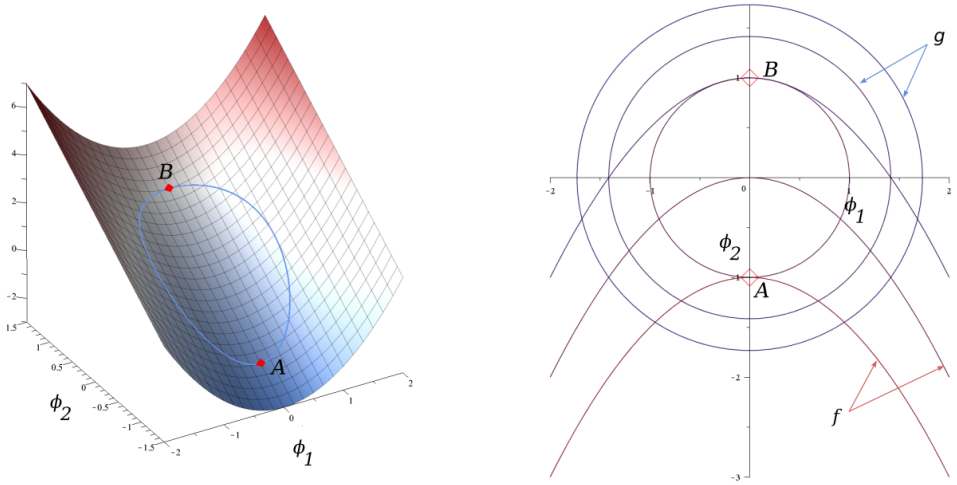

a) b)

Figure 3.3: Minimising the function $f(\phi_1, \phi_2) = \phi_1^2 + 2\phi_2$ subject to the constraint $g(\phi_1, \phi_2) = \phi^2 + \phi^2 - 1$ yields two solutions A and B, only one of which represents a minimum: $A(\phi_1, \phi_2) = (0, -1)$ for $\lambda = -1$. Subplot a) illustrates the objective and the constraint functions while subplot b) shows their respective contour plots.

As seen in subplot a), the circle of radius 1 defined by the constraint equation g is mapped onto the surface of the parabolic cylinder described by f. Subplot b) draws their respective contour lines showing that for both points satisfying the constraint requirement, the level curves are tangent. Later in this chapter we shall give details on how the Lagrange multiplier method is being used in our work. For now, we will mention that this procedure gives us the possibility to constrain the orientation of the magnetisation vector in any preferred direction for the spin structures we simulate. Unlike the two other mentioned numerical schemes, the multiplier approach readily includes the constraint g in the optimisation procedure with no additional penalty functions nor explicit treatment of g. This however comes with a cost of increased complexity; numerically we will have to allocate resources for an $N+C$ dimensional problem, where C is the number of constraints or Lagrange multipliers.

The applicability of the method is not limited to pure mathematics or physics; in the field of economics, optimisation using the Lagrange construct may be used to determine the required conditions needed to maximise the profit with reduced costs of production; inputs such as capital or labour will be subjected to constraints in this type of problem [66]. Additionally, interpreting the λ proportionality terms, may reveal information such as the marginal benefit or marginal cost; the latter parameters are relevant in the decision making process of a producer with respect to a consumer's behaviour.

3 GRADIENT DESCENT METHOD

In order to solve the minimisation problem via the Lagrange multiplier technique, we shall use a first order iterative approach known as the *steepest* or *gradient descent*. Instead of introducing the method with respect to the more complicated Lagrangian expression $\mathscr{L}$, we will initially concern ourselves with the general function f. This section will describe the reasoning behind the gradient descent approach as well as discuss a series of alternative but related iterative procedures.

Let us therefore write the Taylor series expansion of the function f around a point $\boldsymbol{\phi}$:

$$f(\boldsymbol{\phi}+\delta\boldsymbol{\phi}) \approx f(\boldsymbol{\phi}) + \sum_i \frac{\partial f}{\partial \phi_i}\delta\phi_i + \frac{1}{2!}\sum_{i,j}\frac{\partial^2 f}{\partial\phi_i\partial\phi_j}\delta\phi_i\delta\phi_j + .., \tag{3.13}$$

If the first term of the expansion may be regarded as a simple scalar, the second term is essentially the directional derivative of f while the third term expresses the components of the Hessian matrix. Depending on the given problem, different minimisation procedures may prove useful. Some of these may only include calculations of the function f without any

gradient evaluations, such as the Nelder-Mead algorithm. In this approach one constructs a mathematical object with N vertices known as a *simplex*; after f is evaluated in the multidimensional space at the points defined by the vertices, a series of transformations translate the simplex structure towards a minimum [67]. Another class of minimisation techniques makes use of the information stored in the gradient. For example, in the Fletcher-Reeves algorithm, the gradient is evaluated at every step such that a new direction - conjugate to the previous ones - is found. This procedure may prove more useful than the steepest descent approach, in situations where the landscape of the function presents long and narrow valleys [68]. If the gradient is not easily accessible, some implementations will allow iterative procedures based on approximations of ∇f; more complex algorithms can also include an approximation of the Hessian matrix which further improves the accuracy of the method. This latter class of numerical approaches is referred to as quasi-Newtonian.

First-order iterative methods are based on the Taylor series expansion in equation (3.13), truncated at the second term. The basic idea in any minimisation procedure is to move across the space of the function under study, such that the following condition is satisfied at every iteration step:

$$f(\boldsymbol{\phi}+\delta\boldsymbol{\phi}) \approx f(\boldsymbol{\phi}) + \sum_i \frac{\partial f}{\partial \phi_i}\delta\phi_i < f(\boldsymbol{\phi}) \tag{3.14}$$

The term $\sum \frac{\partial f}{\partial \phi_i}\delta\phi_i$ denotes the dot product $\nabla f \cdot \delta\boldsymbol{\phi}$. In the steepest descent approach, the displacement vector $\delta\boldsymbol{\phi}$ is chosen according to:

$$\delta\boldsymbol{\phi} = -\alpha_l \frac{\nabla f}{||\nabla f||} = -\alpha_l \boldsymbol{d}, \tag{3.15}$$

where the step length α_l must be positive. Introducing the new expression of $\delta\boldsymbol{\phi}$ in equation (3.14), we obtain:

$$f(\boldsymbol{\phi}+\delta\boldsymbol{\phi}) \approx f(\boldsymbol{\phi}) - \alpha_l \nabla f \cdot \boldsymbol{d}, \tag{3.16}$$

which satisfies the condition $f(\boldsymbol{\phi}+\delta\boldsymbol{\phi}) < f(\boldsymbol{\phi})$ since the dot product $\nabla f \cdot \boldsymbol{d}$ is always positive. Knowing that the gradient of a function gives us the direction of the greatest increase, this method makes the assumption that the optimal downhill direction lies opposite to that of the gradient. This may prove rather useful if the contour lines of a function are closer to perfect circles; for flat elongated contours, the gradient descent will have a zig-zagging behaviour slowing down calculations - see Figure 3.4. Another obvious disadvantage of the method is given by the fact that the gradient vanishes at any stationary point which yields no possible search direction. If at any given step the method reaches a saddle point, a "push" must be provided in order to continue the search for a minimum. Even if the gradient descent

approach lacks the stability of other iterative methods, it still provides a suitable framework for the present thesis as we will see later in the results sections. The MEP search in this work can be labeled as a proof of concept which is why we are not dealing with performance tests. Future studies will have to specifically aim at the optimisation of the current model.

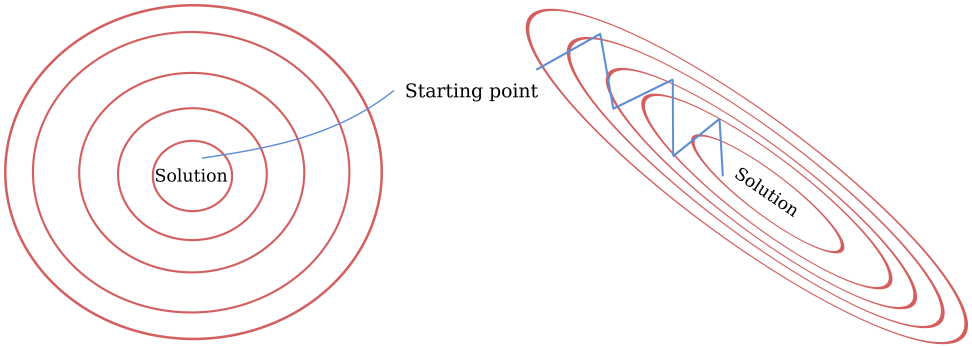

Figure 3.4: Behaviour of the gradient descent method for two different situations: a) simple function with circular level curves - the gradient descent method is straightforward; b) flat, elongated contour lines - the gradient descent algorithm is slowed-down by zig-zagging iterations.

A schematic gradient descent algorithm consists of the following steps:

1. choose a starting point $P(\boldsymbol{\phi}_k)$;
2. evaluate the gradient of the function f at the point $P(\boldsymbol{\phi}_k)$;
3. compute a search direction $\boldsymbol{d}_k = \nabla f / ||\nabla_f||$;
4. choose step size α_l;
5. construct the next point $P(\boldsymbol{\phi}_k - \alpha_l \boldsymbol{d}_k)$
6. evaluate convergence test and either go back to step 2 or end calculations

The choice of the α_l parameter in the 4^{th} step of the iteration scheme above, may represent in itself a minimisation problem in a single variable. This means that at every step k, we ideally want that value α_l which minimises the function $P(\boldsymbol{\phi}_k - \alpha_l \boldsymbol{d}_k)$. If α_l is too large, we might end up past the solution - we are overshooting. On the other hand, if α_l is too small, we might require a considerable number of iterations to reach the required solution. A series of exact or inexact numerical procedures can be used to adapt the value of the parameter α_l. Bracketing methods such as the Fibonacci Search [69] may provide a suitable range $[a \rightarrow b]$ from which α_l can be chosen. Other approaches involve guessing an approximate value for the step size based on the Armijo rule [70] or the Wolfe conditions [71]. To further simplify

the model, we shall use a fixed value for α_l which we obtained after a series of trial and error tests.

Finally, another way to approach the constraint problem in the Lagrange multiplier variant is to directly solve the system of equations (3.8) and (3.9). When dealing with linear algebraic equations this can be done using elimination or decomposition schemes such as the Gauss-Jordan method or the lower/upper (LU) triangular approach respectively. For non-linear and transcedental equations, the complexity of the problem increases such that general algorithms are difficult to define.

4 IMPLEMENTATION

The main aim of our work consists of tracing minimum energy paths of reversal, from which one can extract energy barriers between two given magnetisation states. As we have mentioned earlier, we are interested in simulating spin chain systems characterised by the Hamiltonian in equation (3.1). For each of these structures we can define a global magnetisation vector in the following manner:

$$\boldsymbol{v} = \frac{1}{N}\sum_i \boldsymbol{s}_i, \tag{3.17}$$

where N represents the total number of spins in the system.

During the writing process of a recording layer, an external magnetic field acts upon the global magnetisation of each individual bit, changing their polarisation from *up* to *down* - with respect to the EA - according to the information that needs to be stored. Assuming the polarisation of the bits takes place in continuous steps, we are seeking to replicate this process using the Lagrange multiplier method described earlier. Therefore, in our simulations we will have to force or constrain the magnetisation $\boldsymbol{v}$ such that its projection on the Oz axis changes in successive steps going from $+1$ to -1. Analogous to transition state theory, we are mapping the total energy of the system according to the variation of a given reaction coordinate. In our case this translates to evaluating: $E = f(v_z)$. In this section, we shall give a short description of the common dynamic implementation of the Lagrange multiplier method in the field of magnetics, based on the LLG equation; finally, we will outline our numeric scheme along with its optimisations and relationship to the LLG based approach.

4.1 The dynamic approach

The Lagrange multiplier method has been previously applied in the field of magnetics; Garanin and Kachkachi initially suggested the use of the constraint approach in order to describe spherical nanoparticles characterised by a second-order Néel surface anisotropy [72]. Their results show how the energy landscape modifies for different degrees of deviation from a perfect macrospin structure. A second study conducted by Paz et al. [73] shows both in an atomistic and micromagnetic fashion how energy barriers can be obtained for a series of multi-spin systems such as grains or nano-wires. In their investigation, it is accepted that the applicability of the method is limited by the choice of the constraint itself; the latter term needs to be adjusted according to the problem at hand in order to avoid highly unrealistic energy paths. In other words, the Lagrange multiplier method requires an initial guess of the possible reversal modes for a given magnetic structure.

Both of the studies mentioned earlier, implement a constraint of the following type:

$$\mathscr{G} = -N\boldsymbol{\lambda} \cdot (\boldsymbol{v} - \boldsymbol{v}_0), \tag{3.18}$$

where $\boldsymbol{\lambda}$ takes the role of the Lagrange multiplier and the biasing direction of the magnetisation is governed by $\boldsymbol{v}_0$. The expression in equation (3.18) is then added to the Hamiltonian of the system such that the Lagrangian function is formed:

$$\mathscr{L} = \mathscr{H} + \mathscr{G} = \mathscr{H} - N\boldsymbol{\lambda} \cdot (\boldsymbol{v} - \boldsymbol{v}_0) \tag{3.19}$$

The constraint term does not represent in itself a real physical quantity; for this reason $\mathscr{L}$ can be considered a quasi-fictitious magnetic energy. The dynamic approach implemented in both studies mentioned earlier [72, 73] is based on the LLG equation, which describes the motion of magnetic moments under the action of a given effective field:

$$\frac{d\boldsymbol{s}_i}{dt} = -\frac{\gamma}{1+\alpha^2}\left[\left(\boldsymbol{s}_i \times \boldsymbol{H}^i_{eff}\right) + \alpha\,\boldsymbol{s}_i \times \left(\boldsymbol{s}_i \times \boldsymbol{H}^i_{eff}\right)\right], \tag{3.20}$$

where the first term of the equation models the infinite precession of the spin vectors $\boldsymbol{s}_i$ around the direction given by $\boldsymbol{H}^i_{eff}$, while the second term introduces a dissipative mechanism which damps the precession. The parameter α - known as the damping constant - usually takes values in the range $[0 \rightarrow 1]$, where 0 corresponds to a permanent motion around the field and 1 is the critical damping above which the motion is overdamped. Historically, the initial form of the LLG equation was introduced by Landau and Lifshitz in 1935 [74]. Later, Gilbert reshaped the equation in the form known today [75]; the main difference between the

two mathematical formulations is represented by the choice of the damping term. It can be shown that the formalism developed by Landau and Lifshitz leads to a non-physical result: the motion gets increasingly fast when α increases [76]. Both equations lead to the same results for a small value of the damping constant. In Figure 3.5, one can see how does the α parameter affect the motion of a single spin.

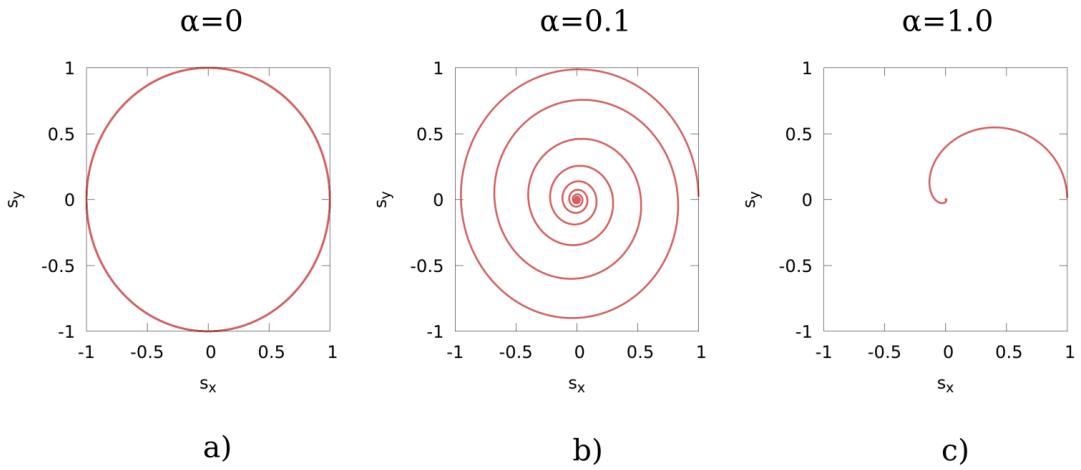

Figure 3.5: Precession of a single spin magnetic moment in the presence of an external field as described by the LLG equation. The figures are restricted to an Oxy plane, with the direction of the field chosen perpendicular to it. a) zero dissipative motion for $\alpha = 0$; b) ordinary precession for $\alpha = 0.1$ and c) motion for the critical damping $\alpha = 1$. The initial direction of the magnetic moment was chosen as <1,0,0>.

In order to implement the Lagrange multiplier method via the LLG equation, one needs to firstly convert the energy given in equation (3.19) into an effective field. This can be done by differentiating the Lagrangian function with respect to the individual spin magnetic moments:

$$\boldsymbol{H}^i_{eff} = -\frac{1}{\mu^i_s}\frac{\partial \mathscr{L}}{\partial \boldsymbol{s}_i}, \tag{3.21}$$

where $\boldsymbol{H}^i_{eff}$ is acting locally on each spin i. Following this, we also need an equation able to describe the time evolution of the $\boldsymbol{\lambda}$ vector. This can be obtained taking the partial derivative of the Lagrangian function with respect to $\boldsymbol{\lambda}$:

$$\frac{d\boldsymbol{\lambda}}{dt} = \frac{\partial \mathscr{L}}{\partial \boldsymbol{\lambda}} = -N(\boldsymbol{v} - \boldsymbol{v}_0) \tag{3.22}$$

Introducing the expression of the effective field (3.21) in the LLG equation (3.20), and coupling the latter with the time variation of the constraint vector given in (3.22), it is possible to

model the constrained dynamics of a magnetic system. Normally, an effective field produces a magnetic torque $\boldsymbol{\tau}_i = \boldsymbol{s}_i \times \boldsymbol{H}^i_{eff}$ which acts on the individual spins such that the whole magnetic structure tends to relax towards an equilibrium energy defined by the given Hamiltonian. The addition of the constraint term introduces an extra component in the effective field, which on its own gives rise to a fictitious torque in the system. The balance between the two types of "forces", leads to unphysical dynamics but real equilibrium solutions since the constraint term vanishes for $\boldsymbol{v} = \boldsymbol{v}_0$. In this approach, the numeric procedure converges when the associated torque per spin $|\boldsymbol{\tau}_i|$ is smaller than a set tolerance. The dynamic approach will be used later in the thesis as a comparison model, but we need to mention that it has been developed and optimised within our research group previously and it is not the result of this work.

4.2 Direct energy minimisation

Unlike the dynamic approach, the constrained problem defined by equation (3.19) is tackled in our thesis via a direct optimisation of the Lagrangian function. Instead of converting the energy into a field and then introducing the latter in the LLG equation, we make use of the gradient descent procedure in order to find the equilibrium magnetisation for a given set of conditions.

Given the spin Hamiltonian in (3.1) and the constraint term described by equation (3.18), the corresponding Lagrangian function in our model is written in the following manner:

$$\mathscr{L} = -\sum_i \mu^i_s \boldsymbol{s}_i \cdot \boldsymbol{H} - \sum_{\substack{i\neq j \\ i<j}} J_{ij} \boldsymbol{s}_i \cdot \boldsymbol{s}_j - \sum_i k^i_u (\boldsymbol{s}_i \cdot \boldsymbol{n})^2 - N\boldsymbol{\lambda} \cdot (\boldsymbol{v} - \boldsymbol{v}_0) \tag{3.23}$$

The search for energy minima according to the steepest descent method is based on calculating the gradient for the above mathematical expression. Identical to the dynamic approach, this is obtained taking the partial derivatives of $\mathscr{L}$ with respect to the spin and constraint variables:

$$\frac{\partial \mathscr{L}}{\partial \boldsymbol{s}_i} = -\mu^i_s \boldsymbol{H} - \sum_{ij} J_{ij} \boldsymbol{s}_j - 2k^i_u (\boldsymbol{s}_i \cdot \boldsymbol{n})\boldsymbol{n} - N\boldsymbol{\lambda} \tag{3.24}$$

$$\frac{\partial \mathscr{L}}{\partial \boldsymbol{\lambda}} = -N(\boldsymbol{v} - \boldsymbol{v}_0) \tag{3.25}$$

One possibility now is to construct the search directions based on the $3(N+1)$ dimensional

vector:

$$\nabla \mathscr{L} = \left(\frac{\partial \mathscr{L}}{\partial s_x^1}, .., \frac{\partial \mathscr{L}}{\partial s_x^N}; \frac{\partial \mathscr{L}}{\partial s_y^1}, .., \frac{\partial \mathscr{L}}{\partial s_y^N}; \frac{\partial \mathscr{L}}{\partial s_z^1}, .., \frac{\partial \mathscr{L}}{\partial s_z^N}; \frac{\partial \mathscr{L}}{\partial \lambda_x}, \frac{\partial \mathscr{L}}{\partial \lambda_y}, \frac{\partial \mathscr{L}}{\partial \lambda_z} \right) \tag{3.26}$$

This however increases the degree of complexity for the energy surface we are exploring and leads us astray from the dynamic description, which separates the update equations of the spin variables and the Lagrange multipliers. The second possibility and the one we make use of consists in splitting the above vector (3.26) in the following components:

$$\nabla_{\boldsymbol{s}} \mathscr{L} = \left(\frac{\partial \mathscr{L}}{\partial s_x^1}, .., \frac{\partial \mathscr{L}}{\partial s_x^N}; \frac{\partial \mathscr{L}}{\partial s_y^1}, .., \frac{\partial \mathscr{L}}{\partial s_y^N}; \frac{\partial \mathscr{L}}{\partial s_z^1}, .., \frac{\partial \mathscr{L}}{\partial s_z^N} \right) \tag{3.27}$$

$$\nabla_{\boldsymbol{\lambda}} \mathscr{L} = \left(\frac{\partial \mathscr{L}}{\partial \lambda_x}, \frac{\partial \mathscr{L}}{\partial \lambda_y}, \frac{\partial \mathscr{L}}{\partial \lambda_z} \right) \tag{3.28}$$

We will later be referring to the first term as the spin gradient while the later will be known as the constraint gradient. Consequently, we are now able to construct the unit vectors $\boldsymbol{d}_i = \nabla_{\boldsymbol{s}_i} \mathscr{L} / ||\nabla_{\boldsymbol{s}} \mathscr{L}||$ and $\boldsymbol{e} = \nabla_{\boldsymbol{\lambda}} \mathscr{L} / ||\nabla_{\boldsymbol{\lambda}} \mathscr{L}||$, where $\nabla_{\boldsymbol{s}_i}$ contains only the partial derivatives linked to the i^{th} spin, while $||\nabla_{\boldsymbol{s}} \mathscr{L}||$ is the modulus of the whole spin gradient (3.27). $\boldsymbol{d}_i$ and $\boldsymbol{e}$ will set the basis for the evolution equations of the spin vectors and the Lagrange multipliers:

$$\boldsymbol{s}_{k+1}^i = \boldsymbol{s}_k^i - \alpha_s \boldsymbol{d}_i \tag{3.29}$$

$$\boldsymbol{\lambda}_{k+1} = \boldsymbol{\lambda}_k + \alpha_\lambda \boldsymbol{e}, \tag{3.30}$$

where the sign difference stands in agreement with the update equations (3.20) and (3.22) used in the dynamic approach. α_s and α_λ govern the step lengths. A stopping criterion for this numeric method can be either represented by a small change in energy or gradient in between successive iterations. Later, we will show precisely how the minimisation procedure and the LLG dynamics are mathematically related. The understanding of the various results in the steepest descent problem is often facilitated by revolving the discussion around *fields* and associated torques rather than *gradients*. In fact, the spin gradient vector in equation (3.27) is equivalent to the effective field in (3.21) but for the pre-factor $-\frac{1}{\mu_s^i}$. This clarification is deemed necessary as we will interpret our findings based on similar concepts to those in the dynamic approach based on the LLG equation.

4.3 Choice of constraint

The shape of the constraint as given in equation (3.18) sets a preferential orientation for all three components of the global magnetisation vector $\boldsymbol{v}$. This contradicts the aim of

our project since we are interested in biasing only the z direction while allowing complete rotational freedom on x and y. Naturally, this aspect leads to the limited constraint below:

$$-\lambda_z(v_z - v_{0z}) \tag{3.31}$$

Its numerical implementation is unfortunately not free of technical problems. First of all, let us consider the case of a single spin in the absence of any magnetic field. In this situation, the Lagrangian function reduces to:

$$\mathscr{L} = -k_u(\boldsymbol{s}\cdot\boldsymbol{n})^2 - \lambda_z(v_z - v_{0z}) = -k_u s_z^2 - \lambda_z(s_z - s_{0z}), \tag{3.32}$$

where we made use of equation (3.17) and the assumption that $\boldsymbol{n}$ lies on Oz. The first issue arises when the spin is pointing along the direction of the EA: $s_z = \pm 1$. Since both the anisotropy and constraint field are parallel to the direction of the spin, the resultant torque $\boldsymbol{\tau} = \boldsymbol{s} \times \boldsymbol{H}_{eff}$ is zero. In this situation, the spin is stuck and consequently its position cannot be changed. This problem arises in the implementation of the LLG equation as well, and it is usually solved by allowing small deviations of the spin vector from the equilibrium axis Oz.

Secondly, if we want to replicate a reversal process, the spin must change its projection along the EA in successive steps going from $+1$ to -1, the primary driving force resulting from the constraint term. In this simple system, we can derive an analytical expression for the equilibrium value of the Lagrange multiplier λ_z, by setting $\frac{d\mathscr{L}}{ds_z} = 0$; this results in the following condition: $\lambda_z = -2k_u s_z$, which tells us that λ_z goes through zero changing its sign and in consequence modifying the spin projection s_z on the EA. However, an additional problem may arise when the numeric procedure finds the Lagrange multiplier equal to zero. To better understand this, let us rewrite function $\mathscr{L}$, this time in terms of the angle $\theta = \langle \boldsymbol{s}, \boldsymbol{n} \rangle$ and setting $\lambda_z = 0$:

$$\mathscr{L}(\theta, \lambda_z = 0) = -k_u \cos^2\theta \tag{3.33}$$

The torque in this situation is obtained by taking the derivative with respect to θ in the equation above: $\tau = \frac{d\mathscr{L}}{d\theta} = k_u \sin 2\theta$. As it can be seen from Figure 3.6, $\sin 2\theta$ vanishes for $\theta = 90°$ which again stops the motion of the spin. In correspondence, the anisotropy energy in this point is maximum since $-\cos^2\theta = 0$. Eventually, by updating λ_z it will be possible to take the spin out of this region; however, the gradient descent method has the disadvantage of being very slow next to critical points due to $\nabla\mathscr{L} \to 0$; on top of this, choosing a small step size might increase the number of iterations required to get past this impediment. In order to overcome the first of the issues discussed here, we saw fit to make use of a constraint based

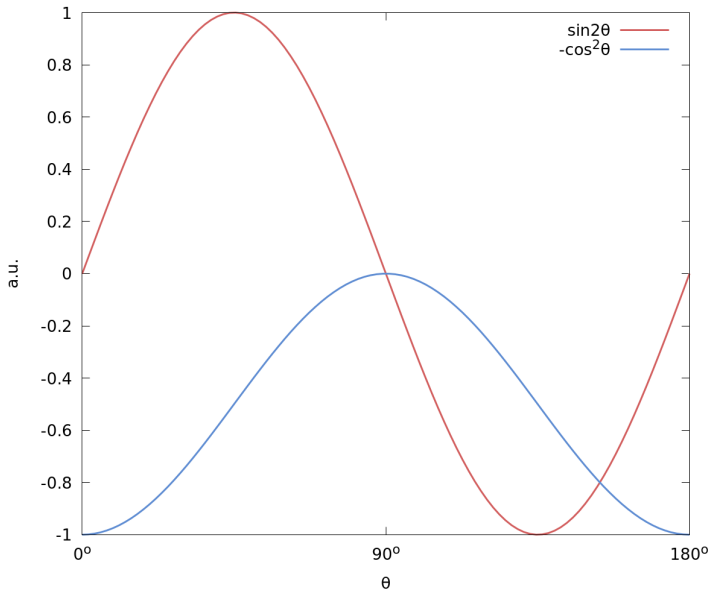

Figure 3.6: Function visualisation. Light blue: $-\cos^2\theta$; Light red: $\sin 2\theta$, where θ represents the angle between the spin vector $\boldsymbol{s}$ and the easy axis direction defined by $\boldsymbol{n}$.

on the dot product $\boldsymbol{\lambda}\cdot\boldsymbol{v}$:

$$-\boldsymbol{\lambda}\cdot\boldsymbol{v}(v_z - v_{0z}) \tag{3.34}$$

This way, we are able to bias only the z component of the global magnetisation vector v_z, while at the same time we manage to provide a torque in the x and y directions such that the spin motion does not get stuck easily. Furthermore, we observed during our tests that it is best to combine the two types of constraints given in equations (3.31) and (3.34) in order to obtain a faster and more reliable path to convergence.

$$-\boldsymbol{\lambda}\cdot\boldsymbol{v}(v_z - v_{0z}) - \lambda_1(v_z - v_{0z}) \tag{3.35}$$

For any choice of constraints, the update equations (3.29) and (3.30) can be modified to include any extra Lagrange multipliers; besides this, the idea presents a degree of generality. We think the inclusion of a constraint term based on the cross product between $\boldsymbol{\lambda}$ and $\boldsymbol{v}$ might further help increase the reliability of the method; the idea is to be able to provide a torque in the system until the condition $v_z = v_{0z}$ is satisfied, hence we want to avoid as much as possible situations in which the torque vanishes but we haven't reached a point of equilibrium yet.

The second problem addressed earlier could be tackled considering a sufficiently big step size α_s or in a more complex way by improving the converge test such that we check the

nature of the critical point we are stuck in. The gradient descent method can be adapted to work only with the simple scalar constraint of equation (3.31); however, for the most part of our thesis we make use of the combined term in (3.35) due to the previously discussed reasons. For a single-phase magnetic material, the dynamic approach has been adapted to work with a longitudinal constraint applied to all spins in the system along the z direction: $-\lambda_z(v_z - v_{0z})$; additionally, a transverse constraint of the form $-\lambda_x v_x(v_z - v_{0z})$ is applied to one of the spins at the vacuum boundary, in order to promote the deviation from the EA. In the following subsection, we shall highlight how the minimisation procedure is mathematically linked to the dynamic approach.

4.4 Mathematical equivalence of dynamic and minimisation techniques

The minimisation technique in the steepest descent approach is not entirely different to the mathematical formulation of the LLG equation. Let's assume we seek to find the equilibrium configuration of a single spin for a general set of conditions, but we are not interested in the precise dynamics that lead us towards it. In this case, if we make use of the LLG equation we can either set the damping constant α to the critical value of 1, or eliminate the precession term altogether since we are looking for the quickest path towards the final solution. The latter approach would lead to the reduced LLG expression below:

$$\frac{d\boldsymbol{s}}{dt} = -\frac{\gamma\alpha}{1+\alpha^2}\boldsymbol{s}\times\left(\boldsymbol{s}\times\boldsymbol{H}_{eff}\right) \tag{3.36}$$

Writing the effective field according to (3.21), equation (3.36) becomes:

$$\frac{d\boldsymbol{s}}{dt} = \frac{\gamma\alpha}{\mu_s(1+\alpha^2)}\boldsymbol{s}\times\left(\boldsymbol{s}\times\frac{\partial\mathscr{L}}{\partial\boldsymbol{s}}\right) \tag{3.37}$$

Furthermore, isolating the right hand-side term in the above equation and dropping the constant terms, we are left with:

$$\boldsymbol{s}\times\left(\boldsymbol{s}\times\frac{\partial\mathscr{L}}{\partial\boldsymbol{s}}\right) \tag{3.38}$$

We can now make use of the vectorial identity $\boldsymbol{a}\times(\boldsymbol{b}\times\boldsymbol{c}) = \boldsymbol{b}(\boldsymbol{a}\cdot\boldsymbol{c}) - \boldsymbol{c}(\boldsymbol{a}\cdot\boldsymbol{b})$ in order to simplify the triple cross product:

$$\boldsymbol{s}\times\left(\boldsymbol{s}\times\frac{\partial\mathscr{L}}{\partial\boldsymbol{s}}\right) = \boldsymbol{s}\left(\boldsymbol{s}\cdot\frac{\partial\mathscr{L}}{\partial\boldsymbol{s}}\right) - \frac{\partial\mathscr{L}}{\partial\boldsymbol{s}}, \tag{3.39}$$

where $\boldsymbol{s}^2$ has been dropped since it is equal to 1. If we now write the gradient vector $\frac{\partial\mathscr{L}}{\partial\boldsymbol{s}}$ as a sum of two components, one parallel and the other perpendicular to the direction of the

spin, out of the substraction in equation (3.39) we will be left with:

$$\boldsymbol{s}\left(\boldsymbol{s}\cdot\frac{\partial\mathscr{L}}{\partial\boldsymbol{s}}\right)-\frac{\partial\mathscr{L}}{\partial\boldsymbol{s}}=\nabla_{\boldsymbol{s}}^{\parallel}\mathscr{L}-\left(\nabla_{\boldsymbol{s}}^{\parallel}\mathscr{L}+\nabla_{\boldsymbol{s}}^{\perp}\mathscr{L}\right)=-\nabla_{\boldsymbol{s}}^{\perp}\mathscr{L}, \tag{3.40}$$

where $\nabla_{\boldsymbol{s}}^{\perp}\mathscr{L}$ is the spin term of the Lagrangian gradient, perpendicular to the direction given by $\boldsymbol{s}$. Therefore, we have been able to link the reduced LLG equation, to the spin component of the gradient vector in (3.26) used in the steepest descent method. We shall see in the next section why the perpendicular part of the gradient is more efficient in the search for equilibrium configurations in comparison to the whole vectorial information stored in $\nabla\mathscr{L}$.

The minimisation and the dynamic approaches are two related but still different procedures. The gradient descent method holds no time scale information and thus it offers a fictitious description of the path towards equilibrium. However, this can also be an advantage when fast convergence is the criterion on which we choose our preferred method of work. The efficiency of the LLG equation relies on the integration scheme that is being used and the required time resolution. Some of the most common implementations make use of the Heun's method or generally the class of Runge-Kutta algorithms. Optimisation techniques offer a much broader range of possibilities; a further study could implement the current energy barrier model via a faster minimisation procedure such as the conjugate gradient approach.

4.5 Algorithm scheme and optimisations

In this subsection, we shall present a simplified layout of the numerical scheme (seen in Figure 3.7) used throughout our project in order to provide a clear and helpful guide in a future work; furthermore, we will briefly describe a series of improvements we made in the algorithm such that numerical errors and inaccuracies are prevented.

First of all, we provide the possibility to separate the update procedure of the spin variables from that of the Lagrange multipliers. That is, we can allow the $\boldsymbol{s}_i$ vectors to evolve for a given set of constraints, and depending on the conditions imposed, we update the value of the λ_j parameters if required; the term λ_j denotes generally any element from the set $(\lambda_x, \lambda_y, \lambda_z, \lambda_1)$. In this manner, it is possible to ensure that we exhaust the whole minimisation potential of the constraints and the spin vectors cannot further evolve with the corresponding torques before $\lambda_j^{l_c} \to \lambda_j^{l_c+1}$; l_c is a counter which keeps track of the number of times the constraints have been modified and it is always smaller than a maximum N_λ threshold. This technique however increases the total run-time of the simulations and it remains to be fully tested. If the Lagrange multipliers are updated simultaneously with the spin vectors, the procedure

is equivalent to the constrained LLG method. The first of the conditions mentioned earlier, checks the maximum value $||\frac{1}{\mu_s^i}\boldsymbol{s}_i \times \frac{\partial \mathscr{L}}{\partial \boldsymbol{s}_i}||$ in the system; if this parameter decreases towards 0, we are ensured to be in the region of a critical point and we are only left to check if the magnetisation constraint $v_0 = v_{0z}$ is satisfied. If the fictitious torque $||\frac{1}{\mu_s^i}\boldsymbol{s}_i \times \frac{\partial \mathscr{L}}{\partial \boldsymbol{s}_i}||$ remains larger than the imposed tolerance (tol) after the maximum number of spin updates N_S has been reached, we proceed towards modifying the Lagrange multipliers.

Secondly, the update equations (3.29) and (3.30) need to be adjusted from two points of view: the numerical procedure doesn't preserve the unit length of the spin vectors, therefore after every update $\boldsymbol{s}_i^k \rightarrow \boldsymbol{s}_i^{k+1}$ we need to normalise each $\boldsymbol{s}$ vector to its magnitude $||\boldsymbol{s}||$; furthermore, any search direction $\boldsymbol{d}_i$ or $\boldsymbol{e}$ is obtained by dividing the components of the gradients in (3.27) and (3.28) by their respective magnitudes. If the length of the gradients $\rightarrow 0$, the unit vectors $\boldsymbol{d}_i$ and $\boldsymbol{e}$ will approach $+\infty$, thus introducing errors in the calculations. For this reason, $||\nabla_{\boldsymbol{s}}\mathscr{L}||$ and $||\nabla_{\boldsymbol{\lambda}}\mathscr{L}||$ are set to 1 if they drop lower than 0.1.

Thirdly, in the previous subsection we showed in what conditions the energy minimisation based on the steepest descent algorithm is equivalent to the LLG equation. In our model, we will substract from the gradient vector in (3.27) its projection on the direction of the spins, which will give us a specific advantage. This way, we make sure to focus on rotating the $\boldsymbol{s}$ vector towards equilibrium due to the perpendicular component of the gradient $\nabla_{\boldsymbol{s}}^{\perp}\mathscr{L}$, without adjusting the length of the spin since $\nabla_{\boldsymbol{s}}^{\parallel}\mathscr{L}$ is extracted. Particularly, this modification is aimed at improving the speed of the calculations.

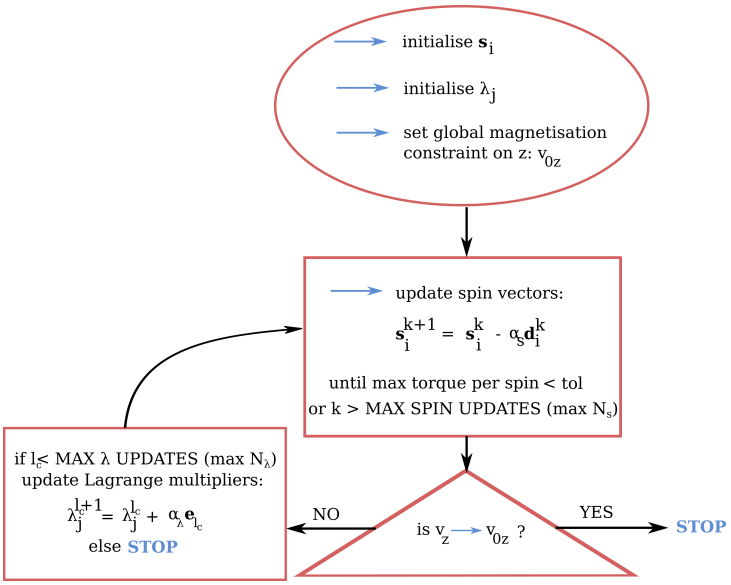

Figure 3.7: Schematic diagram of the numerical procedure implemented throughout the project.

Finally, as pointed out by Garanin and Kachkachi in [72], it is advisable to limit the values of the constraints in order to preserve the stability of the magnetic structure. Very large values of the λ_j parameters lead to high constraint fields which have the potential to irreversibly distort the system. If any λ_j increases in absolute value by a tenfold margin, we reset it to its starting point.

As seen in Figure 3.7, every simulation starts with the initialisation of the spin vectors

$\boldsymbol{s}_i$ and the Lagrange multipliers λ_j, as well as by defining the global magnetisation target v_{0z} on the direction of the EA. Next, we update the spin components based on the steepest descent algorithm and check if the tolerance is satisfied or the maximum number of updates has been reached. If any of the aforementioned conditions is violated, we proceed to modify the parameters λ_j after which we go back to the previous step. We repeat this until the condition $v_z = v_{0z}$ is satisfied and the maximum torque in the system is sufficiently small. In the worst-case scenario, the maximum number of λ_j updates will be reached without satisfying the magnetisation constraint, in which case the numerical procedure needs to be reinitialised. Below, we outline the standard simulation parameters we use:

Simulation parameter	Value
max N_s	1
max N_λ	10^7
tol	10^{-5}
α_s	0.01
α_λ	0.01
$v_z - v_{0z}$	10^{-5}
$(\lambda_x;\lambda_y;\lambda_z;\lambda_1)_{init}$	(0.01;0;0.1;0.1)

Table 2: Highlight of the standard parameters used in our simulations. If max N_s is set to 1, the update procedure of the spins and the Lagrange multipliers takes place simultaneously, replicating the approach in the dynamic method. Usually, this can help speed up the calculations.

Monolayer results

In this chapter, we will present a series of results obtained for a single-phase, hard magnetic structure, with the aim of testing and validating our numerical procedure. Initially, we shall discuss the parameters we employ in our simulations, after which we will focus our attention on the two reversal mechanisms exhibited in the elongated grains we are studying - coherent rotation and domain wall motion. Next, a brief discussion will attempt at clarifying the nature of the domain walls found in the spin chain systems under study, with the aim of explaining a series of analytic expressions we choose to test our model against. Finally, we shall consider how does the energy barrier correlate with the height of the grain and the preferred reversal mechanism, as well as replicate the SW predicted variation of the energy barrier with respect to an external magnetic field. In addition to testing our method in regards to analytic results, we shall also verify it against the picture offered by the dynamic approach based on the LLG equation.

1 Material parameters

The primary investigation in our project consists of mapping MEPs for spin chain structures. Initially, we shall consider the example of a single-phase magnetic material of hard composition with the aim of testing and validating the numerical model we developed. Our chosen atomic system in this chapter is characterised by generic parameters, within the limits defined by the current industrial demands. While traditional perpendicular recording is based on Co alloys, the evergrowing need for miniaturisation and the advent of heat-assisted technology, require the use of highly anisotropic materials, of which $L1_0$FePt is considered to be one of the most suitable candidates. If Co based grains such as CoCrPt are normally characterised by $K \approx 10^6\ J/m^3$, the $L1_0$ phase of FePt presents an anisotropy with a tenfold increase in its strength $K \approx 10^7\ J/m^3$ [77, 78]. In our model, we will use an intermediate value of $K = 7.7 \times 10^6\ J/m^3$.

The saturation magnetisation of a material is usually regarded with a higher degree of flexibility. For example, Weller et al. presented a list of media candidates with M_s ranging from 300 to 1400 kA/m [77]. Previously, in the longitudinal recording era, a high M_s was required in order to improve the magnetic signal such that it could be detected by the read heads [79]. Later, this parameter had to be carefully tailored such that the demagnetisation field $\boldsymbol{H}_d$ associated with neighbouring grains would not lead to spontaneous switching of the bits. $\boldsymbol{H}_d$ is directly proportional to M_s and generally increases as the distance between magnetic poles is reduced. The shift towards perpendicular recording and the improvement of read sensitivity bypassed both of these issues. Recently, it has been revealed that the saturation magnetisation may play a more significant role; Evans et al., extended the traditional magnetic trilemma by considering the bit-error-rate (BER), a parameter which describes the probability of an unsuccessful write event [80]. In their work, it is shown that BER is minimised and the AD optimised using materials characterised by large M_s values. In our single-phase model, we will choose a saturation magnetisation of $M_s = 1024\ kA/m$.

Finally, the last important ingredient is defined by the strength of the exchange interaction. As we have seen in the previous chapter, J_{ij} is inherently correlated to the Curie point of a material. A low T_c is preferred in the HAMR technology due to power consumption reasons and damage prevention of the head/medium interface [81]. The reduction of the ordering temperature simultaneously lowers the exchange constant; ultimately, this allows for a smoother transition between bits, thus improving the SNR [82]. For our toy material, we will consider a Curie temperature of 700 K. The lattice constant will be set to a value of $a = 3$ Å.

The equivalent atomistic parameters used for the entirety of this chapter are listed in the table below:

Parameter	Value	Unit
J_{ij}	6.87×10^{-21}	Joules
k_u	2.07×10^{-22}	Joules
μ_s	2.98	μ_B
a	3	Å

Table 3: Atomistic parameters corresponding to the hard material we are modelling throughout this chapter.

The strength of the anisotropy field for the material we are modelling evaluates to approximately 15 T. Considering a cuboidal 3 nm grain, we can clearly see that the stability

parameter KV/k_BT is close to 50 at $T = 300K$, a value well situated within the limits defined by standard recording demands.

2 MINIMUM ENERGY PATHS

In this section, we will discuss the two possible reversal mechanisms in our single-phase spin chain systems, as well as interpret their corresponding energy curves in comparison to the SW description. MEPs will be traced out by modifying the global magnetisation constraint v_{0z}, successively from +1 to −1 in steps of 0.01; for each of these points, the minimum energy is computed using the gradient descent method along with the Lagrange multiplier in the form given in equation (3.35). This procedure will give us the curve described by $E = f(v_z)$, where E is the total energy, equivalent to the Hamiltonian: $\mathscr{H}_{total}$.

The generation of the magnetic system follows the steps discussed in the previous chapter; the spin vectors are initialised along the direction of the EA such that the global magnetisation starts from $v_z = +1$. To facilitate the understanding of these results, we will initially drop the Zeeman term and consider only the effect of the magnetocrystalline anisotropy and the exchange interaction. Later, we will also introduce an applied field in the system in order to further test our numerical model.

2.1 The coherent rotation regime

Let us take the example of a magnetic grain of 3 nm in height placed in zero applied field. In Figure 4.1, we can see two subplots which picture the reversal process of the grain. As the v_z component is reduced, the spins will deviate from the equilibrium position via a coherent mechanism; this will correspond to an increase in energy which will reach a maximum for $v_z = 0.0$ as subplot a) suggests. Further lowering the magnetisation constraint, the spin system will end up in the $-z$ direction, opposite to its initial orientation - see subplot b). Since there is no applied field, the two competing energies in this system are given by the anisotropy and the exchange terms; as the size of the grain is small enough, the prevaling spin-spin interaction favours a macrospin-like behaviour.

Subfigure a) shows both the numeric energy curve we obtained as well as the analytic reference based on the SW model. Traditionally, the SW picture does not contain any exchange term; to compare it with our method, we need to substract from the total energy E the spin-spin contribution : $-\frac{1}{2}J(N-1)$, where the i, j indices accompanying the exchange constant have been dropped for simplicity. This procedure does not alter the corresponding

energy barrier, since the latter is based on calculating energy differences $\Delta E = E_1 - E_2$. Any constant value added or subtracted in both of the initial E_1 and final E_2 energy terms, will be irrelevant in the calculation of ΔE. The energy depicted in the top subplot of Figure 4.1

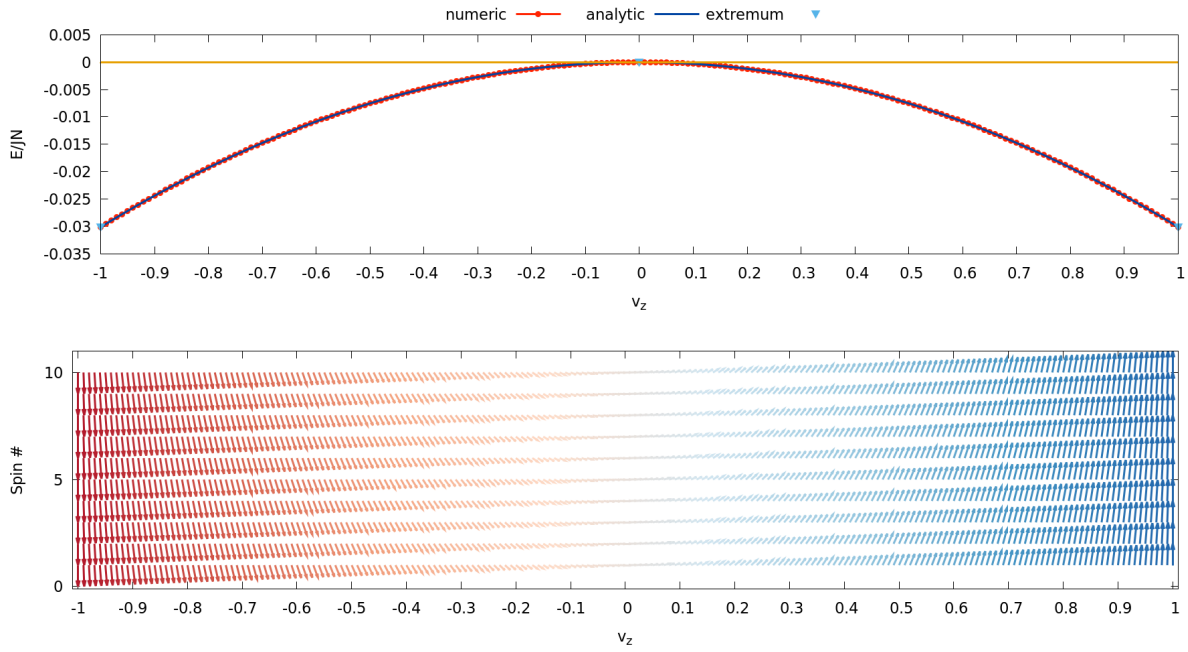

Figure 4.1: Coherent reversal of a 3 nm magnetic grain. Upper figure - total energy E as a function of the global magnetisation v_z. Dotted red line: numerical result based on the gradient descent method; continuous blue line: analytic result based on the SW theory. The light-blue triangles suggest the extremum energy points, the 0 margin being the maximum value. The y-axis is normalised to the exchange constant J and the number of spins in the system N. Lower figure - rotation of the spins in the Oxz plane. The colour represents the magnitude of the s_z projection on the EA, with red being -1, white 0 and blue +1. The y-axis denotes the spin id; a height of 3 nm corresponds to a chain of 10 spins.

refers to the average value per spin; since all magnetic moments rotate in phase, they are characterised by the same energy. Taking the maximum point and either given minima, we can calculate an average energy barrier which in this case is equivalent to the value associated with the reversal of a single SW particle.

2.2 Domain wall nucleation in the reversal process

Following the example in the previous subsection, we will now increase the size of the magnetic grain by doubling its height: $h = 6$ nm. The reversal process and the energy associated are depicted in Figure 4.2. Starting from $v_z = +1$ and slowly reducing the magnetisation

constraint, we observe an initial coherent behaviour similar to the previous case. However, as v_z approaches a value of 0.7, a domain wall is nucleated in the system; following this, the wall will propagate through the grain, leaving behind completely reversed magnetic moments until the entire spin chain relaxes in the $-z$ direction.

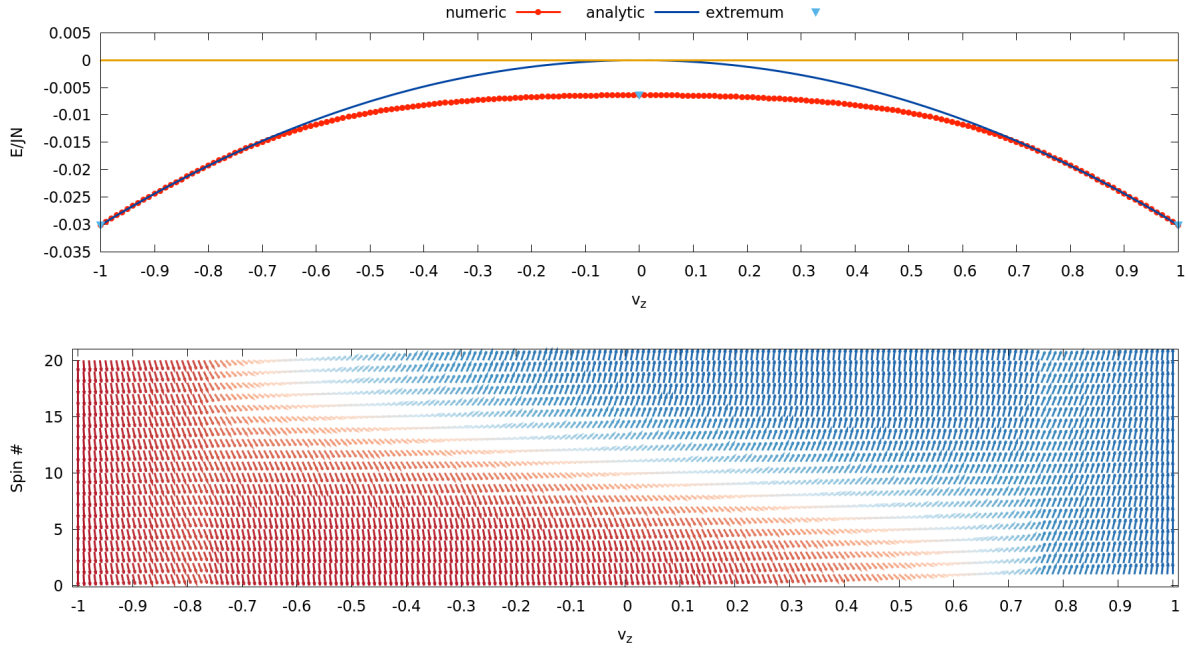

Figure 4.2: Example of domain wall nucleation in the reversal process of a 6 nm long magnetic grain. Upper figure - total energy E as a function of the global magnetisation v_z. Dotted red line: numerical result based on the gradient descent method; continuous blue line: analytic description of the coherent reversal in the SW model. The average energy per spin in this case presents a lower maximum compared to the coherent path. All the other characteristics mentioned in the previous figure are valid here as well.

The reason why domain wall nucleation prevails over the macrospin approximation, can be understood in numerous ways. We recall from Chapter 2, that in general a magnetic system will energetically prefer a multi-domain structure in an attempt to close the field lines in itself and reduce the overall magnetostatic energy. Since we do not consider any dipole-dipole interactions, a more specific explanation needs to be given: in the absence of an external field, the energy of a magnetic grain in the coherent limit, is given by the KV product as suggested in equation (2.37). On the other hand, taking a look at the mathematical expression in (2.33), the wall energy is directly proportional to the cross-sectional area of the grain. If the latter parameter remains unchanged when we raise the height h, the volume increases - thus steadily requiring more energy to undergo a coherent process. At a critical

point, a nucleation process will take place, thus reducing the total energy of the grain. Later in this chapter, we will correlate the width of a domain wall with the transition point between the two reversal mechanisms. A similar analysis for elongated grains, has been previously approached micromagnetically by Dittrich/Forster et al. [15, 16] via the NEB method.

We need to mention that our numeric procedure leads to domain wall nucleation provided we make use of a specific adjustment. After a new magnetisation constraint v_{0z} is set, we rotate the first spin in the chain around the y axis using the following matrix product:

$$\begin{pmatrix} s_{1x} \\ s_{1y} \\ s_{1z} \end{pmatrix}^{*} = \begin{pmatrix} \cos\theta & 0 & \sin\theta \\ 0 & 1 & 0 \\ -\sin\theta & 0 & \cos\theta \end{pmatrix} \begin{pmatrix} s_{1x} \\ s_{1y} \\ s_{1z} \end{pmatrix} \tag{4.1}$$

where θ is set to 5°. In the absence of this step, the magnetic system will always follow a coherent behaviour - owing to the difficulty of the gradient descent method in exiting a stationary point. This initial spin rotation plays a similar role to the transverse constraint used in the dynamic approach.

3 DOMAIN-WALLS IN ELONGATED GRAINS

This section aims at detailing the nature of the domain-walls observed in the spin chain systems we study. If one takes a closer look at the wall profile in the lower subplot of Figure 4.2, it becomes clear that it does not coincide with the expected Bloch or Néel arrangements in Figure 2.10. In the Bloch model, the rotations of the spins take place in a plane perpendicular to the wall, while in the Néel description spins rotate parallel to it. From this point of view, our grain structure reverses in a Néel like rotation. The matching is not entirely perfect since the geometry is different. In our case, Oz gives the direction of the EA and Oxy represents the median plane, separating the two domains on either side of the wall. In subplot b) of Figure 2.10, Oz remains the direction of the EA, but Oxz is the median plane. However, if we turn back to the analytic description of the Bloch wall energy in Chapter 2, the only factors of interest are the anisotropy and the exchange contributions. In the absence of any demagnetising term, we can treat our observed domain walls using the Bloch model. This clarification is important, since later in the chapter we will make use of the analytic expression for the wall energy, in order to test the validity of our numeric results.

In order to verify our claims, we can initially check the magnetisation profile in the remanent state corresponding to $H = 0$. According to the Bloch model, the spins will rotate

within the system, such that their s_z projection on the EA, follows a hyperbolic tangent variation - see equation (2.36). This result represents the exact analytic solution obtained using methods of variational calculus. In the approximate model we also discussed in Chapter 2, the spins were assumed to exhibit a rotation with a constant angle $\frac{\pi}{N^*}$, where N^* is described by equation (2.30) and represents the equilibrium number of spins in the wall. For our material parameters detailed in Table 3, N^* evaluates to approximately 18 spins, equivalent to 5.4 nm. In this simplified model, the spin profile can be obtained considering that θ - the angle given by the dot product $\boldsymbol{s} \cdot \boldsymbol{n}$ - is varying from 0 to π in steps of $\frac{\pi}{N^*}$, and the projection s_z is given by $s_z = \cos\theta$.

In Figure 4.3a), we considered the example of a 12 nm grain, for which we compared the remanent magnetisation profile obtained using our numerical procedure, with the exact and approximate models mentioned earlier.

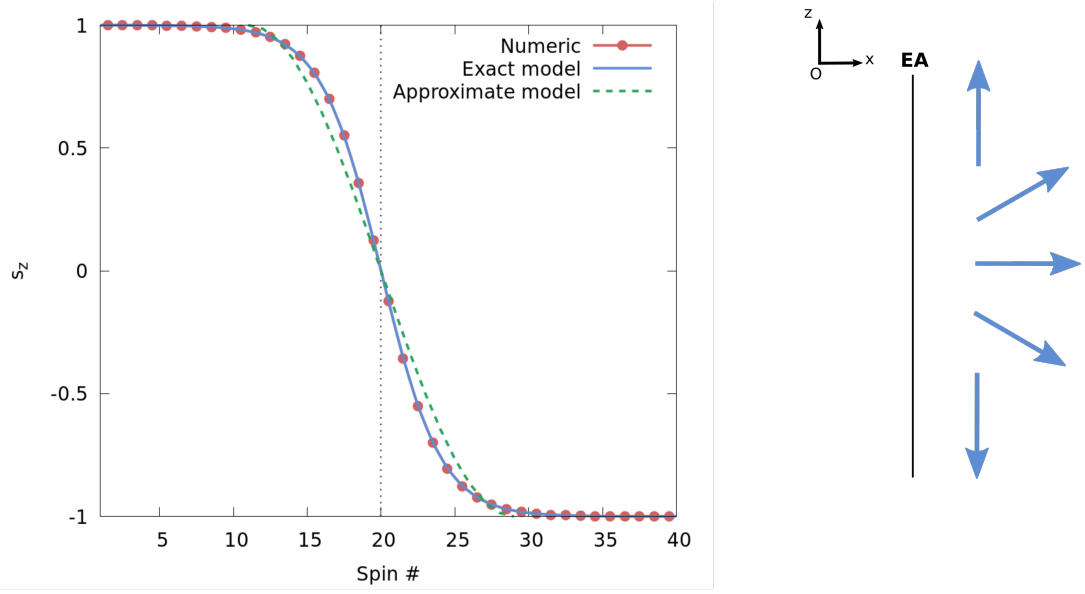

Figure 4.3: a) Magnetisation profile in the remanent state for a grain of 12 nm - equivalent to a chain of 40 spins: Dotted red lines - numerical result; continuous blue line - exact profile obtained based on equation 2.36; dashed green line - approximate profile based on the assumption that spins rotate uniformly within the wall with an angle $\frac{\pi}{N^*}$. The x-axis gives the id of the spin with the index starting from 0.5; b) Schematic representation of the spin rotations in an elongated grain; EA represents the easy-axis.

We first of all see that our method fully matches the description given by the variational approach; second of all, the approximate profile gives a reasonable account of the s_z evolution

particularly at the edges of the wall. Additionally, in subplot b) one can see a schematic representation of the in-plane spin rotations arising in the domain walls found in our elongated grains.

The uniform rotation of the spins in the approximate model can easily be shown not to correspond with the actual picture within the domain wall. Two neighbouring spin vectors $\boldsymbol{s}_{i+1}$ and $\boldsymbol{s}_i$, will form an angle between them, given by the difference $\theta_{i+1} - \theta_i$. Plotting the latter quantity for all the spin pairs in the chain, the Gaussian profile in Figure 4.4 is obtained, thus invalidating the hypothesis of the approximate model.

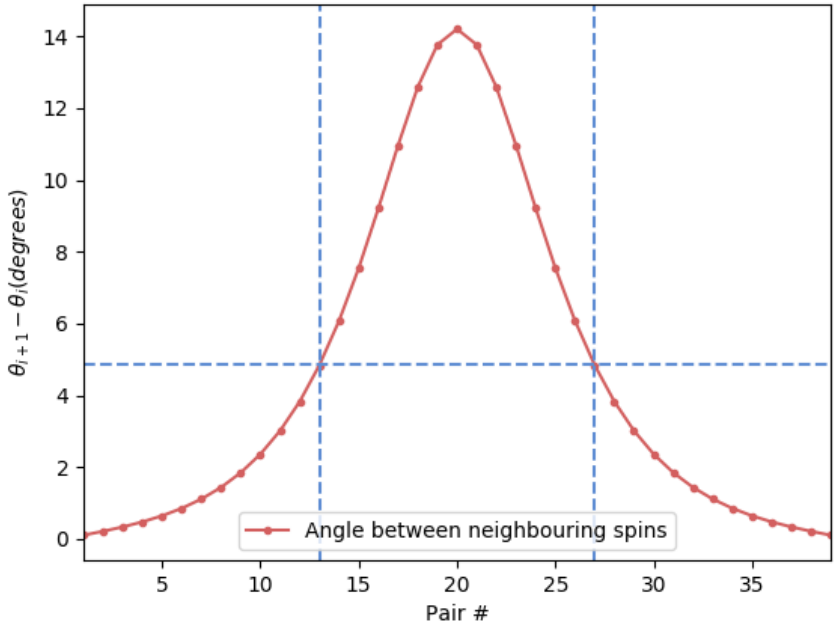

Figure 4.4: Angle between neighbouring spins across the total length of the spin chain. The intersections of the blue dotted lines, mark the start and end points on the red curve, corresponding to the spin pairs in the domain wall.

4 ENERGY BARRIERS

In this section, we will focus our attention on the energy barriers involved in the reversal process of the spin chains we study. First of all, we will seek to better understand the transition from coherent behaviour to domain wall nucleation by controlling the height of the magnetic grain. In order to test the validity of our model, we shall compare our results with the SW theory and the description offered by the dynamic approach based on the LLG equation.

Finally, we will explore the potential of energy barrier reduction by use of an applied magnetic field.

4.1 Reversal mechanism control via grain height variation

Let us consider a broad range of grain heights: h =[1:15] nm; the maximum limit may exceed the requirements found in certain literature sources but nonetheless it does not affect the interpretation of the results. For example, Weller et al. [83] suggest that in HAMR applications, the media thickness needed to reach an areal density of 4 Tb/in^2 should be fixed around 8 nm; studies concerning hard/soft composites can extend this limit to 10 nm and beyond.

Having clarified this, we will trace MEPs for each grain size and extract the corresponding energy barrier, that is the difference between the maximum and the equilibrium energy - the latter being obtained for either points $v_z = \pm 1$.

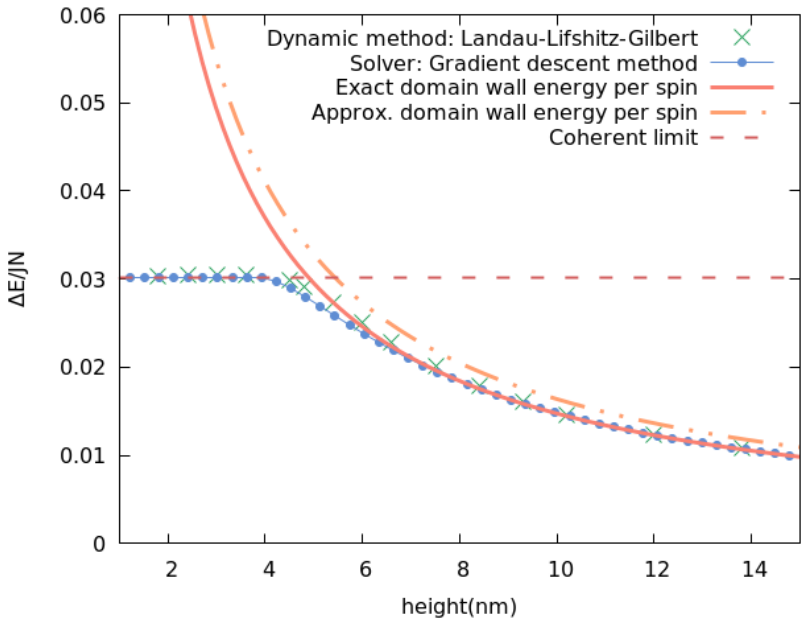

Figure 4.5: Energy barrier as a function of grain height: dashed line – single domain energy barrier according to SW theory; dotted line & starred points - numerical energy barrier obtained with the gradient descent and LLG method respectively; solid line – exact analytic domain wall energy based on equation (2.34); dots and dashes - approximate domain wall energy as given in equation (2.31). All values on the y axis have been normalised to the exchange constant J and the number of spins N. In reference [73], Paz et al. interpret the $\Delta E = f(h)$ variation, without the normalising factor $\frac{1}{N}$.

We compare our numerical result and test its validity against the description offered by the dynamic procedure and three analytic equations. One of these, represents the SW energy

barrier - obtained from the path defined by equation (2.41) - while the other two expressions concern the Bloch wall energy as given in the approximate and exact equations in (2.31) and (2.34) respectively. The result is plotted in Figure 4.5; we mention that ΔE is normalised to the exchange constant J and the total number of spins N in the system.

As we can see, for relatively small grain heights in the range $[1 \rightarrow 4]$ nm, the numerical energy barrier per spin is equal to the single-domain value obtained using the SW model. When the size of the system increases further, $\Delta E/JN$ is lowered and the numerical curve converges towards the exact analytic expression of the normalised domain-wall energy - the curve corresponding to the simplified Bloch model is given for comparison. This means that, in order to reverse the magnetisation of highly elongated grains, we need to provide the amount of energy able to nucleate a domain wall in the system. Reversal of small grains however, demands an energy input able to rotate the spins over the barrier defined by the strength of the anisotropy term. Given the results displayed in Figure 4.5, we can conclude that there is a good agreement between the two numerical methods used and the analytic tests we employed.

The transition from the coherent behaviour to domain wall nucleation can be understood from a different point of view. In literature, a Bloch wall width is defined according to the following equation [36]:

$$\delta_B^* = \pi \sqrt{\frac{A}{K}} \tag{4.2}$$

The expression above is written using micromagnetic parameters, but from an atomistic point of view, we have:

$$\delta_B = \pi a \sqrt{\frac{J}{2k_u}}, \tag{4.3}$$

where we made use of the conversion factors in Table 1. Given the material parameters mentioned at the beginning of this chapter, δ_B evaluates to approximately 4 nm for our toy magnetic system. Thus, it becomes obvious that our elongated grain will energetically prefer a multi-domain structure once it is sufficiently large to fit a domain wall across its volume.

In Figure 4.6, one can take a closer look at individual MEPs obtained for different height values, using both the minimisation technique and the dynamic approach. In the same plot, we also include the curve corresponding to the coherent reversal mode. It is once again easy to see that, as the size of the grain increases, the average energy in the system will lower its peak. The asymmetry in the MEPs given by the dynamic method, comes as a result of not relaxing the spin system to complete equilibrium; besides this aspect, there is a very good degree of agreement between the two approaches. While not shown in greater detail, it is

worth mentioning that the gradient descent method traces the optimum paths in tens of seconds, while the LLG method presents a tenfold increase in the run-time.

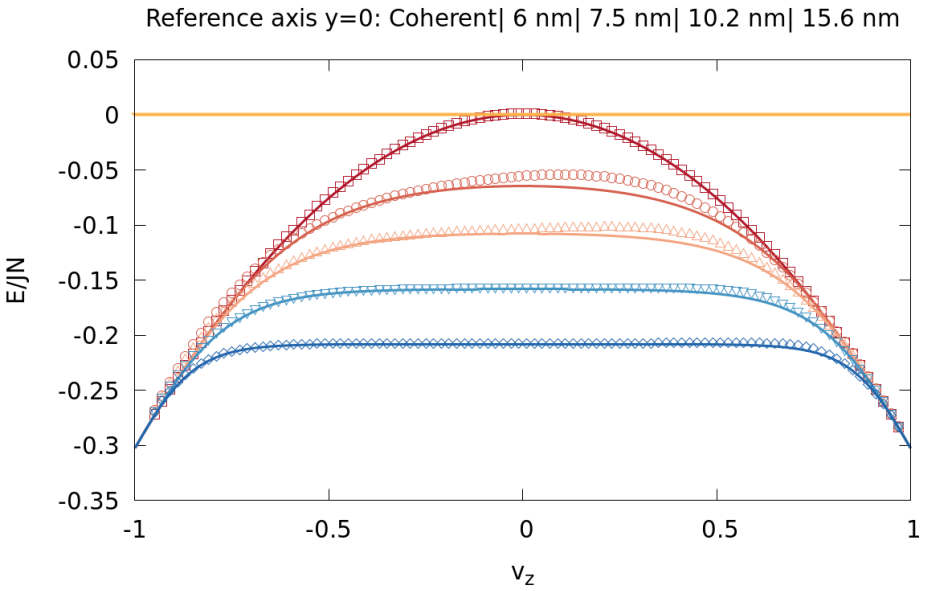

Figure 4.6: Minimum energy paths for different grain heights. The maximum energy peak corresponds to the coherent reversal curve. Continuous lines: results obtained using the minimisation procedure; empty symbols: results obtained integrating the LLG equation. The slight asymmetry in the MEPs corresponding to the dynamic approach, is a consequence of not relaxing the spin system until complete equilibrium is reached.

4.2 Energy barrier reduction in an external magnetic field

An important conclusion from the SW theory can be drawn referring back to the energy barrier equation in (2.40). In its atomistic form, we rewrite it as:

$$\Delta E = k_u \left(1 - \frac{H}{H_k}\right)^2, \tag{4.4}$$

where H_k is equal to $2k_u/\mu_s$ and represents the anisotropy field. We need to emphasise that here we refer only to the case in which the external field is applied parallel to the EA.

We can easily identify the two extremum values of ΔE, in regards to the strength of the applied field H. When the latter term is zero, the total energy of the SW particle consists of the anisotropy term only; in this case, the height of the energy barrier is defined by the k_u constant as seen in equation (4.4). As the field H is increased, ΔE lowers in a quadratic manner until it completely vanishes when the condition $H = H_k$ is satisfied. In simple terms,

it means that once the anisotropy field is reached, the reversal of the particle from one magnetisation state to another is made possible. In real applications, the magnetic grains forming individual bits may not reverse in the same applied field due to a distribution of their internal switching fields. This is the result of several factors regarding the morphology of the grains, their magnetic properties or degree of alignment with the applied field, which in turn affect the local energy barriers and overall lead to a deterioration of the SNR [77, 84]. In more detail, grains with switching field lower than the average will be more unstable when subjected to thermal effects, thus leading to irreversible information loss. On the contrary, a switching field higher than the average, leads to errors during the writing process if the strength of the applied field is not large enough to reverse all the individual grains. The exchange interaction may also play a role in the observed SNR, since a strong coupling between neighbouring grains, prevents smooth transitions from one bit to another. However, the use of highly anisotropic materials in the current perpendicular magnetic recording (PMR) technology limits thermal instabilities and exchange induced errors.

In this subsection, we will firstly aim to replicate the $\Delta E = f(H)$ variation in the coherent limit described by the SW theory; additionally, we will investigate the field dependent energy barrier also in systems exhibiting a non-coherent reversal mechanism. In Figure 4.7, one can see the results we obtained for the following grain heights: 3 nm, 6 nm and 12 nm. With the smallest size system being below the Bloch wall width (≈ 4 nm), the numerical calculations perfectly overlap over the analytic description of the SW model; the quadratic variation of the $\Delta E = f(H)$ function is obtained, and the $H = H_k$ equality leads to a vanishing of the energy barrier. We recall that given the material parameters described earlier in this chapter, the anisotropy field H_k takes a value around 15 T. Both the 6 nm and 12 nm grain dimensions exhibit a domain wall based switching; as we already know from the previous subsection, the zero field energy barrier in systems larger than the Bloch wall width differs from the coherent case and it is governed by the wall energy (here in normalised units). An interesting result is obtained as the strength of the applied field is increased. Our numerical simulations yield the same 15 T coercivity for the grains reversing by domain wall nucleation. It is important to note that the expression given in (4.4) is valid only in the coherent limit. The energy barrier variation with respect to the field strength could be modelled using a general analytic equation such as:

$$\Delta E = \Delta E_0 \left(1 - \left(\frac{H}{H_{cr}}\right)^{\alpha}\right)^{\beta}, \tag{4.5}$$

where ΔE_0 is the zero field energy barrier and α and β are fitting parameters. In our case, the irreversible switching takes place at a critical field H_{cr} equal to the anisotropy field H_k. It is

expected that H_{cr} along with the α and β parameters will vary as the field deviates from the direction of the EA.

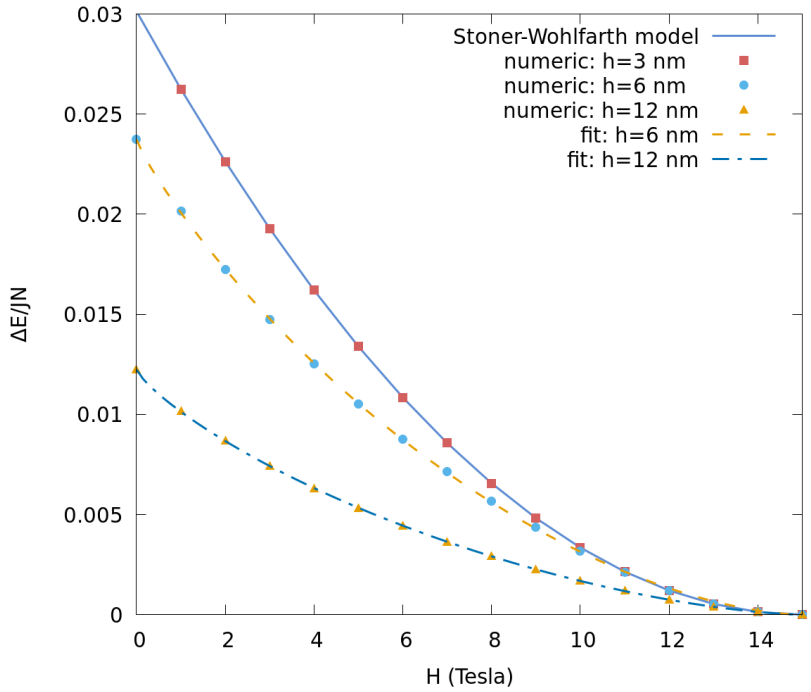

Figure 4.7: Energy barrier as a function of the applied field strength for a 3 nm, 6 nm and 12 nm grain height. Interestingly, our numerical simulations yield the same coercivity in all three cases: 15 T, a value equal to the anisotropy field. The fitting of the 6 nm and 12 nm results has been achieved using equation (4.5), where the critical field H_{cr} is equal to H_k and the zero field energy barrier ΔE_0 is the normalised wall energy.

The unchanged coercivity value obtained irrespective of the grain height, can be understood by taking a closer look at the optimum paths of reversal. To develop our argument, we shall discuss the effect of the Zeeman component on the overall shape of the energy landscape. In Figure 4.8.a) we plot the zero field MEPs of the 3 nm (coherent), 6 nm and 12 nm grains respectively. In this case, all systems are characterised by two energy minima at $v_z = \pm 1$ and one maximum point at $v_z = 0$. An external field applied in the -z direction has two effects on the energy surfaces.

First of all, the points defining the MEPs are shifted along the y-axis depending on the relative orientation between spins and the external field - see the $H = 5$ T case in subplot b) of Figure 4.8. To quantify this effect, we use the following geometrical construct: a straight line is drawn through the first two right hand side points on each individual MEP as displayed below; the procedure is repeated for field strengths ranging from 0 T to 16 T. For each case, the slope (m) of the straight line is extracted and the results are plotted in Figure 4.8.c). We can see

that for all system sizes, the magnitude of the slope increases identically as H is modified. At exactly the same critical field limit of 15 T, m becomes 0 and a further increase of the applied field strength changes its sign. This discontinuity corresponds to an irreversible change of the energy landscape for which the initial minimum at $v_z = +1$ becomes a maximum energy point. In normalised units, the energy shift due to the Zeeman component is identical for all the grain heights we considered, thus giving an initial explanation for the equal coercivity values.

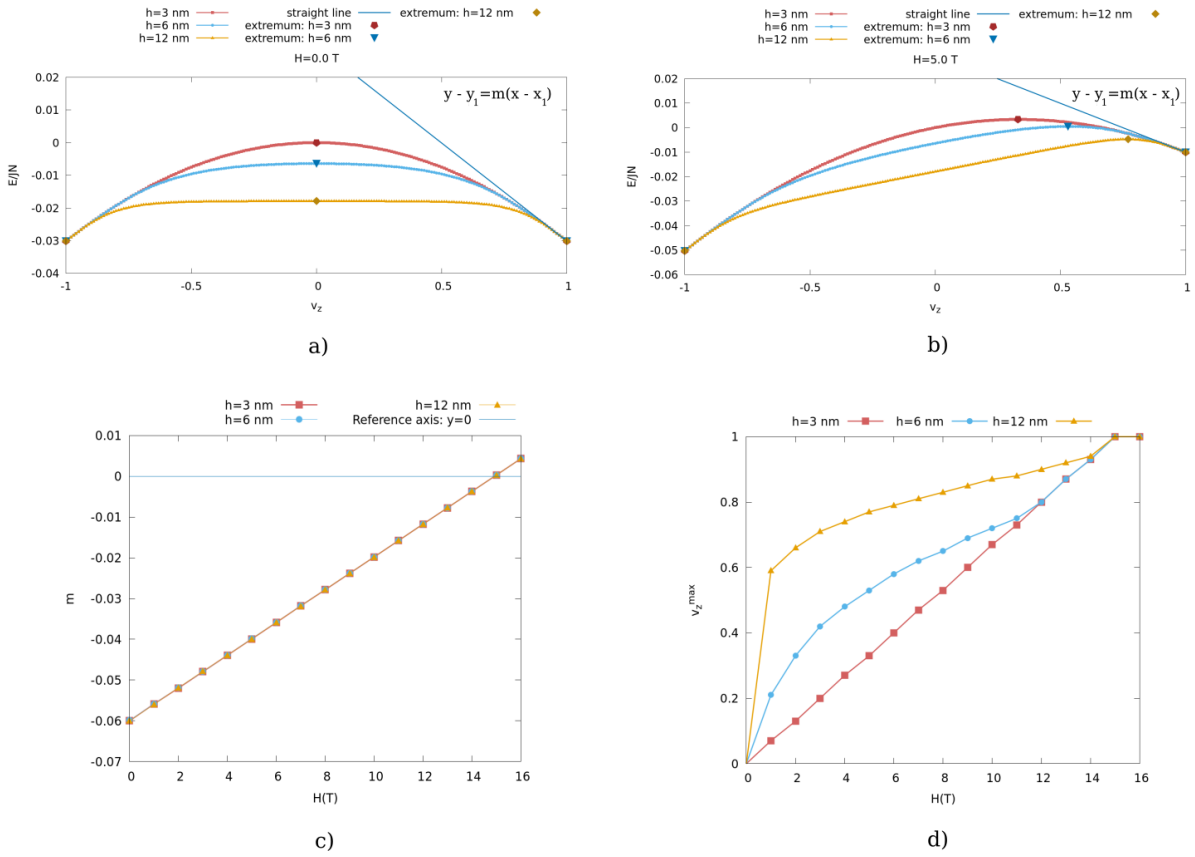

Figure 4.8: MEPs examples for a 3 nm (coherent), 6 nm and 12 nm grain in an external applied field of a) 0 T and b) 5 T respectively. We geometrically construct individual straight lines - using the equation given in the top right corner of the plots - passing through the first two right-hand side points on each $E = f(v_z)$ curve. This process is repeated for the whole field range of $[0T \rightarrow 16T]$ and the slope of the straight line is extracted. Its variation with respect to H is plotted in subfigure c) for all three grain heights. The position of the maximum energy points on the MEPs as a function of H is displayed in subplot d).

The displacement of the maximum energy points across the surface of the MEPs is the second effect arising as a consequence of the applied field. Referring back to the subplots a) and b) of Figure 4.8, it can be seen how an increase in H from 0 T to 5 T will move the

energy maxima towards the right hand side region of the $E = f(v_z)$ curves. Extracting the v_z position of the maxima (v_z^{max}) as a function of the applied field strength for all three grain sizes, we obtain the result in Figure 4.8.d). In the case of the coherent grain, the maximum energy point is displaced linearly as H is increased. After the anisotropy field is reached, the energy maximum will correspond to the $v_z = +1$ configuration. Due to a change in the MEP curvature, the initial $v_z^{max} = f(H)$ variation strongly deviates from the linear case for both the 6 nm and 12 nm grain heights. However, as the field increases above a certain threshold governed by the height of the grain, v_z^{max} enters the coherent region. In this limit, energy barrier calculations for a coherent and non-coherent reversing grain will yield the same result. Thus, the irreversible switching of the average magnetisation vector will take place at the same critical field equal to H_k.

One final comment takes note of the results obtained by Forster et al. within their micromagnetic study of elongated grains [16]. There, in the figure labeled as "Fig.7", it is shown that for an $\frac{H_k}{M_S}$ ratio of 37.7 - in units of Oe(emu/cc)$^{-1}$ - H_c becomes weakly dependent on the grain size and it remains close to the H_k value within a 20% margin. Preserving the units, $\frac{H_k}{M_S}$ is approximately equal to 146 in our case, which represents a good reason for neglecting the magnetostatic effects but also an additional argument for the identical coercivity values we obtain irrespective of the grain height.

Initial bi-layer results

This chapter constitutes a summary of the work-in-progress study based on systems consisting of hard/soft coupled materials. Its aim is to outline a qualitative description of the optimum paths of reversal we obtain and the limitations we have been facing. In the first section we will provide the material parameters used throughout this chapter, as well as refer to the context and demands in the current magnetic recording industry. We will then focus our attention on the numerical strategy implemented in the analysis of composite media, after which we will describe the present shortcomings of the approach. A two spin system will be used as a basis for these observations. To visualise the reversal process in realistic bi-layer structures, we will discuss examples of MEPs in two other hard/soft geometries. Following this, we will demonstrate the role of the interfacial exchange coupling in governing the reversal process and the energy barriers in the composite systems we study. Additionally, atomistic spin dynamics simulations will reveal the advantage offered by hard/soft exchange coupled layers over single-phase media, based on the switching field variation with respect to the interlayer exchange.

1 Material parameters

An improvement over the accessible AD in conventional PMR and CGC media designs ($\approx 300 \rightarrow 400$ Gbits/in^2 [85]), has been achieved using hard/soft composite structures which offer an elegant solution to the writability issue outlined in the magnetic trilemma. In both the ECC structure introduced by Victora and Shen [10] and the ES media suggested by Suess et al. [11], the hard phase represents the recording material which needs to satisfy the standard thermal stability requirement, while the additional soft layer is used to aid the switching process. Assuming both layers to be first magnetised along the $+z$ direction, a reverse magnetic field will initially promote a switching event in the soft phase due to its lower anisotropy component. Depending on the design, the coercivity of the hard layer

will be lowered due to a domain wall assisted process or coherent based mechanism, thus facilitating its reversal [86]. The relevance of the hard/soft composite structures has been rekindled in the context of heat-assisted recording due to the work of Suess and Schrefl [14]. They have shown how in an Fe/FePt bilayer system, the higher T_c of the Fe phase preserves a sufficiently large magnetisation near the writing temperature of the FePt recording layer, which overall leads to a lowered BER and a predicted AD of over 50 Tbits/in^2. An experimental study from the same year outlined the behaviour of coupled composites for different soft materials. It was confirmed that low-anisotropy [Co/Ni] or [Co/Pt] multilayers increase the thermal stability of the system in comparison to Fe [87]. As it was previously mentioned, the future HAMR technology imposes the use of highly anisotropic materials such as $L1_0$FePt characterised by $K \approx 10^7\ J/m^3$ [77, 78].

The results presented in this final chapter of the thesis are based on a generic hard/soft spin chain system modelled using the material parameters listed in Table 4.

Material / Parameter (Units)	Soft	Hard
J_{ij} (Joules)	8.87×10^{-21}	6.82×10^{-21}
k_u (Joules)	1.89×10^{-23}	2.41×10^{-22}
μ_s (μ_B)	2.03	3.05
a (Å)	3	3

Table 4: Atomistic parameters of the hard/soft bilayer system simulated throughout this chapter. The interfacial exchange strength is modelled as a percentage $p \in [0\% \rightarrow 100\%]$ of the intralayer J_{ij} in the hard phase.

The anisotropy field of the hard layer amounts to 17 T, a value more than eight times larger than the one corresponding to the soft phase: 2 T. Compared to the parameters used in the previous chapter, the atomistic k_u value of the hard layer corresponds to a macroscopic anisotropy of $K = 8.9 \times 10^6\ J/m^3$, while μ_s is linked to a saturation magnetisation of approximately: $M_S = 1050\ kA/m$. The exchange constants give rise to a lower T_c point in the hard material ($695K$) in comparison to the soft counterpart ($905K$). The strength of the exchange interaction J_{int} at the interface, varies as a percentage $p \in [0\% \rightarrow 100\%]$ of the intralayer exchange in the hard phase. For both materials, we consider an identical lattice spacing of 3Å . The layer heights or equivalently the number of spins in each of the two magnetic phases are varied according to the problem at hand.

2 NOTES ON METHODOLOGY

A study of bi-layer systems demands a closer look at the constraint shape in use. In equation (3.35), we introduced a general constraint term later put to test in the case of single-phase magnetic materials (as seen in the previous Chapter). For the two phase spin structures we are now interested in - see Figure 5.1 - we need to redefine the global magnetisation vector $\boldsymbol{v}$ as follows:

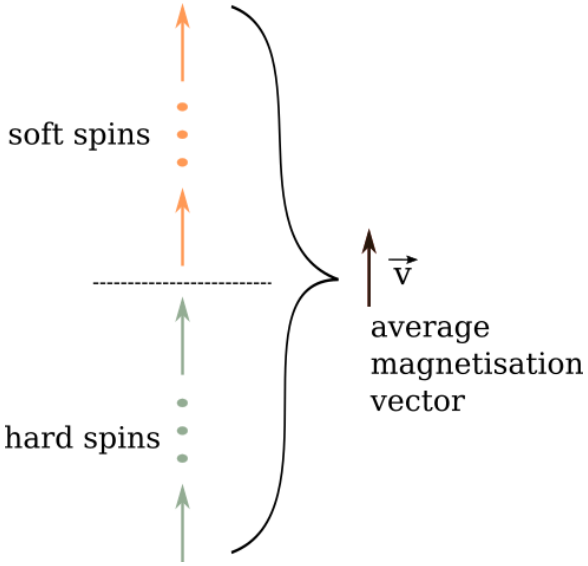

Figure 5.1: Schematic representation of a generic hard/soft chain system.

$$\boldsymbol{v} = \frac{1}{N_S + N_H} \sum_i \boldsymbol{s}_i, \tag{5.1}$$

where N_S and N_H represent the total number of soft and hard spins respectively. As an example, in this section we will attempt to obtain the zero-field MEP for a system consisting of two decoupled spins ($N_S, N_H = 1$ and $J_{int} = 0$). At first, we will apply the same numerical procedure used previously for single-phase materials but adopting the new definition of the $\boldsymbol{v}$ vector. The results of this simulation labelled as "case 1", can be seen in Figure 5.2.a). The corresponding spin configurations are plotted separately for the hard and soft components in subfigure b). As the global magnetisation vector deviates from the equilibrium position, the soft spin is the first one to reverse. Its rotation yields a local maximum energy on the MEP, corresponding to $v_z = 0.5$. Following this, the soft spin relaxes towards the -z direction which leads to a zero average magnetisation due to the antiparallel configuration of the spins.

A natural follow-up, the reversal of the hard phase is unfortunately accompanied by a sudden energy jump at $v_z = -0.54$. The reason behind it finds its explanation in the shape of the constraint in use. We need to keep in mind that equation (3.35) introduces constraint fields on x, y and z which act simultaneously on both spins. The x and y components, applied transverse with respect to the EA, aid the switching of the hard phase but can alter the $-z$ reversed position of the soft spin. Once this happens, the large z constraint field needed to balance the anisotropy of the hard phase, pushes the soft spin towards the $+z$ direction leading to the observed energy jump. A simple strategy to avoid such events is to cancel the Lagrange fields acting on the soft phase after its reversal process has been finalised or just

before the unwanted jump occurs. Using this procedure, we obtain the expected MEP as suggested by the curve labelled "case 2" in Figure 5.2.a); accompanying spin configurations are given in subplot c).

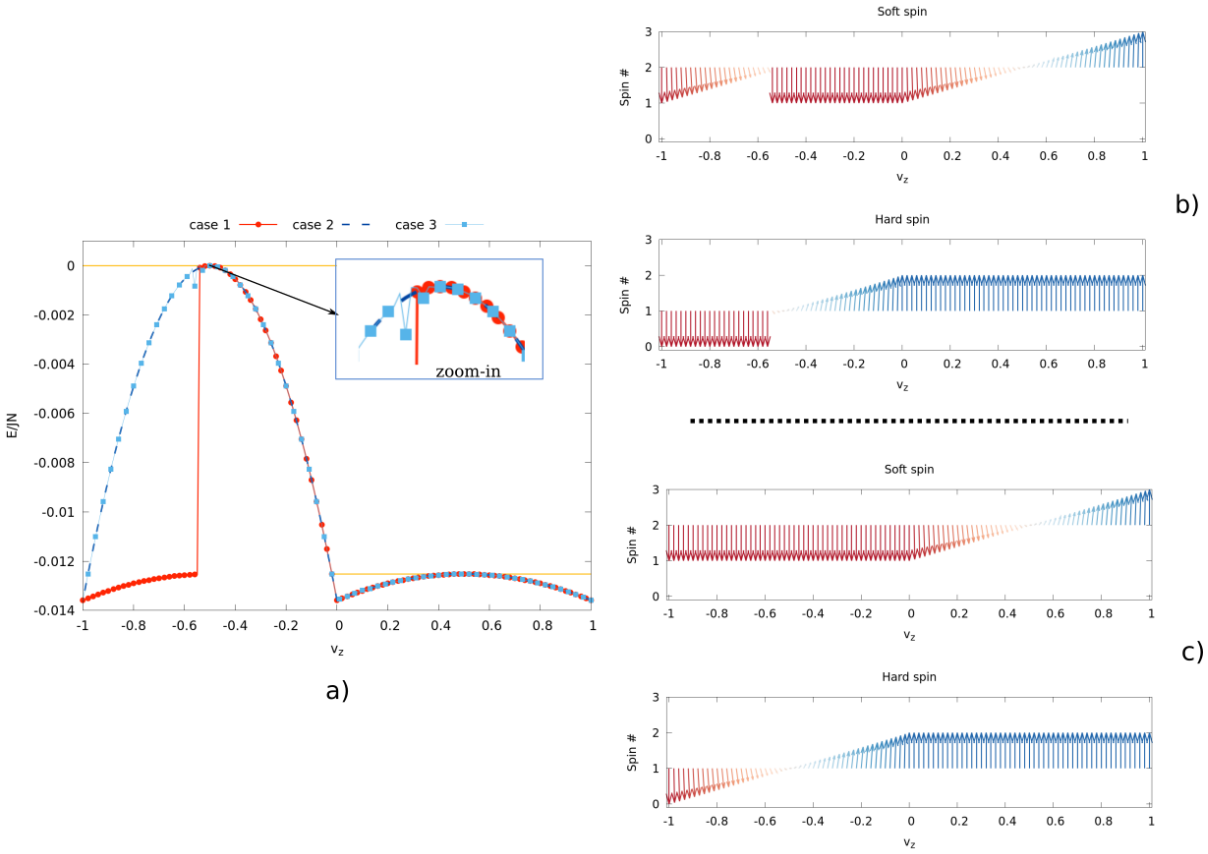

Figure 5.2: Reversal process in a two spin, hard/soft chain system. a) MEPs obtained using different numerical strategies: case 1 - the constraints defined by (3.35) act on both spins all throughout the reversal process; case 2 - once the soft phase is reversed, the constraints acting on this layer are cancelled; case 3 - we consider x and z constraints in the hard layer and a single z constraint in the soft layer; this trial procedure suffers from convergence issues as seen in the zoomed-in box. The y-axis is normalised to the maximum exchange constant and the total number of spins. The yellow horizontal lines mark the energy maxima during each of the spins' reversal. Subplots b) and c) accompany the first two MEPs defined as "case 1" and "case 2"; the Oxz configurations of the hard and soft spins in both situations are displayed in separate boxes for clarity. The "Spin #"-axis centers the origin of the spin vectors according to their position in the chain: 1 for the hard spin, 2 for the soft counterpart.

Cancelling out the constraints acting on the soft layer requires the *a priori* knowledge of the v_z coordinate corresponding to an energy jump. A future study will have to focus its attention on adapting the constraint term to bi-layer systems in order to develop a generally

applicable algorithm. An initial trial has been made using the following implementation. For ease of equilibration, an x and z constraint are allowed in the hard layer: $-\lambda_x v_x(v_z - v_{0z}) - \lambda_z(v_z - v_{0z})$. Attempting to avoid the previously discussed energy jumps along the MEP, we limit the constraints acting on the soft layer to a z component only: $-\lambda_z(v_z - v_{0z})$. The reversal path obtained using this method is labelled as "case 3". Despite offering the opportunity for general use, this particular approach lacks a rapid convergence rate and may lead to inaccuracies along the MEP - see zoom-in box in Figure 5.2.a). In the following sections of this chapter, we shall make use of the strategy outlined in the "case 2" result.

3 MINIMUM ENERGY PATHS

In this section, we will move away from the two spin system described earlier towards a more realistic representation of a hard/soft structure. We will consider initially examples of MEPs with the aim of describing the main details in the reversal of a composite system. Both the thermal stability aspect and the switching factor in hard/soft media are influenced by a range of parameters. Here, we will consider only the role played by the interfacial exchange coupling. Atomistic spin dynamics simulations will provide an additional point of view in the final discussions of this section.

3.1 Initial examples

In what is to follow, we will use our adapted numerical approach to visualise MEP examples in two hard/soft composites. We recall that the objective in this chapter is to offer a qualitative analysis only, due to the limitations described in the previous section. In both examples below, we consider a hard layer with a height equal to 9 nm; given the lattice constant defined in Table 4, N_H evaluates to 30 spins. Two soft layer heights will be discussed: 3 nm (N_S = 10 spins) and 21 nm (N_S = 70 spins) respectively. The interlayer exchange strength is set to J_{int} = 1% and no external field is considered.

The result presented in Figure 5.3, corresponds to the 9 nm/3 nm composite system. Initially, both layers are magnetised along the +z direction; with the average magnetisation vector constrained to deviate from the EA, the soft spins are first to rotate away from their equilibrium position. Since in this case the height of the soft layer is much smaller than the Bloch wall width ($\delta_B^{Soft} \approx 14.5$ nm), its reversal process follows a coherent mechanism. A local energy maximum is found at $v_z = 0.7$, standing for an in-plane configuration of the soft spins. Due to the presence of the interfacial coupling, the two energy minima at $v_z = 1.0$ and

$v_z = 0.5$ - corresponding to the ± z orientations of the soft layer - are not symmetric about the local maximum point which separates them. Because of its large anisotropy, the hard phase is characterised by a small Bloch wall width ($\delta_B^{Hard} \approx 3.5$ nm). The 9 nm height will thus allow a non-coherent magnetisation process as the hard layer starts to reverse. A final maximum energy point is found at $v_z = -0.25$, after which the system relaxes towards the -z configuration.

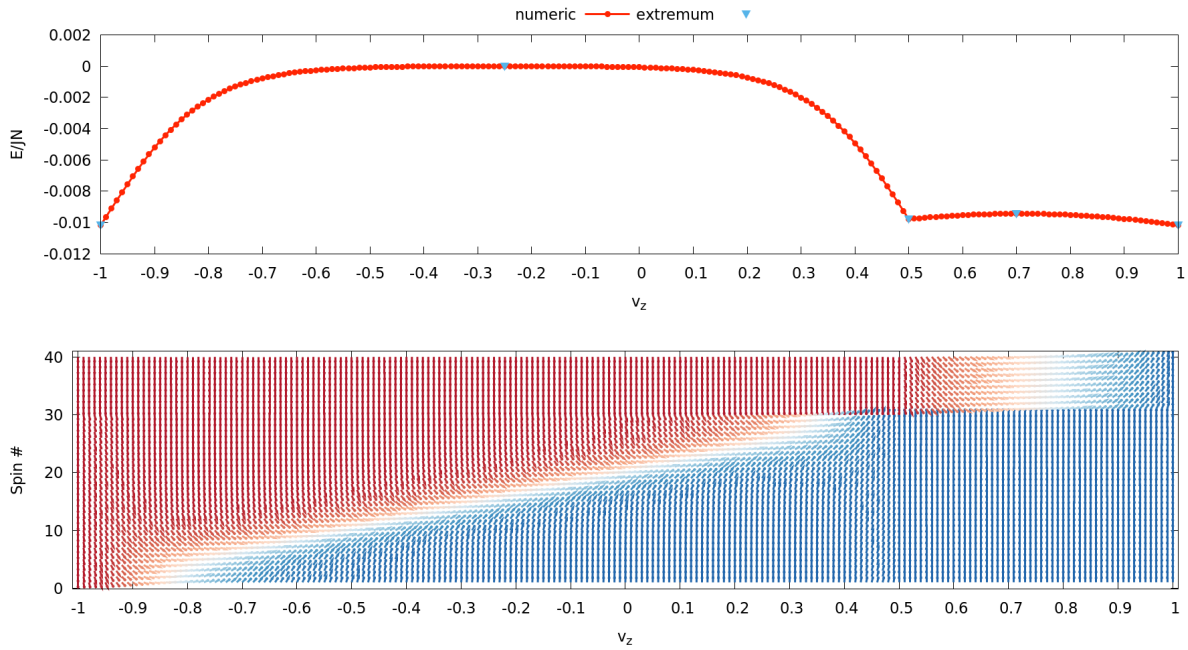

Figure 5.3: 9 nm/3 nm hard/soft composite system. Above: MEP - the y axis is normalised to the maximum exchange constant and the total number of spins. For ease of visualisation, the energy is shifted such that the maximum point along the MEP corresponds to 0. Below: spin configurations in the Oxz plane. The "Spin #"-axis gives a the spin id or position in the chain.

In real magnetic recording applications, the height of both the hard and soft layers are important extrinsic parameters to consider. The thermal stability aspect is largely determined by the hard component. From the previous chapter, we recall how the energy barrier of a single phase system saturates for a layer thickness above the Bloch wall width. Simply put, the thermal stability factor cannot be improved above this threshold. It is therefore required that the hard layer is designed such that a domain wall can be accommodated across its length. In terms of switching, it has been previously shown how the domain wall assisted magnetic recording (DWAMR) is more advantageous in comparison to the coherent based mechanism in the ECC design [12]. In DWAMR (also known as the ES regime), the reversal process starts with a domain wall nucleation in the soft layer. Under the increasing strength of the external

field, the domain wall propagates towards the hard/soft interface where it is compressed and finally pushed in the hard phase for a "de-pinning" field value. For this reversal process to be allowed, Dobin and Richter impose as a necessary condition, soft and hard layers thick enough to fit the interfacial domain wall [12, 13]. Compared to the traditional Bloch wall width, the critical length parameter (l_{cr}) defined in their work takes into account the strength of the applied field. For an infinitely soft material, l_{cr} can be approximated by: $a\sqrt{\frac{J}{\mu_s H}}$; we can see from this formula that an increase of the external applied field leads to a reduction of the wall width, thus making nucleation events possible even in very thin soft materials. Since in zero applied field the domain wall width is maximum, we can use the Bloch length parameter (δ_B) as a safe threshold for the ES regime.

In the example given in Figure 5.4, we consider a 9 nm/21 nm hard/soft composite system in zero field, with both layers larger than their corresponding Bloch wall widths. Due to its greater thickness, the MEP is dominated by the reversal of the soft layer; compared to the previous case, both phases follow incoherent magnetisation processes. Points of

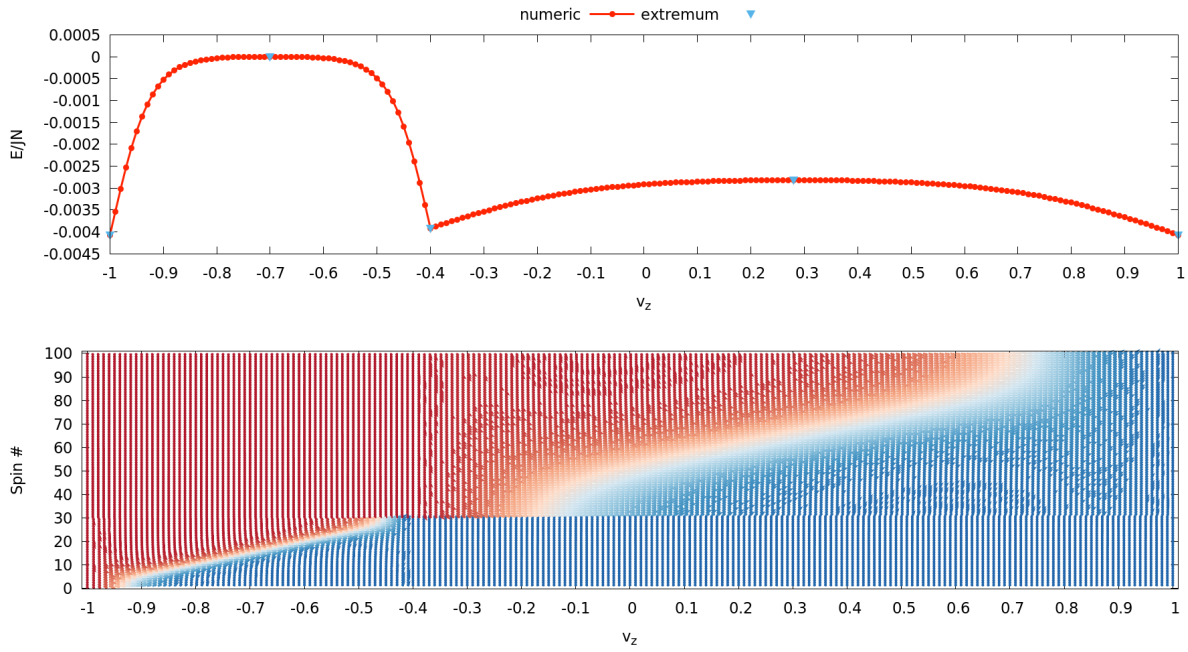

Figure 5.4: 9 nm/21 nm hard/soft composite system. Above: MEP - the y axis is normalised to the maximum exchange constant and the total number of spins. For ease of visualisation, the energy is shifted such that the maximum point along the MEP corresponds to 0. Below: spin configurations in the Oxz plane.

maxima, governed by the wall energies of the two layers, are found for $v_z = 0.28$ and $v_z = -0.7$ respectively. Once again, due to the presence of the interlayer exchange, the minimum energy

states corresponding to the ± z configurations of either the hard or the soft phase, are not symmetric with respect to the local maxima separating them.

3.2 The role of the interlayer exchange

The exchange coupling at the hard/soft interface can significantly influence the reversal process of the system. To demonstrate its role, we will make use of the two bi-layer geometries described in the previous section. The results presented in Figure 5.5, display zero-field MEPs obtained for several J_{int} values ranging from 0% to 100% coupling.

In subplot a), we discuss the 9 nm/3 nm hard/soft system. For 0% interlayer exchange, the MEP is characterised by two distinct energy barriers, demonstrating the independent reversal processes of the two layers. As the strength of the coupling is increased, the local minimum found initially at $v_z = 0.5$ is steadily vanishing. Concurrently, it is clear to see that the MEP becomes less dependent on the interfacial exchange value; above an approximate limit of $J_{int} = 25\%$, there is no significant variation of the energy surface during the reversal of the soft phase. Interestingly, the zero field energy barrier of the hard phase remains constant for all interlayer exchange strengths.

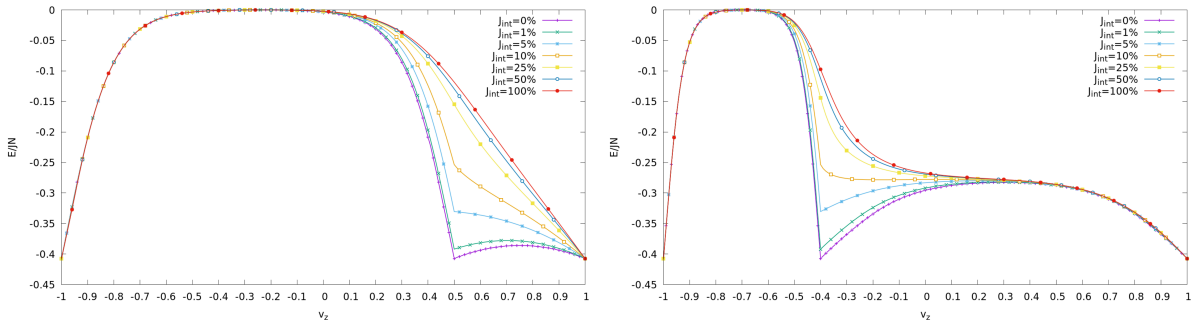

a) b)

Figure 5.5: MEPs as a function of the interlayer exchange strength: a) 9 nm/3 nm bilayer; b) 9 nm/21 nm bilayer.

The right-hand side section of Figure 5.5, displays the results obtained for the 9 nm/21 nm bilayer system. The given MEPs present a similar behaviour when compared to the previous case, with the main difference being the non-coherent reversal of the soft material. For very small coupling strengths, the two layers switch from the up to the down state independently as there are distinct energy barriers present along the optimum path. Once again, with an increase in J_{int} above 25%, the -z equilibrium configuration of the soft layer dissapears and the MEP remains unchanged, irrespective of the coupling strength. Unlike the 9 nm/ 3nm

case, the energy barriers characterising both the hard and soft materials can be considered constant to a good approximation. The most striking effect of varying the interlayer exchange remains confined near the hard/soft interface. Analytic energy barrier calculations in hard soft systems are traditionally defined either in the limit of the macrospin approximation [88] or the domain-wall assisted magnetic recording [89]. In the latter case, it is predicted that the zero field energy barrier of the bi-layer structure is defined by the domain wall energy of the hard phase in the limit of strong coupling.

Atomistic spin dynamics (ASD) simulations - see Figure 5.6 - reveal the greater importance played by the interfacial exchange strength in determining the switching of the bi-layer structure. One of the main aims in composite media systems is to reduce the otherwise large coercivity of the hard phase below the strength of the available write field. As it can be seen from the results below, at a 0% interlayer coupling, the switching field needed to reverse the hard layer is equal to the anisotropy field (17 T). In both geometries we considered, a rapid coercivity reduction is observed as J_{int} approaches the 20% margin; on average, the switching field decreases by a 2.5 factor near this coupling threshold.

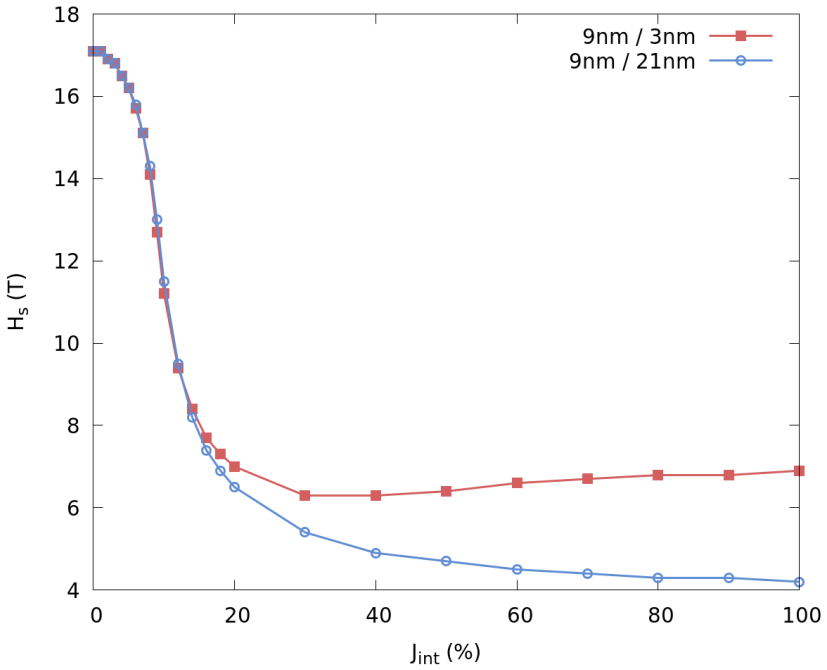

Figure 5.6: ASD simulations revealing the importance of the interlayer exchange in lowering the switching field of the hard phase. The results presented in this figure were obtained by Sergiu Ruta; permission for use has been granted.

Further increasing the interlayer exchange leads to divergent $H_s = f(J_{int})$ variations. In the 9

nm /3 nm bi-layer structure, H_s increases at a steady rate up to an approximate value of 7 T in the limit of full coupling. On the other hand, the domain-wall assisted reversal in the 9 nm/21 nm system, leads to a continuous reduction of the switching field up to a minimum value of 4.2 T. It is worth pointing out that in this case we obtain the critical pinning field strength predicted by Kronmüller and Goll in their micromagnetic treatment of phase boundaries [90].

Conclusions

In this work, we developed a direct minimisation procedure based on the gradient descent algorithm, aimed at mapping MEPs of reversal for spin chain systems. Such an analysis has the potential to identify energy barriers between different magnetic configurations of equilibrium which later can help infer the long term thermal stability of a given recording medium.

Initially, we applied our method for a single phase system - the opening section of the "Monolayer results" chapter defines the parameters we used. We first discussed standard examples of MEPs along with their corresponding spin configurations obtained for coherent and domain wall governed switching. Following this, we argued the nature of the domain walls nucleated in the spin chain systems we simulate. From a rotational point of view, a Néel description should be applied, but in the absence of any demagnetising effects the Bloch model can be used. The magnetisation profile of a grain in the remanent state gave an initial confirmation of the previous statement. Next, we analysed how the reversal mechanism can be controlled with a variation of the grain height. When the size of the system is smaller than the domain wall width (δ_B), the coherent reversal is preferred and the numerical energy barrier is seen to agree with the value obtained within the SW model. As the system grows in height over the δ_B limit, the numerical barrier converges towards the energy required to nucleate a Bloch domain wall. This result is particularly important as it offered us an initial validation of the implemented model. In addition, the direct minimisation procedure has also been shown to match with the interpretation offered by the dynamic method based on the LLG equation. Furthermore, we successfully replicated the energy barrier variation as a function of the applied field strength in the SW description. Analysing MEPs in grains larger than their corresponding Bloch wall widths, we observed that for a field applied parallel to the EA, the coercivity is equal to the value exhibited by single domains. Our results are consistent with the micromagnetic analysis of elongated grains done by Forster et al. [16] in which it is shown that for large H_k/M_s ratios, the coercivity is weakly dependent on the grain size.

In the chapter dedicated to bi-layer systems, we discuss the current status of our work and the present limitations. The choice of the constraint term can affect the overall shape of the MEP; a thorough analysis of the Lagrange multiplier technique in composite media shall be the focus of a future study. For now, we limited ourselves to a qualitative description of the reversal process in hard/soft systems based on two given geometries. The role of the interfacial exchange strength has been discussed in regards to the thermal stability of the medium. In our simulations, the energy barrier characterising the hard layer is independent of the interfacial exchange coupling. On the other hand, ASD simulations reveal the advantage of composite systems over single phase media: for a critical coupling strength, the field required to switch the magnetisation of the hard phase is significantly lowered. On average, for a J_{int} of approximately 20%, the switching field in our hard/soft systems is reduced by a factor of 2.5 compared to the coercivity of the stand-alone hard phase.

1 FUTURE WORK

The model implemented in this thesis showed a good applicability in single phase media; therefore, a natural follow-up of the present study would be to extend the evaluation of MEPs and corresponding energy barriers for a wide range of parameters in monolayer systems. As a start, the transition between coherent rotation and domain wall assisted reversal can be investigated as a function of the exchange and anisotropy values. Such an analysis can provide the critical grain size needed to yield the maximum thermal stability factor. Since the results presented here are strictly valid at $0K$, a temperature related study can be sought. Using for example the Callen-Callen scaling laws of the anisotropy and magnetisation terms [91], temperature dependent energy barriers could be investigated such that a more realistic view of thermal stability in grains is acquired. According to the SW theory, the coercivity can be lowered by deviating from the parallel orientation of the external field with respect to the EA; using our numerical approach and an analytic description similar to the one given in equation (4.5), $\Delta E = f(H)$ curves could be investigated for different applied field geometries.

In the case of bi-layer systems, the present model is limited due to the choice of the constraint term. According to the work in [86], another idea that could be applied for hard/soft composite media would be to allow separate constraints in both materials which may lead to the removal of the observed sudden energy jumps in the MEP. Furthermore, the energy landscape in our study is parametrised as $E = E(v_z)$, where v_z is obtained by summing over all the spins in the system. To reveal hidden energy barriers in bi-layer structures, the energy landscape should be evaluated as $E = E(v_z^{soft}, v_z^{hard})$, where v_z^{soft} and v_z^{hard} take into

account only the soft and hard spins respectively.

A method of investigating MEPs of reversal and extracting the corresponding energy barriers could be potentially used in conjunction with the Kinetic Monte-Carlo (KMC) model [92]. The latter numerical algorithm allows long-time scales simulations of magnetic systems, otherwise not accessible via the LLG equation. For example, one can use the KMC approach in order to accurately fit experimental $M-H$ curves within the $ms \rightarrow s$ time-frame [93] or predict the magnetisation decay of thermally activated grain structures over periods spanning decades [94]. At its core, the KMC method employs probabilistic calculations which govern local relaxation processes according to the Néel-Arrhenius transition theory. For an accurate recording media description, the KMC algorithm would require energy barrier parametrisation which can describe both coherent and non-coherent grain reversal. Since general analytic ΔE expressions are difficult to define, investigations using the KMC method have been so far based on the SW picture. The numerical 1D model described in our work could facilitate long-term magnetic recording studies by providing energy barrier input into the KMC algorithm.

Nomenclature

List of Abbreviations

1D One-dimensional

AD Areal density

ASD Atomistic Spin Dynamics

ASRC Advanced Storage Research Consortium

ASTC Advanced Storage Technology Consortium

bcc Body-centered cubic

BPMR Bit Patterned Magnetic Recording

CGC Coupled Granular Continuous

DFT Density Functional Theory

EA Easy-axis

ECC Exchange Coupled Composite

ES Exchange Spring

fcc Face-centered cubic

HAMR Heat Assisted Magnetic Recording

HDD Hard-disk-drive

LLB Landau-Lifshitz-Bloch

LLG Landau-Lifshitz-Gilbert

MEP Minimum Energy Path

NEB Nudged Elastic Band

PMR Perpendicular magnetic recording

RKKY Ruderman-Kittel-Kasuya-Yosida

sc Simple cubic

SNR Signal-to-noise ratio

SOT Spin-orbit-torque

STT Spin-transfer-torque

SW Stoner-Wohlfarth

TDDFT Time Dependent Density Functional Theory

List of Symbols

α Damping constant

$\boldsymbol{\tau}$ Torque

$\boldsymbol{B}$ Magnetic induction

$\boldsymbol{d}$ Search direction

$\boldsymbol{H}$ Magnetic field

$\boldsymbol{H}_d$ Demagnetising field

$\boldsymbol{H}_m$ Molecular field

$\boldsymbol{H}_{eff}$ Effective field

$\boldsymbol{J}_t$ Total angular momentum

$\boldsymbol{L}$ Total orbital angular momentum

$\boldsymbol{l}$ Angular momentum

$\boldsymbol{M}$ Volume magnetisation

$\boldsymbol{m}$ Magnetic dipole moment

$\boldsymbol{n}$	Easy-axis unit vector
$\boldsymbol{r}$	Position vector
$\boldsymbol{S}$	Total spin angular momentum
$\boldsymbol{s}$	Spin vector
$\boldsymbol{v}$	Average magnetisation vector of the spin chain system
$\boldsymbol{v}_0$	Target magnetisation
χ	Magnetic susceptibility
ΔE	Energy barrier
δ_B^*	Micromagnetic Bloch wall width
δ_B	Atomistic Bloch wall width
ϵ	Spin-wave correction factor
γ	Gyromagnetic ratio
$\hbar$	Reduced Planck constant
λ	Lagrange multiplier
$\mathscr{H}_{exch}$	Exchange Hamiltonian
$\mathscr{H}_{ext}$	Zeeman Hamiltonian
$\mathscr{H}_{total}$	Total Hamiltonian
$\mathscr{H}_{uni}$	Uni-axial anisotropy Hamiltonian
$\mathscr{L}$	Lagrangian function
μ	Magnetic permeability
μ_0	Vacuum permeability
μ_B	Bohr magneton
μ_s	Atomic spin magnetic moment

ψ	Total wave function
ρ	Spatial wave function
θ	The angle between the magnetisation/magnetic moment vector and the easy-axis
θ_0	Angle between external field and easy-axis
ξ	Spin wave function
A	Exchange stiffness
a	Lattice spacing
A_{loop}	Loop surface area
E	Total energy
e	Elementary charge
E^*_{DW}	Approximate domain-wall energy
E_{DW}	Exact domain-wall energy
E_{ms}	Magnetostatic energy
E_{SW}	Stoner-Wohlfarth energy
$f(\boldsymbol{\phi})$	Generic function of $\boldsymbol{\phi}$ variables
g	Landé g-factor
$g(\boldsymbol{\phi})$	Generic constraint of $\boldsymbol{\phi}$ variables
H_c	Coercivity
H_K	Micromagnetic anisotropy field
H_k	Atomistic anisotropy field
H_n	Nucleation field
H_p	Pinning field
H_s	Switching field

H_w	Strength of write field
I	Current intensity
i, j	Indices
J_{ij}	Exchange constant corresponding to interaction between spins i and j
J_{int}	Interfacial exchange strength
K	First-order magnetocrystalline anisotropy constant
k_B	Boltzmann constant
k_u	Uni-axial anisotropy constant of atomic site
m_0	Electron rest mass
M_S	Saturation magnetisation
N	Number of particles (spins, atoms etc.) or dimensions
n	Number of particles in a given unit volume
n_W	Weiss Coefficient
n_{at}	Number of atoms in the unit cell
R	Radius
T	Temperature
T_c	Curie temperature
V	Volume
W	Energy band width
z	Number of nearest-neighbours

References

[1] D. Reinsel, J. Gantz, and J Rydning. https://www.seagate.com/files/www-content/our-story/trends/files/idc-seagate-dataage-whitepaper.pdf, 2018.

[2] https://www.ibm.com/ibm/history/exhibits/storage/storage_350.html.

[3] https://www.seagate.com/gb/en/news/news-archive/terabit-milestone-storage-seagate-master-pr/, 2012.

[4] H. J. Richter, A. Lyberatos, U. Nowak, R. F. L. Evans, and R. W. Chantrell. The thermodynamic limits of magnetic recording. *Journal of Applied Physics*, 111(3):033909, 2 2012.

[5] K. Hono and Y. Takahashi. L10–FePt Granular Films for Heat-Assisted Magnetic Recording Media. In *Ultra-High-Density Magnetic Recording*, pages 245–277. Pan Stanford, 3 2016.

[6] http://idema.org/?page_id=416.

[7] R. E. Rottmayer, S. Batra, D. Buechel, W. A. Challener, J. Hohlfeld, Y. Kubota, L. Li, B. Lu, C. Mihalcea, K. Mountfield, K. Pelhos, C. Peng, T. Rausch, M. A. Seigler, D. Weller, and X. M. Yang. Heat-Assisted magnetic recording. *IEEE Transactions on Magnetics*, 42(10):2417–2421, 2006.

[8] T. R. Albrecht, H. Arora, V. Ayanoor-Vitikkate, J-M Beaujour, D. Bedau, D. Berman, A. L Bogdanov, Y-A Chapuis, J. Cushen, E. E Dobisz, G. Doerk, H. Gao, M. Grobis, B. Gurney, W. Hanson, O. Hellwig, T. Hirano, P-O Jubert, D. Kercher, J. Lille, Z. Liu, C. M. Mate, Y. Obukhov, K. C Patel, K. Rubin, R. Ruiz, M. Schabes, L. Wan, D. Weller, T-W Wu, and E. Yang. Bit Patterned Magnetic Recording: Theory, Media Fabrication, and Recording Performance. *IEEE Transactions on Magnetics*, 51(5), 5 2015.

[9] Y. Sonobe, D. Weller, Y. Ikeda, M. Schabes, K. Takano, G. Zeltzer, B. K. Yen, M. E. Best, S. J. Greaves, H. Muraoka, and Y. Nakamura. Thermal stability and SNR of coupled

granular/continuous media. In *IEEE Transactions on Magnetics*, volume 37, pages 1667–1670, 7 2001.

[10] R. H. Victora and X. Shen. Exchange coupled composite media for perpendicular magnetic recording. In *IEEE Transactions on Magnetics*, volume 41, pages 2828–2833, 10 2005.

[11] D. Suess, T. Schrefl, S. Fähler, M. Kirschner, G. Hrkac, F. Dorfbauer, and J. Fidler. Exchange spring media for perpendicular recording. *Applied Physics Letters*, 87(1):012504, 7 2005.

[12] A. Yu Dobin and H. J. Richter. Domain wall assisted magnetic recording. *Applied Physics Letters*, 89(6):062512, 8 2006.

[13] A. Yu Dobin and H. J. Richter. Domain wall assisted magnetic recording (invited). In *Journal of Applied Physics*, volume 101, page 09K108. American Institute of Physics (AIP), 5 2007.

[14] D. Suess and T. Schrefl. Breaking the thermally induced write error in heat assisted recording by using low and high Tc materials. *Applied Physics Letters*, 102(16):162405, 4 2013.

[15] R. Dittrich, T. Schrefl, D. Suess, W. Scholz, H. Forster, and J. Fidler. A path method for finding energy barriers and minimum energy paths in complex micromagnetic systems. *Journal of Magnetism and Magnetic Materials*, 250:12–19, 9 2002.

[16] H. Forster, N. Bertram, X. Wang, R. Dittrich, and T. Schrefl. Energy barrier and effective thermal reversal volume in columnar grains. *Journal of Magnetism and Magnetic Materials*, 267(1):69–79, 11 2003.

[17] O. Fruchart. *Lecture notes on nanomagnetism*. Institut Néel (CNRS & UJF) - Grenoble, 2012.

[18] D. Jiles. *Introduction to Magnetism and Magnetic Materials*. CRC Press, 3rd edition edition, 2015.

[19] G. Bertotti. *Hysteresis in Magnetism*. Elsevier, 1998.

[20] P. Hohenberg and W. Kohn. Inhomogeneous electron gas. *Physical Review*, 136(3B):B864, 11 1964.

[21] F. Giustino. *Materials Modelling using Density Functional Theory: Properties and Predictions* . OUP Oxford, 2014.

[22] L. K. Wagner. Quantum Monte Carlo for Electronic Systems Containing d and f Electrons. In *Handbook of Materials Modeling*. Springer, 2020.

[23] P. Elliott, M. Stamenova, Jacopo Simoni, S. Sharma, S. Sanvito, and E. Gross. Time-Dependent Density Functional Theory for Spin Dynamics. In *Handbook of Materials Modeling*, pages 841–866. Springer International Publishing, 2020.

[24] J. Hubbard. Electron correlations in narrow energy bands. *Proceedings of the Royal Society of London. Series A. Mathematical and Physical Sciences*, 276(1365):238–257, 11 1963.

[25] The Hubbard model at half a century. *Nature Physics*, 9(9):523, 9 2013.

[26] H. Kronmüller. General Micromagnetic Theory. In *Handbook of Magnetism and Advanced Magnetic Materials*. John Wiley & Sons, Ltd, Chichester, UK, 12 2007.

[27] D. V. Berkov. Magnetization Dynamics Including Thermal Fluctuations: Basic Phenomenology, Fast Remagnetization Processes and Transitions Over High-energy Barriers. In *Handbook of Magnetism and Advanced Magnetic Materials*. John Wiley & Sons, Ltd, Chichester, UK, 12 2007.

[28] O. Chubykalo-Fesenko and P. Nieves. Landau-Lifshitz-Bloch Approach for Magnetization Dynamics Close to Phase Transition. In *Handbook of Materials Modeling*, pages 867–893. Springer International Publishing, 2020.

[29] E. Ising. Beitrag zur Theorie des Ferromagnetismus. *Zeitschrift für Physik*, 31(1):253–258, 2 1925.

[30] W. Heisenberg. Zur Theorie des Ferromagnetismus. *Zeitschrift für Physik*, 49(9-10):619–636, 9 1928.

[31] T. A. Ostler, J. Barker, R. F.L. Evans, R. W. Chantrell, U. Atxitia, O. Chubykalo-Fesenko, S. El Moussaoui, L. Le Guyader, E. Mengotti, L. J. Heyderman, F. Nolting, A. Tsukamoto, A. Itoh, D. Afanasiev, B. A. Ivanov, A. M. Kalashnikova, K. Vahaplar, J. Mentink, A. Kirilyuk, Th Rasing, and A. V. Kimel. Ultrafast heating as a sufficient stimulus for magnetization reversal in a ferrimagnet. *Nature Communications*, 3(6):1–6, 2 2012.

[32] U. Ritzmann, S. von Malottki, J-V Kim, S. Heinze, J. Sinova, and B. Dupé. Trochoidal motion and pair generation in skyrmion and antiskyrmion dynamics under spin–orbit torques. *Nature Electronics*, 1(8):451–457, 8 2018.

[33] R. M. Otxoa, U. Atxitia, P. E. Roy, and O. Chubykalo-Fesenko. Giant localised spin-Peltier effect due to ultrafast domain wall motion in antiferromagnetic metals. *Communications Physics*, 3(1):1–7, 12 2020.

[34] P. Chureemart, R. F.L. Evans, and R. W. Chantrell. Dynamics of domain wall driven by spin-transfer torque. *Physical Review B - Condensed Matter and Materials Physics*, 83(18):184416, 5 2011.

[35] K. Cai, Z. Zhu, J.M. Lee, R. Mishra, L. Ren, S. D. Pollard, P. He, G. Liang, K.L. Teo, and H. Yang. Ultrafast and energy-efficient spin–orbit torque switching in compensated ferrimagnets. *Nature Electronics*, 3(1):37–42, 1 2020.

[36] R. Skomski. *Simple Models of Magnetism*. OUP Oxford, 2008.

[37] P.W. Atkins and R.S. Friedman. *Molecular Quantum Mechanics*. Oxford University Press, 2010.

[38] B. D. Cullity and C. D. Graham. *Introduction to Magnetic Materials*. John Wiley & Sons, Inc., Hoboken, NJ, USA, 11 2008.

[39] J. Stöhr and H.C. Siegmann. *Magnetism: From Fundamentals to Nanoscale Dynamics* . 2006.

[40] K. H. J. Buschow and F. R. de Boer. *Physics of Magnetism and Magnetic Materials*. Springer US, 2003.

[41] P. Weiss. L'hypothèse du champ moléculaire et la propriété ferromagnétique. *Journal de Physique Théorique et Appliquée*, 6(1):661–690, 1907.

[42] W. Heitler and F. London. Wechselwirkung neutraler Atome und homöopolare Bindung nach der Quantenmechanik. *Zeitschrift für Physik*, 44(6-7):455–472, 6 1927.

[43] S. J. Blundell. *Magnetism in condensed matter*. Oxford University Press, 2001.

[44] N. A. Spaldin. *Magnetic materials: Fundamentals and applications*. Cambridge University Press, 2010.

[45] J. M.D. Coey. *Magnetism and magnetic materials.* Cambridge University Press, 2010.

[46] H. Barkhausen. Zwei mit Hilfe der neuen Verstärker entdeckte Erscheinungen. *Physik Z.*, 20, 1919.

[47] H. J. Williams and W. Shockley. A simple domain structure in an iron crystal showing a direct correlation with the magnetization. *Physical Review*, 75(1):178–183, 1 1949.

[48] F. Bitter. On inhomogeneities in the magnetization of ferromagnetic materials. *Physical Review*, 38(10):1903–1905, 11 1931.

[49] K. Futschik, H. Pfützner, A. Doblander, P. Schönhuber, T. Dobeneck, N. Petersen, and H. Vali. Why not use magnetotactic bacteria for domain analyses? *Physica Scripta*, 40(4):518–521, 10 1989.

[50] I. Manke, N. Kardjilov, R. Schäfer, A. Hilger, M. Strobl, M. Dawson, C. Grünzweig, G. Behr, M. Hentschel, C. David, A. Kupsch, A. Lange, and J. Banhart. Three-dimensional imaging of magnetic domains. *Nature Communications*, 1(8):1–6, 11 2010.

[51] F. Bloch. Zur Theorie des Austauschproblems und der Remanenzerscheinung der Ferromagnetika. *Zeitschrift für Physik*, 74(5-6):295–335, 5 1932.

[52] P. Anikeeva, G. Beach, and N. Holten-Andersen. 3.024 Electronic, Optical and Magnetic Properties of Materials, 2013.

[53] E. C. Stoner and E. P. Wohlfarth. A mechanism of magnetic hysteresis in heterogeneous alloys. *Philosophical Transactions of the Royal Society of London. Series A, Mathematical and Physical Sciences*, 240(826):599–642, 5 1948.

[54] A. Aharoni. Theoretical search for domain nucleation. *Reviews of Modern Physics*, 34(2):227–238, 4 1962.

[55] W. F. Brown Jr. Micromagnetics. *New York: Interscience Publisher*, 1963.

[56] H. Kronmüller. Theory of Nucleation Fields in Inhomogeneous Ferromagnets. *physica status solidi (b)*, 144(1):385–396, 11 1987.

[57] A. Aharoni. *Introduction to the Theory of Ferromagnetism.* Oxford University Press, 1996.

[58] A.H. Morrish. *The Physical Principles of Magnetism.* John Wiley & Sons, 2001.

[59] H. Kronmüller. Micromagnetism and the Microstructure of Modern Magnetic Materials. In *Magnetic Hysteresis in Novel Magnetic Materials*, pages 85–108. Springer Netherlands, 1997.

[60] G. Varvaro, A.M. Testa, E. Agostinelli, D. Peddis, and P. Laureti. Magnetic Characterization of Perpendicular Recording Media. In *Ultra High Density Magnetic Recording: Storage Materials and Media Designs*, chapter 8, pages 385–456. Pan Stanford Publishing, 2016.

[61] G. P. Zhao, H. W. Zhang, Y. P. Feng, Chun Yang, and C. W. Huang. Nucleation or pinning: Dominant coercivity mechanism in exchange-coupled permanent/composite magnets. *Computational Materials Science*, 44(1):122–126, 11 2008.

[62] R F L Evans, W J Fan, P Chureemart, T A Ostler, M O A Ellis, and R W Chantrell. Atomistic spin model simulations of magnetic nanomaterials. *Journal of Physics: Condensed Matter*, 26(10):103202, 3 2014.

[63] D. Garanin. Self-consistent Gaussian approximation for classical spin systems: Thermodynamics. *Physical Review B - Condensed Matter and Materials Physics*, 53(17):11593–11605, 5 1996.

[64] D.P. Bertsekas. *Constrained Optimization and Lagrange Multiplier Methods* . Academic Press, 1982.

[65] Nocedal J. and S.J. Wright. *Numerical Optimization*. Springer New York, 2006.

[66] J. V. Baxley and J. C. Moorhouse. Lagrange Multiplier Problems in Economics. *The American Mathematical Monthly*, 91(7):404–412, 8 1984.

[67] J.H. Mathews and K.K. Fink. *Numerical Methods Using Matlab*. Prentice Hall, 4th edition, 2004.

[68] W. H. Press, S.A Teukolsky, T. V. William, and B. P. Flannery. *Numerical Recipes in C++: The Art of Scientific Computing*. Cambridge University Press, 2002.

[69] J. Kiefer. Sequential Minimax Search for a Maximum. *Proceedings of the American Mathematical Society*, 4(3):502, 6 1953.

[70] L. Armijo. Minimization of functions having Lipschitz continuous first partial derivatives. *Pacific Journal of Mathematics*, 1966.

[71] P. Wolfe. Convergence conditions for ascent methods. *SIAM Review*, 11(2), 1969.

[72] D. A. Garanin and H. Kachkachi. Surface Contribution to the Anisotropy of Magnetic Nanoparticles. *Physical Review Letters*, 90(6):4, 2 2003.

[73] E. Paz, F. Garcia-Sanchez, and O. Chubykalo-Fesenko. Numerical evaluation of energy barriers in nano-sized magnetic elements with Lagrange multiplier technique. *Physica B: Condensed Matter*, 403(2-3):330–333, 2 2008.

[74] L Landau and E Lifshits. On the theory of the dispersion of magnetic permeability in ferromagnetic bodies. *Phys. Zeitsch. der Sow*, 8:153–169, 1935.

[75] T. L. Gilbert. A phenomenological theory of damping in ferromagnetic materials. *IEEE Transactions on Magnetics*, 40(6):3443–3449, 11 2004.

[76] J. C. Mallinson. On Damped Gyromagnetic Precession. *IEEE Transactions on Magnetics*, 23(4):2003–2004, 1987.

[77] D. Weller and A. Moser. Thermal effect limits in ultrahigh-density magnetic recording. *IEEE Transactions on Magnetics*, 35(6):4423–4439, 1999.

[78] B. S.D.Ch S. Varaprasad, Y. K. Takahashi, and K. Hono. Microstructure control of L10-ordered FePt granular film for heat-assisted magnetic recording (HAMR) media. *JOM*, 65(7):853–861, 7 2013.

[79] S. N. Piramanayagam. Perpendicular recording media for hard disk drives. *Journal of Applied Physics*, 102(1):011301, 7 2007.

[80] R. F.L. Evans, R. W. Chantrell, U. Nowak, A. Lyberatos, and H. J. Richter. Thermally induced error: Density limit for magnetic data storage. *Applied Physics Letters*, 100(10):102402, 3 2012.

[81] N. J. Gokemeijer, W. A. Challener, E. Gage, Y. T. Hsia, G. Ju, D. Karns, L. Li, B. Lu, K. Pelhos, C. Peng, T. Rausch, R. E. Rottmayer, M. A. Seigler, X. Yang, and H. Zhou. Challenges in Heat Assisted Magnetic Recording. Technical report, 2008.

[82] L. Guan and J-G Zhu. Recording, noise, and medium microstructure in perpendicular recording with a soft magnetic underlayer. *Journal of Applied Physics*, 91(10 I):8363–8365, 5 2002.

[83] D. Weller, G. Parker, O. Mosendz, E. Champion, B. Stipe, X. Wang, T. Klemmer, G. Ju, and A. Ajan. A HAMR media technology roadmap to an areal density of 4 Tb/in2. *IEEE Transactions on Magnetics*, 50(1), 1 2014.

[84] R. Wood. The feasibility of magnetic recording at 1 terabit per square inch. *IEEE Transactions on Magnetics*, 36(1 PART 1):36–42, 2000.

[85] J. Chureemart. *Orientation and Thermal Stability of Advanced Recording Media*. PhD thesis, University of York, 2013.

[86] F. Garcia-Sanchez. *Modeling of field and thermal magnetization reversal in nanostructured magnetic materials*. PhD thesis, Universidad Autonoma de Madrid, 2007.

[87] H. H. Guo, H. G. Chu, J. L. Liao, B. Ma, Z. Z. Zhang, and Q. Y. Jin. Thermal stability of fept-based exchange coupled composite films. *IEEE Transactions on Magnetics*, 49(7):3683–3686, 8 2013.

[88] Z. S. Shan, J. P. Liu, Vamsi M. Chakka, Hao Zeng, and J. S. Jiang. Energy barrier and magnetic properties of exchange-coupled hard-soft bilayer. In *IEEE Transactions on Magnetics*, volume 38, pages 2907–2909, 9 2002.

[89] P. N. Loxley and R. L. Stamps. Theory of domain wall nucleation in a two section magnetic wire. In *IEEE Transactions on Magnetics*, volume 37, pages 2098–2100, 7 2001.

[90] H. Kronmüller and D. Goll. Micromagnetic theory of the pinning of domain walls at phase boundaries. *Physica B: Condensed Matter*, 319(1-4):122–126, 7 2002.

[91] H. B. Callen and E. Callen. The present status of the temperature dependence of magnetocrystalline anisotropy, and the l(l+1) 2 power law. *Journal of Physics and Chemistry of Solids*, 27(8):1271–1285, 8 1966.

[92] R. W. Chantrell, N. Walmsley, J. Gore, and M. Maylin. Calculations of the susceptibility of interacting superparamagnetic particles. *Physical Review B - Condensed Matter and Materials Physics*, 63(2):024410, 12 2000.

[93] M. L. Plumer, T. J. Fal, J. I. Mercer, J. P. Whitehead, J. Van Ek, and A. Ajan. Kinetic Monte Carlo simulations of M-H Loops for HAMR recording media: Comparison with MOKE data. *IEEE Transactions on Magnetics*, 50(3):22–26, 2014.

[94] T. J. Fal, J. I. Mercer, M. D. Leblanc, J. P. Whitehead, M. L. Plumer, and J. Van Ek. Kinetic Monte Carlo approach to modeling thermal decay in perpendicular recording media. *Physical Review B - Condensed Matter and Materials Physics*, 87(6):064405, 2 2013.